Nanostructured Redox-Active Mesoporous Silica Films Based on An Electron-Hopping Mechanism : Charge Transfer Behaviors And Energy Storage Potentials

Jianren Wang

A thesis**:**

Nanostructured Redox-Active Mesoporous Silica Films Based on An Electron-Hopping Mechanism: Charge Transfer Behaviors And Energy Storage Potentials

by

Jianren Wang

For obtaining a **Doctoral** title

Major: Chemistry (Doctoral school C2MP)

Public defense scheduled **on 2 December 2020** in front of the jury**:**

Supervisor:
Dr. Neus Vilà — Lecturer (LCPME, Université de Lorraine)

Co-supervisor:
Dr. Alain Walcarius — Research Director (LCPME, Université de Lorraine)

Reviewers:
Pr. Patrice Simon — Professor (CIRIMAT, Université Toulouse III)
Pr. Christel Laberty-Robert — Professor (LCMCP, Sorbonne Université)

Examiners:
Pr. Laurent Ruhlmann — Professor (ICS, Université de Strasbourg)
Dr. Vanessa Fierro — Research Director (IJL, Université de Lorraine)

Films de silice mésoporeux nanostructurés redox actifs basés sur un mécanisme de saut d'électrons: comportements de transfert de charge et perspectives de stockage d'énergie

Sujet de thèse **:**

Présenté par

Jianren Wang

Pour l'obtention de titre de Docteur

Spécialité: Chimie (Ecole doctorale C2MP)

Soutenance publique prévue le **2 Décembre 2020** devant le jury:

Directrice:
Dr. Neus Vilà — Maître de Conférences (LCPME, Université de Lorraine)

Co-directeur:
Dr. Alain Walcarius — Directeur de Recherche (LCPME, Université de Lorraine)

Rapporteurs:
Pr. Patrice Simon — Professeur (CIRIMAT, Université Toulouse III)
Pr. Christel Laberty-Robert — Professeur (LCMCP, Sorbonne Université)

Examinateurs:
Pr. Laurent Ruhlmann — Professeur (ICS, Université de Strasbourg)
Dr. Vanessa Fierro — Directeur de Recherche (IJL, Université de Lorraine)

Acknowledgements

First and foremost, I hereby extend my thanks to my supervisors. **Neus Vilà**, thank you for the countless hands-on experimental guidance, numerous efforts for the materials characterizations, as well as endless tolerance for the mistakes I made. **Alain Walcarius**, your profound knowledge and rigorous scholarship have a deep influence on me, and I have also learned a lot of writing skills from the corrections you made for my drafts. Just as a famous saying, the mind is not a vessel to be filled but a fire to be kindled. The last three years working with you cultivate my interest of science, improve my ability to solve problems, and broaden my horizons, with which I believe I can go farther in my future life.

I would like to express a special gratitude to **Liang Liu**, whose lofty academic attitude and solid theoretical foundation always inspire me to strive for excellence. Your heart-to-heart talks and guidance always sustain me especially when I was not confident in moments of difficulties. Moreover, I would like to thank to the people who support my experiments: **Mathieu Etienne** for the SEM measurements; **Claire Genois** for the compound supply; **Gérard Paquot** and **Jean-Paul Moulin** for the Machining assistance; **Jérôme Grausem** for the FTIR set-up; **Grégory Francius** for AFM images; **Manuel DOSSOT** for the Raman spectra; and **Aurélien RENARD** for the XPS and Nitrogen Adsorption-desorption testes. I also feel grateful to **Grégoire Herzog**, **Christelle Despas**, **Marc Hebrant**, and **Michel Perdicaki** for the stimulating discussions during regular group meetings. Without your support and encouragement, I would not have been able to complete this thesis in time.

Then my thanks comes to my lab-mates from all over the world: **Samuel**, **Himanshu**, **Ning**, **Taisiia**, **Mengjie**, **Guofeng**, **Deomila**, **Joanna**, **Mariela**, **Wahid**, **Magdalena**, **Huong, Martha**, **Christelle**, and **José**. I cannot forget the parties we ever hold and the drinking time in bars, with endless topics from the culture difference to the international situation, from the experimental plan to the trip experience. I realized how privileged I am to get the chance to work with you. The joyful days and cheerful moments we spent together will always be treasured in my memory. With your company, I never felt lonely in the days aboard and I greatly enjoyed the time with you guys!

Likewise, I would like to express my sincere thanks for my friends in Nancy. Just to name a few of them (please forgive me for not being able to list all of them): **Shengzhao Pang**, **Ruotao Yang**, **Zhang Zhao**, **Yajun You**, **Kou Du**, **Hang Wan**, **Anji Ma**, **Yuan Chu**, **Tao Wang**, and many others. Your company brought a lot of joy to my life in the past three years. I also would like to say thanks to my landlady **Collet Dubas** who always invited me to her family meal and took care of me these years, which really let me feel at home.

I would like to give my sincere thanks to my parents: **Yingmao Wang** and **Yufeng Wang**. Like many Chinese students of my generation, I am the only child of my family. My parents have dedicated their entire lifetime to nurture and educate me, without asking for anything in return. I hope that I have not let my parents down so far and that they would be able to talk about me with pride. I also want to thanks to my girlfriend **Tian Li**, who encouraged me to go aboard to experience a different life and patiently comfort me when I was down.

To my parents and friends, for their unconditional love and support

Table of Content

Abstract

Electrical conductivity has always been a most fundamental element for energy storage electrodes. Because of this, there were only few attempts to use the insulating materials (i.e., silica, and anodized aluminium etc.) in the energy storage field despite their advantages including controllable and well-organized nanostructures, environmental benign properties, facile methods of synthesis, large surface area, as well as low cost. Electron-hopping, a special electron conduction mechanism, allows electrons to transfer among adjacent and close enough redox molecules directly without requiring the conductivity of supporting materials. This unique charge transfer feature makes possible the use of insulating materials for energy storage after functionalizing their surface with redox-active molecules. This thesis is focused on the: 1) demonstration of the feasibility of a novel idea to construct energy storage materials with a demo of redox-molecules functionalized silica film deposited on ITO electrode; 2) achievement of a large-scale assembly of such silica film on graphene substrate which possesses a high surface area; 3) development of the prototype of flexible planar devices.

First, the redox-active and vertically-aligned mesoporous silica thin films were prepared on indium-tin oxide electrode from the combination of an electrochemically-induced self-assembly method (to generate azide functionalized silica) and a copper-catalyzed azide-alkyne click reaction (to derivatize the material with electroactive groups). Such insulating silica films composed of uniformly distributed vertical mesochannels (pore diameter: 2 nm) provide a large surface area to accommodate the redox active species, such as ferrocene, on the surface of silica walls. Besides, the density of the redox molecules can be easily varied by tuning the composition of silane precursors (3-azidopropyl triethoxysilane, and tetraethoxysilane) in the starting solution. These features make such organic-inorganic films an ideal platform to evaluate the energy storage potential, and the factors influencing the electron-hopping

process. The most effective system is the ferrocene-functionalized silica film prepared from 40% organosilane, which is able to deliver a capacity of 105 C cm^{-3} (1.10 mC cm^{-2}) at a current density of 0.4 A cm^{-3}. (with up to 48% capacity retention achieved at a short charging time of 2.8 s).

The ITO substrate can only provide limited area for the growth of the mesoporous silica film, restricting energy and power density of the final electrode. Therefore, the extensive assembly of such redox-active silica film has been further done by using a large surface area electro-exfoliated graphene as the current collector to study its interest in delivering fast redox reactions over a large-scale (contrary to monolayer-based electroactive system generated on the ITO electrode). Multiple characterization techniques have been used to analyze the obtained electrode (labelled as Fc-MS@EG). It proves a uniform deposition of the ferrocene functionalized mesoporous silica thin film on the few-layers graphene. As a result, a sandwich structure with a thickness ~70 nm was formed. Compared with the ITO counterpart, the Fc-MS@EG can deliver ~200 times higher specific capacity of 196 mC cm^{-2} (326 mF cm^{-2}) at a current density of 2 mA cm^{-2}, and 69% capacity retention even at 3800 C, which is much better than the traditional faradic materials.

An attempt to fabricate a flexible planar micro-device operating with the electron-hopping mechanism has been done through generating the ferrocene functionalized silica film on the flexible graphene electrode. With this aim, a systematic preparation protocol is proposed including transfer of a thin layer of graphite on scotch tape, 3D printing assisted patterning, electro-exfoliation of graphite, and following deposition of the silica layer, and click chemistry. The preliminary results prove the feasibility of this protocol, and the obtained planar electrode shows a high flexibility thanks to the scotch tape substrate. It also delivers a high capacity of 24.5 mC cm^{-2} at a current density of 0.5 mA cm^{-2}, and good rate performance of 81% capacity retention at a current density of 8 mA cm^{-2}.

Résumé

Les progrès rapides de la société et l'augmentation constante des besoins matériels entraînent une consommation explosive de sources d'énergie non renouvelables, telles que le pétrole et le charbon, qui peuvent difficilement répondre à la demande dans un avenir proche. En outre, le processus d'extraction et la consommation de ressources énergétiques fossiles ont également entraîné de graves problèmes environnementaux et climatiques en raison des émissions de carbone et des rejets de dioxyde d'azote et de dioxyde de soufre, etc. Par conséquent, le développement et l'utilisation des sources d'énergie renouvelables est une voie inévitable pour le développement durable de la société au 21e siècle. De nouvelles sources d'énergie, notamment l'énergie éolienne, l'énergie solaire et l'hydroélectricité, ont été exploitées ces dernières années. Cependant, le caractère intermittent et la répartition géographique inégale de ces nouvelles sources d'énergie posent des difficultés pour leur utilisation pratique directe, et il faut donc des dispositifs de stockage de l'énergie pour une utilisation efficace, sûre et fiable de ces sources. Les batteries secondaires au lithium-ion à haute densité énergétique (près de 180 Wh/kg) sont actuellement les dispositifs de stockage d'énergie électronique les plus utilisés, mais le processus relativement lent d'intercalation des ions lithium en phase solide limite leur densité de puissance. En revanche, les supercondensateurs peuvent fournir une densité de puissance beaucoup plus élevée (10 kW/kg), d'excellentes performances de débit, une longue durée de vie et une large plage de températures d'utilisation. Par conséquent, l'amélioration de la densité énergétique des supercondensateurs et la réalisation de caractéristiques supplémentaires (par exemple, la transparence, la flexibilité et la microminiaturisation) pour répondre aux demandes de stockage d'énergie de plus en plus massives et variées sont les tendances de développement croissantes.

La conductivité électrique a toujours été un élément fondamental pour les électrodes de stockage d'énergie. C'est pourquoi il n'y a eu que peu de tentatives d'utilisation des matériaux isolants (silice, aluminium anodisé, etc.) dans le domaine du stockage de

l'énergie, malgré leurs avantages, notamment des nanostructures contrôlables et bien organisées, des propriétés respectueuses de l'environnement, des méthodes de synthèse faciles, une grande surface et un faible coût. Le saut d'électrons, un mécanisme spécial de conduction des électrons, permet aux électrons de se transférer directement entre les molécules redox adjacentes sans avoir besoin de la conductivité des matériaux de support. Cette caractéristique unique de transfert de charge permet d'utiliser des matériaux isolants pour le stockage de l'énergie après avoir fonctionnalisé leur surface avec des molécules redox actives. Cette thèse porte sur le : 1) la démonstration de la faisabilité d'une nouvelle idée pour construire des matériaux de stockage d'énergie avec une démonstration de molécules redox fonctionnalisées sur un film de silice déposé sur une électrode ITO ; 2) la réalisation d'un assemblage à grande échelle sur un substrat de graphène qui possède une surface élevée ; 3) le développement du prototype de dispositifs planaires flexibles.

Tout d'abord, les couches minces de silice mésoporeuse fonctionnalisée de molécules redox ont été préparées sur une électrode d'oxyde d'indium-étain à partir de la combinaison d'une méthode d'auto-assemblage induite électrochimiquement (pour générer de la silice fonctionnalisée par un azide) et d'une réaction de clic azide-alcyne catalysée par le cuivre (pour dériver le matériau avec des groupes électroactifs), comme l'illustre la **Figure 1**. Ces films de silice isolants composés de mésocanaux verticaux uniformément répartis (diamètre des pores: 2 nm) offrent une grande surface pour accueillir les espèces redox actives, telles que le ferrocène, à la surface des parois de silice. En outre, la densité des molécules d'oxydoréduction peut être facilement modifiée en ajustant la proportion d'azide-silane dans la solution de précurseur. Ces caractéristiques font de ces films organique-inorganique une plateforme idéale pour évaluer le potentiel de stockage de l'énergie et les facteurs influençant le processus de saut d'électrons. Le système le plus efficace est le film de silice fonctionnalisé au ferrocène, préparé à partir d'organosilane à 40%, qui est capable de fournir une capacité de 105 C cm^{-3} (1,10 mC cm^{-2}) à la densité de courant de 0,4 A cm^{-3}. (avec une rétention de capacité allant jusqu'à 48 % obtenue avec un temps de charge aussi court que 2,8 s).

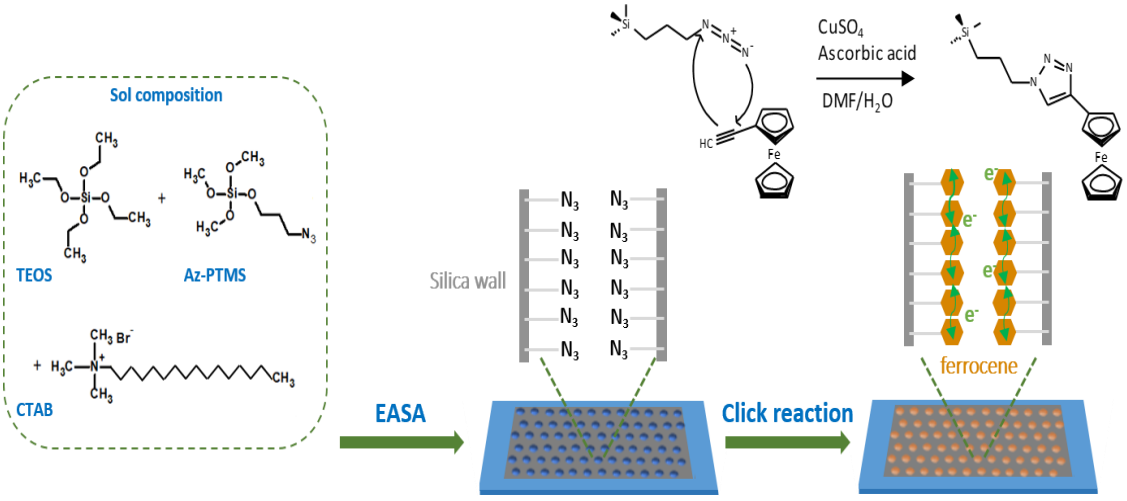

Figure 1. Illustration schématique du processus de préparation des couches minces de silice mésoporeuse à fonctionnalisation ferrocène, alignées verticalement, sur un morceau d'électrode ITO plate.

Le substrat ITO ne peut fournir qu'une surface limitée pour la croissance du film de silice mésoporeux, ce qui limite son énergie finale et sa densité de puissance. Par conséquent, l'assemblage étendu du système de dopage électronique à base de silice est ensuite généré sur un collecteur de courant en graphène électro-exfolié de grande surface afin d'étudier son intérêt pour la réalisation de réactions d'oxydoréduction rapides à grande échelle (contrairement au système électroactif à base de monocouche généré sur l'électrode ITO), comme l'illustre la **Figure 2**. Des caractérisations multiples ont été utilisées pour analyser l'électrode obtenue (appelée Fc-MS@EG). Elle prouve un dépôt uniforme de la fine couche de silice mésoporeuse fonctionnalisée au ferrocène sur les quelques couches de graphène. Il en résulte une structure en sandwich d'une épaisseur de ~70 nm. Comparé à son homologue de l'ITO, le Fc-MS@EG peut fournir une capacité spécifique environ 200 fois plus élevée de 196 mC cm^{-2} (326 mF cm^{-2}) à une densité de courant de 2 mA cm^{-2} et une rétention de capacité de 69% même à 3800 C, ce qui est bien mieux que les matériaux faradiques traditionnels.

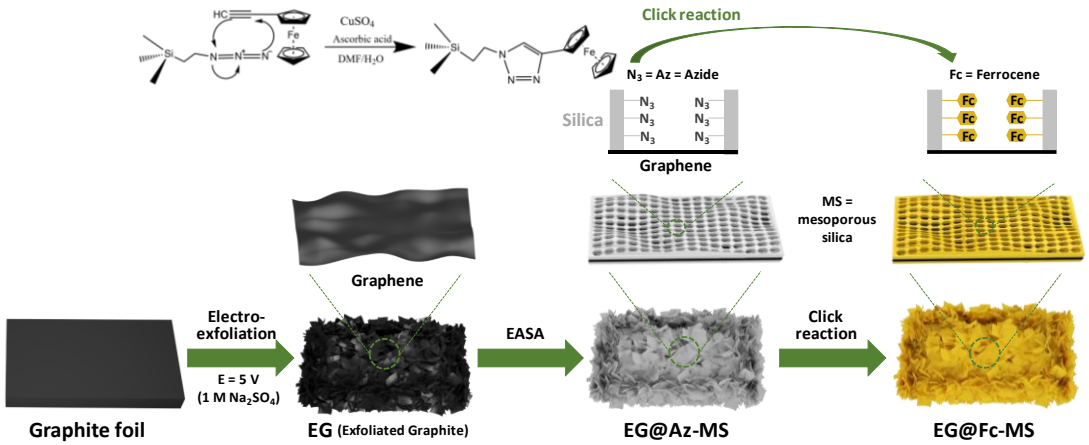

Figure 2. Illustration schématique de la formation de EG@Fc-MS. Elle implique la formation de graphite exfolié (EG), sa modification avec une silice mésoporeuse fonctionnalisée par un azide (Az-MS) et une dérivatisation finale par chimie de clic pour former la silice mésoporeuse greffée par un ferrocène (Fc-MS).

Une tentative de fabrication d'un micro-dispositif planaire flexible fonctionnant avec le mécanisme de saut d'électrons a été réalisée en générant le film de silice fonctionnalisé au ferrocène sur l'électrode flexible en graphène. Dans ce but, un protocole de préparation systématique est proposé, comprenant le transfert d'une fine couche de graphite sur du scotch, l'impression 3D assistée de motifs, l'électro-exfoliation du graphite et, après le dépôt de la couche de silice, la chimie du clic, comme l'illustre la **Figure 3**. Les résultats préliminaires prouvent la faisabilité de ce protocole, et l'électrode plane obtenue montre une grande flexibilité grâce au substrat de scotch tape. Elle offre également une capacité élevée de 24,5 mC cm^{-2} à la densité de courant de 0,5 mA cm^{-2}, et une bonne performance de taux de rétention de capacité de 81% à la densité de courant de 8 mA cm^{-2}.

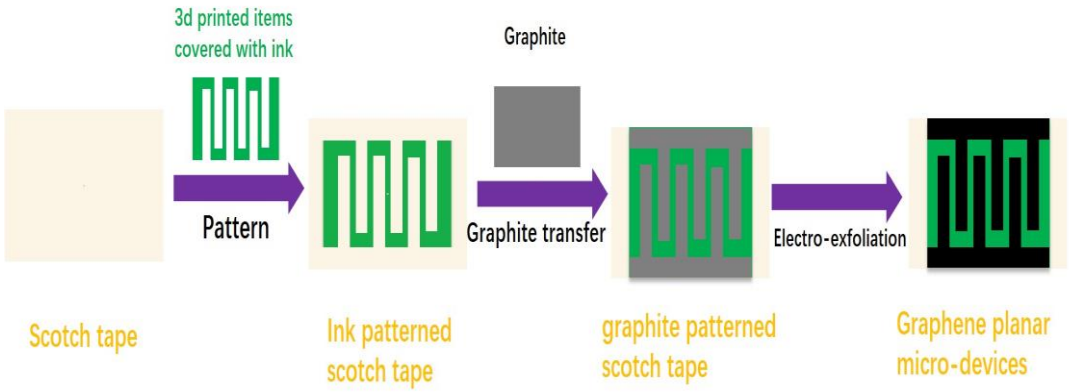

Figure 3. Le processus prévu pour la fabrication de microdispositifs planaires en graphène.

Dans l'ensemble, un nouveau type de matériaux de stockage d'énergie à base de silice fonctionnant avec un mécanisme de saut d'électrons a été préparé en combinant une méthode d'auto-assemblage induite électrochimiquement (EASA) et une réaction azide-alcyne catalysée par le cuivre (CuAAC). Les centres actifs redox (molécules de ferrocène ou de cobaltocénium) répartis à la surface du film de silice peuvent directement commuter les électrons par le biais du processus de saut d'électrons. Les résultats démontrent que ce mécanisme de transfert de charge est capable de fournir un taux de transfert d'électrons rapide même sur le substrat de silice isolant, ce qui se traduit par une performance de taux supérieure par rapport aux matériaux faradiques traditionnels. La haute densité des molécules redox et la voie de diffusion des contre-ions lisses ont été identifiées comme jouant un rôle essentiel pour assurer le processus de saut d'électrons rapide. En outre, l'assemblage à grande échelle du système de saut d'électrons a été réalisé en générant le film de silice fonctionnalisé au ferrocène sur une électrode autoportante en mousse de graphène, présentant une densité de capacité 100 fois plus élevée que celle générée sur une électrode ITO, tout en maintenant la performance de taux élevé. Enfin, une tentative a été faite pour assembler la silice fonctionnalisée au ferrocène sur un dispositif planaire flexible, et les résultats préliminaires ont prouvé la faisabilité de l'idée que nous proposons. Globalement, dans cette thèse, l'étude systématique du potentiel du processus de saut d'électrons dans le

domaine du stockage de l'énergie, qui pourrait ouvrir une nouvelle voie pour la construction de matériaux de stockage de l'énergie.

- Ces travaux évaluent tout d'abord le potentiel du saut d'électrons en tant que mécanisme de transfert de charge prometteur pour les matériaux de stockage de l'énergie. Les matériaux préparés à base de silice fonctionnant avec ce mécanisme présentent des performances de stockage d'énergie compétitives.

- Ce travail prouve que les matériaux isolants nanostructurés peuvent également être utilisés pour les applications de stockage d'énergie, ce qui brise le stéréotype et élargit largement le choix des matériaux d'électrode.

- Ces travaux évaluent en particulier la valeur de stockage de l'énergie des couches minces de silice fonctionnalisées par les molécules d'oxydoréduction préparées avec la méthode de l'AESA, en réalisant leur démonstration de faisabilité, l'assemblage à grande échelle et la tentative de construction de dispositifs planaires flexibles, ce qui favorise solidement le développement de ces couches minces.

Objectives of This Thesis

The electron-hopping redox mechanism shows great advantages in terms of both fast redox kinetics and solid-phase free counterions diffusion processes. However, the potential of the electron-hopping process has been long-time overlooked in the energy storage field, and few efforts trying to construct the energy storage devices on the basis of this mechanism. Therefore, the general idea for my thesis is to fabricate a novel kind of energy storage devices/pseudocapacitors operating with the electron hopping mechanism, to analyze possible parameters affecting energy storage behaviors, and to evaluate their practical values. To achieve this goal, the redox-active vertically aligned silica thin film has been prepared with the combination of EASA (electro-assisted self-assembly) method and click chemistry, which is chosen as the platform to evaluate the electron-hopping process. The insulating nature of silica wall would exclude any possibilities to conduct electrons, and therefore the electron-hopping process among the redox species on the surface of silica becomes the only way to achieve the faradic reaction.[1,2] Large surface area and vertically aligned mesochannels of such silica film would also accommodate high density of active species, and facilitate the mass transport during the redox reaction. Overall, in this work, the construction of energy storage devices operating with electron-hopping has been achieved, and the possible factors that may affect the energy storage behaviors have also been analyzed in detail.

Chapter I

Introduction

The rapid progress of society and keep surging material needs result in an explosive consumption of non-renewable energy sources, such as oil and coal, which can hardly meet the demand in the near future.[3,4] Besides, the mining process and the consumption of fossil energy resources have also brought seriously environmental and climate problems due to the carbon emissions and the discharges of nitrogen dioxide and sulfur dioxide, etc. Therefore, developing and utilizing renewable energy sources is an inevitable way for the sustainable development of society in the 21st century.[5] New energy sources, including wind energy, solar energy, and hydropower, have been exploited in recent years. However, the intermittent feature and uneven geographical distribution of these new energy sources pose difficulties for the direct practical use, and therefore energy storage devices are required for efficient, safe and reliable utilization of these sources.[6] Lithium-ion secondary batteries featured with high energy density (close to 180 Wh/kg) are currently most widely used electronic energy storage devices, [7] but the relative slow lithium ions intercalation process in solid phase restricts their power densities. In contrast, supercapacitors can deliver much higher power density (10 kW/kg), excellent rate performance, long cycle life, and the wide temperature range of use.[8] Therefore, improving the energy density of supercapacitors and achieving additional features (e.g., transparency, flexibility and microminiaturization) to meet the more and more massive and various energy storage demands are the growing development trends.[9] In the following chapters, the origin of supercapacitors, evaluation indicators, energy storage mechanisms, types and electrochemical characteristics of supercapacitors will be introduced and then puts forward our research ideas in conjunction with the bottleneck problems of supercapacitors.

1.1 Development history of supercapacitors

As early as 18th century, people started to learn about electrical phenomena with the rise of electrostatic physics research, such as the invention of "electrical devices" (e.g., Electrophorus and Van de Graaff generator). After 140 years, the understanding of electrical phenomena in the depth of the molecular and electronic levels began, due to the pioneering work of Faraday, Tomson, and Milikan.[10] As shown in **Figure 1**, the invention of the Leyden Jar is an important historical event for the study of electrical energy storage. Leyden Jar is a prototype of the supercapacitor, consisting of a glass jar with metal foil cemented to the inside and the outside surfaces, and a metal terminal projecting vertically through the jar lid to make contact with the inner foil. It can store electric charges (from an external source) between metal foil on the inside and outside of the jar. Because of the Leyden Jar, people established the concept that “static electricity” can be stored at the interface between the solid electrode and the electrolyte. But the nature behind the charges storage phenomenon is not clear until the 19th century. In 1853, VonHelmholz proposed a mechanism of the interfacial charges storage by studying ions behavior in colloidal suspensions, and established the first electrical double layer model, namely Helmholtz model.[11] Supercapacitor researches flourished in the 20th century, the modern electrical double layer capacitor theories were developed by Gouy,[12] Chapman,[13] Stern[14] and Grahame.[15] Soon afterwards, H.I. Becker et al. first put electrical double layer capacitor into practice, they used porous carbon as the electrode in aqueous electrolyte for charges storage, and applied a patent for it.[16] But, unfortunately, this patent was not commercialized finally. The first non-aqueous electrochemical capacitor was invented by Robert Rightmire of SOHIO Company.[17] Compared with aqueous capacitors, the working voltage of non-aqueous capacitors is higher, which means it can store more charges. In 1978, NEC corporation used SOHIO's technology to prepare the first commercially electrical double layer capacitor, named "supercapacitor", which successfully opened the door to commercial market, and was widely used in backup power supplies, clock

chips and other electronic devices.[18]

In 1971, it was discovered that, compared to electrical double layer capacitor, RuO_2 could store more charges through the Faraday reaction, and therefore, a new type of electrochemical capacitor was proposed.[19,20] In the 1980s, PRI company used RuO_2 and Ta_2O_5 as the electrode to prepare a high-performance capacitor, but it was not widely used due to its high price.[21] Subsequently, the U.S. Department of Energy and the current world supercapacitor giant Maxwell Technology began intensive research on improving the performance of supercapacitors. Since then, various new-type supercapacitors sprang up, and played important roles in back-up power systems, continuous power supply systems, and heavy-duty crane start systems.[22] More and more related studies have been done in recent years for developing advanced "supercapacitors" and deeply understanding their energy storage mechanisms to long-time, high-safety, and stably support the operation of the electronic devices.

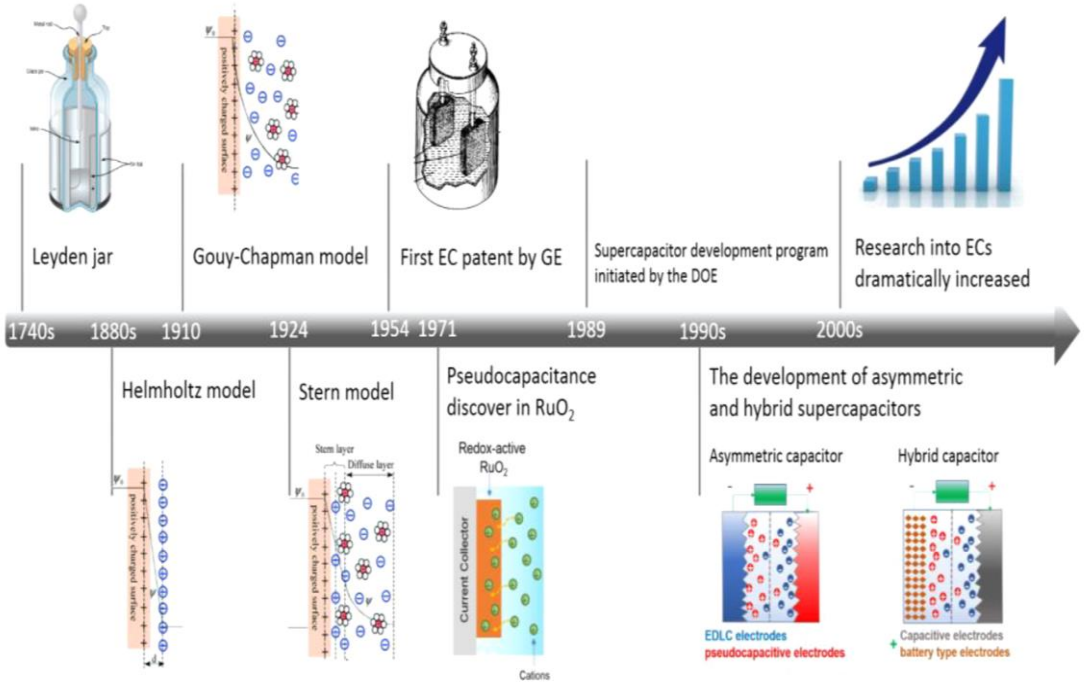

Figure 1. Historic timeline for the development of supercapacitors.[18]

1.2 The main evaluation indicators for capacitors

Capacitor is a passive electronic component that can store electrical energy in an electric field. It consists of two conductive terminals and a dielectric between them. By applying an external voltage, the electrons migrate between the two terminals to balance the potential difference and to store energy. The capacitance C of the capacitor is the ratio between the stored charges (Q) and the applied voltage (V), as expressed in equation 1:

$$\mathrm{C} = \frac{Q}{V} \qquad \text{Equation 1}$$

or the classical parallel-plate capacitor, C can also be expressed as:

$$\mathrm{C} = \frac{\varepsilon_0 \times \varepsilon_r \times A}{D} \qquad \text{Equation 2}$$

Where A is the area of parallel-plates (m^2), D is the separated gap thickness between the parallel-plate (m), and ε_0, ε_r are the permittivity for the vacuum and the dielectric ($F\ m^{-1}$), respectively.

The energy density (E) and power density (P) are the two important indicators of capacitor performance. The energy density is the energy that can be stored in the capacitor per unit, which can be calculated by the following formula:

$$\mathrm{E} = 0.5 \times \mathrm{C} \times V^2 \qquad \text{Equation 3}$$

Where E is the energy density ($Wh\ kg^{-1}$ or $Wh\ cm^{-3}$), C is the capacitance of the capacitor ($F\ kg^{-}1$ or $F\ cm^{-3}$), and V is the external applied voltage (V).

The power density is the rate of energy transmission per unit time. The power density of a capacitor is usually related to the equivalent resistance of the capacitor (ESR), which produces a voltage drop that limits the maximum energy and power of the capacitor. The power density of the capacitor can be calculated by the following equation:

$$P_{max} = \frac{V^2}{4 \times ESR}$$ Equation 4

Where P is the energy density (W kg^{-1} or W cm^{-3}), V is the external applied voltage (V) and ESR is the equivalent resistance of the capacitor (ESR).

1.3 The energy storage mechanisms of supercapacitors

Electrochemical double layer capacitors (EDLCs) are a special and important type of capacitors. Unlike physical capacitors, the electrodes of EDLCs are exposed into electrolyte and charges can be stored at the electrode/electrolyte interface.[23] EDLCs also follows the basic principles of capacitors, but their capacitance is more than 1,000 times higher than traditional capacitors because of the large specific surface area of electrodes and tightly adsorbed ions on their surface in the nano-scale dielectric distance.[24–26] Besides, supercapacitors can also deliver high power densities because of the fast rate of storing and releasing ions during the energy storage process. However, compared with rechargeable batteries, despite much higher performance than conventional capacitors, supercapacitors show limited capacity due to their different charge storage mechanisms. Batteries can store the ions/charges in the bulk phase of the electrodes, while the EDLCs can only store the ions/charges at the interface of the electrodes via a physical adsorption process. The ions intercalation process of batteries leads to high energy densities but relatively low power densities due to the slow ions diffusion in the solid phase. (~ 10^{-15}-10^{-16} m^2 s^{-1})[27] In contrast, the EDLCs can deliver much higher power densities due to the fast rate of physical surface adsorption of ions. For classical EDLCs electrodes, carbon-based materials including activated carbon,[28,29] carbon aerogel,[30] carbon nanotubes (CNTs),[31,32] and graphene[33,34] are widely used because of their large surface area, good electrical conductivity, and superior chemical stability.[35] However, pure physical ions adsorption mechanism of EDLCs also restrict their energy densities to some extent and corresponding surficial capacitance is from 10 μF cm^{-2} to 21 μF cm^{-2}.[36,37] The

specific surface area of carbon materials always range from 1000 m^2 g^{-1} to 3000 m^2 g^{-1} and therefore they can theoretically provide capacitance from 100 F g^{-1} to 600 F g^{-1}.[38] But, in practical tests, the capacitance of carbon-based materials can only achieve 100 F g^{-1} to 250 F g^{-1} because not all the surface area can be fully utilized during the energy storage processes.[39] As a result, shown in **Figure 2**, batteries and EDLCs are complementary but cannot completely replace each other.[40]

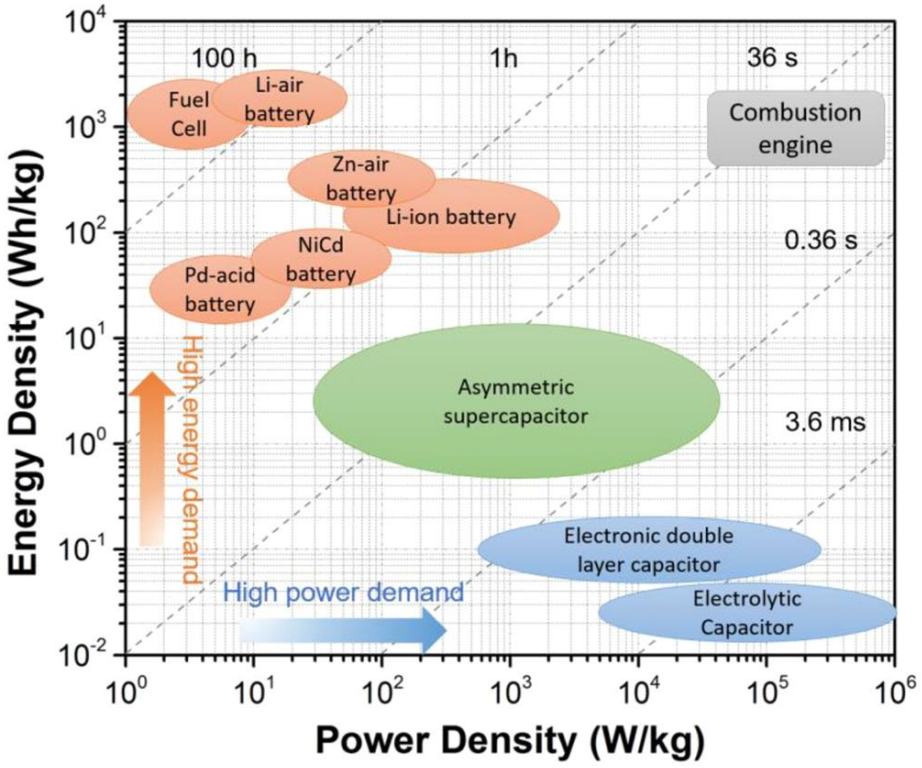

Figure 2. Ragone plot illustrating the performances of specific power vs. specific energy for different electrical energy-storage technologies. Times shown in the plot are the discharge time, obtained by dividing the energy density by the power density.[18]

Unlike EDLCs, pseudocapacitors is a different type of capacitors that can store charges/ions through fast, reversible redox reactions on the surface/near-surface region of faradic materials (**Figure 3).** The energy storage of pseudocapacitors does not originate from physical ions adsorption but from the valence changes of electrode materials. This property permits the pseudocapacitors (or asymmetric supercapacitors when the anode and cathode are different) a balanced behavior between EDLCs and

batteries,[18] shown in **Figure 2**. RuO_2 is the first reported pseudocapacitive material that can store energy via fast and reversible surface redox of ruthenium. Since then, especially in recent years, numerous pseudocapacitive materials have been reported. Generally speaking, the energy storage active sites of pseudocapacitive materials are located at the near-surface, which means the distance is $\ll (2Dt)^{0.5}$, where D is ions diffusion coefficient ($cm^2\ s^{-1}$) and t is diffusion time (s).[41] If based on the energy storage mechanisms, the pseudocapacitive materials can be divided into three types, namely underpotential deposition, redox mechanism, and intercalation mechanism.[42] 1) Underpotential deposition is that ions attached to the metal/electrolyte interface can be deposited onside under a biased potential to the reversible thermodynamic potential, such as the adsorption of H^+ on the surface of Pt or the deposition of Pd^{2+} on Au. (**Figure 3**b) 2) Redox pseudocapacitance is that fast and reversible redox reactions occur on the surface/near-surface of transition metal derivatives such as MnO_2, [43,44] RuO_2,[45] and conductive polymers.[46] 3) Intercalation capacitance is that ions enter the interlayer with redox active materials to react, but no phase change occurs, such as Nb_2O_5.[47,48] Although there are clear definitions for pseudocapacitance, the boundaries between batteries and pseudocapacitors are still blurred due to the similar mechanisms. (e.g., the redox reactions and intercalation processes are also the typical mechanisms for batteries) Therefore, the criteria need to be set to identify their energy storage characteristics, and to distinguish differences between them.

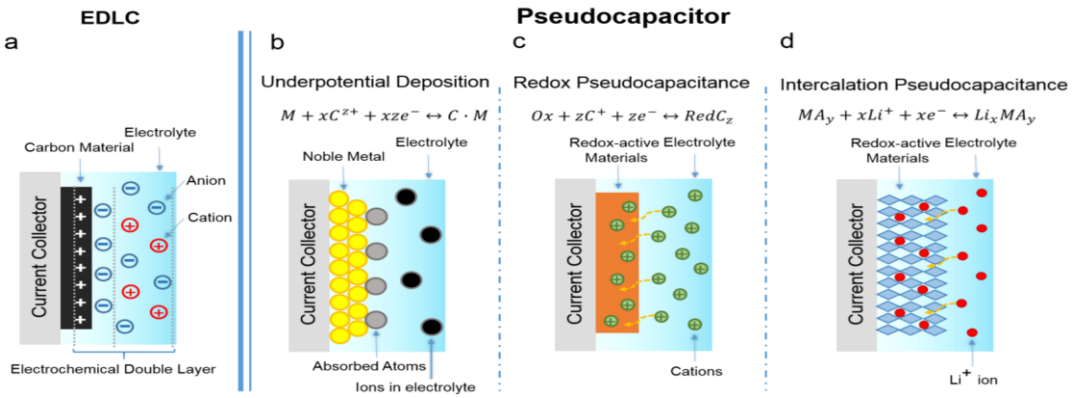

Figure 3. Schematics of charge-storage mechanisms for (a) EDLCs and (b-d) different types of pseudocapacitive electrodes: (b) underpotential deposition, (c) redox pseudocapacitor, and (d) ion intercalation pseudocapacitor.[42]

1.4 The features of batteries and supercapacitors

In the early stages, there is a sharp distinction between batteries and supercapacitors/pseudocapacitors. Only the materials that show rectangular cyclic voltammetry curves (**Figure 4**a&b) and a linear voltage response (a triangular-shaped curve) during constant current charge/discharge curves (**Figure 4**c) can be considered as capacitive materials. The current response of this kind of materials is directly proportional to the charge/discharge rate, i.e., $i = Cv$, where i is the current response, C is the capacitance and v is the scan rate during the CV test. In addition, the capacitance can be calculated with the equation of $C=Q/\Delta E$, where Q is the charges that are stored, ΔE is the width of the potential window, and C should be a constant (even for the pseudocapacitors like that in **Figure 4**b) independent to ΔE. Whereas, for batteries, prominent and widely separated peaks associated with the reduction and oxidation of transition metal centers can be observed during the cyclic voltammetry. (**Figure 4**g&h) Unlike that of capacitors, the potential response of a battery is profoundly nonlinear during the charge/discharge curves and obvious plateaus can be observed at the potentials of the faradaic reduction or oxidation of the active sites (**Figure 4**i). Therefore, it is easy to distinguish the traditional batteries and supercapacitors/pseudocapacitors. However, with the rapid development of "nano-technology", increasing numbers of new pseudocapacitive materials (e.g., transition-metal oxides, hydroxides, sulfides, carbides, nitrides, conducting polymers, etc.) display electrochemical characteristics that are neither purely capacitive nor purely battery-type. As a result, the boundaries between batteries and pseudocapacitors become more and more blurred. Similar to that of batteries, redox/intercalation peaks can be observed for the pseudocapacitive materials during the cyclic voltammetry (**Figure 4**d&e**).** But, it should also note that the peaks of pseudocapacitive materials are highly symmetrical without obvious peak-to-peak separation, because the size of these materials are reduced to the nanoscale, diffusion path lengths for ions are significantly reduced, and surface active sites available for non-insertion charge storage are

dramatically enhanced.[41] Also, the charge-discharge curves of pseudocapacitive materials are distorted (**Figure** 4f**)**, showing as an intermediate state between batteries and pseudocapacitors.

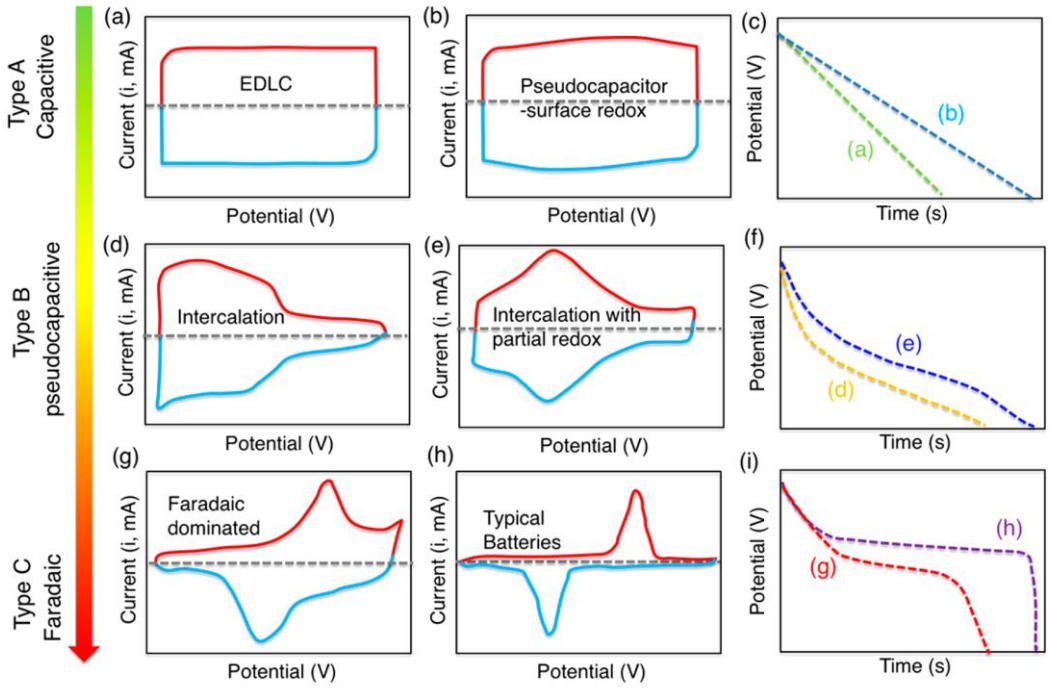

Figure 4. Schematic cyclic voltammetry (a, b, d, e, g, h) and corresponding galvanostatic discharge curves (c, f, i) for various kinds of energy-storage materials. A pseudocapacitive material will generally have the electrochemical characteristics of one, or a combination, of the following categories: (b) surface redox materials (e.g., MnO_2 in neutral, aqueous media), (d) intercalation-type materials (e.g., lithium insertion in Nb_2O_5 in organic electrolytes), or (e) intercalation-type materials showing broad but electrochemically reversible redox peaks (e.g., Ti_3C_2 in acidic, aqueous electrolytes). Electrochemical responses in (g-i) correspond to battery-like materials. [41]

How to define the in-between behaviors of these pseudocapacitive materials has arisen long dispute, especially in recent years. Jeffrey W. Long et al. propose this type of materials as battery-type materials, C/mAh is more suitable to be used as the unit rather than F, and only those show rectangular curves during the cyclic voltammetry can be considered as pseudocapacitive materials such as MnO_2 and RuO_2 etc.[49] This point of view received a large number of supporters, and the corresponding paper obtains

1,240 citations within 5 years.[49] The major argument to support this idea is that the relationship between capacity and the potential window is nonlinear. As shown in CV curves of Co_3O_4 thin film (**Figure 1.5**), the capacitance varies with the selected potential window, and therefore, defining it as the battery-type material is more suitable.

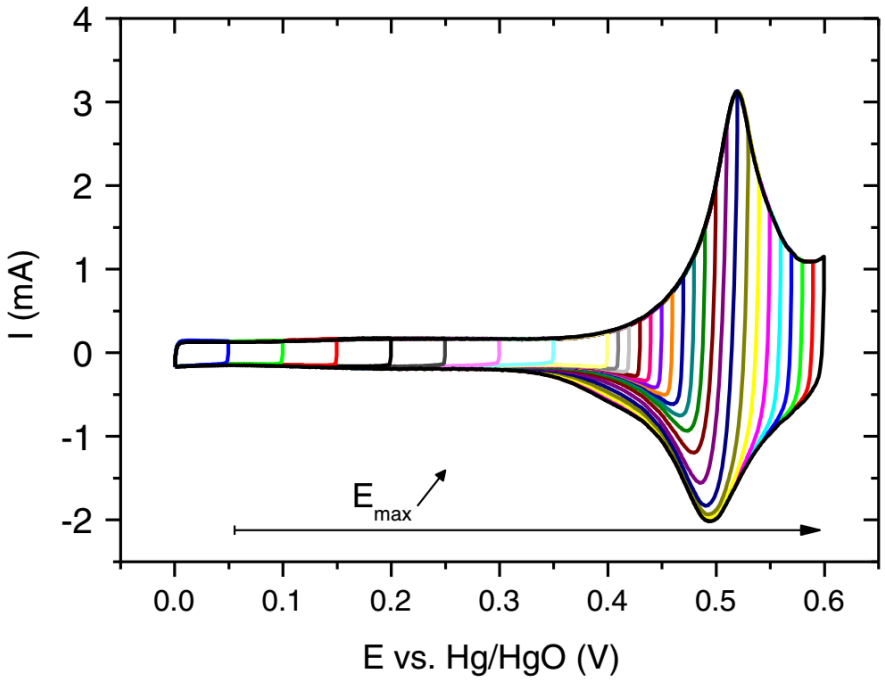

Figure 5. Cyclic voltammetry (10 mV s^{-1}) of an electroplated Co_3O_4 thin film annealed at 300 ºC, using different upper potential limits, in 1 M KOH electrolyte.

On the other hand, Patrice Simon et al. consider this type of materials as pseudocapacitive materials. This opinion also receives a lot of support and the citations of the corresponding paper reach 2,698 within 6 years.[3] The most important argument focuses on the potential response during charge-discharge processes rather than cyclic voltammetry. As shown in **Figure 6**, the $LiCoO_2$, a typical battery cathode material, delivers different potential-time profile because of the size effect. When the size of the $LiCoO_2$ reduces to nano-level (i.e., 6nm), the charge-discharge curve seems more like supercapacitors instead of batteries behavior that obtained from the bulk counterpart. They claim the nano-effect will introduce the “extrinsic” pseudocapacitance due to the accelerated surface/near-surface redox reactions and intercalation processes by significantly reducing the scale of active materials. In addition, the rate performance of

this kind of materials is much higher than traditional battery electrodes (e.g., fully recharged in 1 min, referred to as a rate of 60 C).

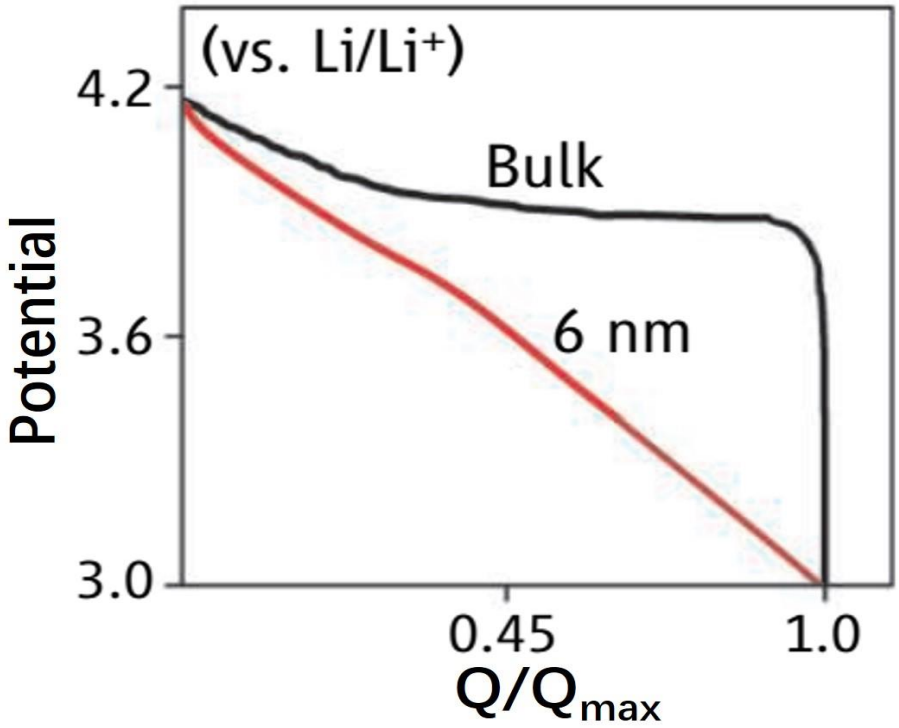

Figure 6. Difference of charge-discharge curves between bulk $LiCoO_2$ and nanosized (6 nm) $LiCoO_2$.

Both views are reasonable, and opposite conclusions are derived from the different focus of attention. Obviously, this new type of material is in the middle of traditional batteries and supercapacitors, possessing similar charge-discharge behaviors to EDLCs, but also showing distinct peaks during the cyclic voltammetry like that of batteries. In my opinion, we need to go back to the nature of energy storage devices before defining the new type of materials. The origin usage scenario for the energy storage devices is the current output/input, namely galvanostatic charge-discharge process, and the cyclic voltammetry just acts as analysis methods to understand the energy storage mechanisms. Therefore, either C or F can be used as the unit for this kind of material, at least within a certain potential window, to evaluate the energy storage capacity. In addition, some criteria have been established by previous works to distinguish this new type of materials from traditional battery materials.

1.5 The criteria to distinguish pseudocapacitive materials and battery-type materials

The rate-determining step during the energy storage process is one of the main criteria to judge what type of material it is. The diffusion-controlled (always the slow diffusion inside the solid phase of active materials) energy storage behavior is the sign for battery-type materials. Whereas capacitive materials will deliver a surface-controlled energy storage behavior due to the fast ions diffusion processes and the superior reaction kinetics. Therefore, a set of methods have been developed by previous studies to reveal the nature of the energy storage process.

As discussed above, one of the essential characteristics of pseudocapacitive materials is the linear or approximately linear relationship between stored charges and potential change during the charge/discharge test. Besides, although both types of materials show peaks during the cyclic voltammetry test, the current responses at various scan rates are different, which can also be used to distinguish pseudocapacitive materials. The relationship between currents and scan rates at a fixed potential can be described with the following equation [50]:

$$\mathrm{i} = \mathrm{a} \times v^{b}$$

Where i (A) is the current at a fixed potential, v (v/s) is the scan rate, and a, b are the parameters obtained by fitting the data.

The obtained b value is the indicator for the energy storage behavior. If the b value is close to 0.5, the energy storage process is diffusion-controlled, which means this is the battery-type electrode. Whereas, if the b value is close to 1, this means that the energy storage process is a surface-controlled behavior, indicative of the capacitive electrode. Therefore, the real rate-determine step at different potentials can be revealed by fitting the cyclic voltammetry data. For example [51], as shown in **Figure 7**a, a pair of redox

peaks can be observed for the nanosized TiO_2 during the cyclic voltammetry test, which comes from the insertion of the lithium ions into its lattice structure. The b values are also calculated from these curves at different potentials by taking the cathodic branches, and the results are given in **Figure 7**b. The b values are potential dependent. In non-faradic region, the b values are close to 1, which means this is a capacitive behavior. While, in the faradic region, the b values are close to 0.5, indicating the energy storage behavior is controlled by the lithium ions diffusion inside the TiO_2 solid phase.

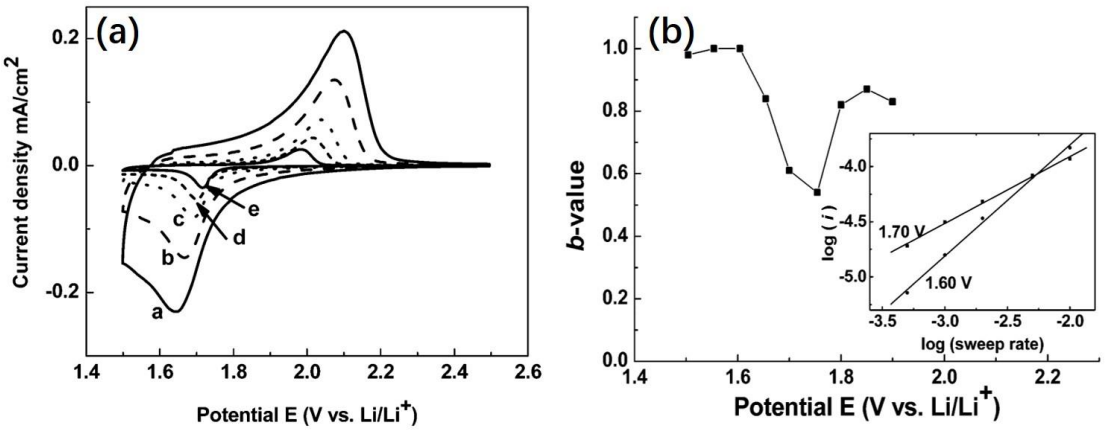

Figure 7. (a) Voltammetric responses for the 7 nm nanocrystalline TiO_2 film. The scan rates are (from out to in) 10, 5, 2, 1, and 0.5 mV/s. (b) The b values calculated at different potentials by utilizing cathodic branches.[51]

As discussed in section 1.4, the energy storage behavior is also up to the structure of the materials. The following equation can be used to further separate the capacitive current from the total current, and to semi-quantitatively analyze the contribution proportions from the two parts of current.

$$\mathrm{i} = \mathrm{k}_1 v + k_2 v^{0.5}$$

Where *i* is the current at a fixed potential, *v* is the scan rate, and k_1, k_2 are the parameters obtained by fitting the data. The part of $k_1 v$ represents the surface-controlled current, and the $k_2 v^{0.5}$ represents the diffusion-controlled current.

Taking the different current contributions of TiO_2 nanoparticles with different particle sizes (7 nm, 10 nm, 30 nm) (**Figure 8**a&b), the ratio of the capacitive current significantly increases with decreasing the particle size. This phenomenon can be attributed to the much higher surface-to-volume ratio by decreasing the particle size. The high ratio of the capacitive current will lead to a better rate performance since a large proportion of redox reaction happens at surface/near-surface instead of inside the solid phase suffering from a slow ions intercalation process.

Overall, the energy storage behaviors of one particular faradic material are related to several aspects, such as the types or even the morphologies of active materials, and comprehensive methods should be used to understand the energy storage behaviors.

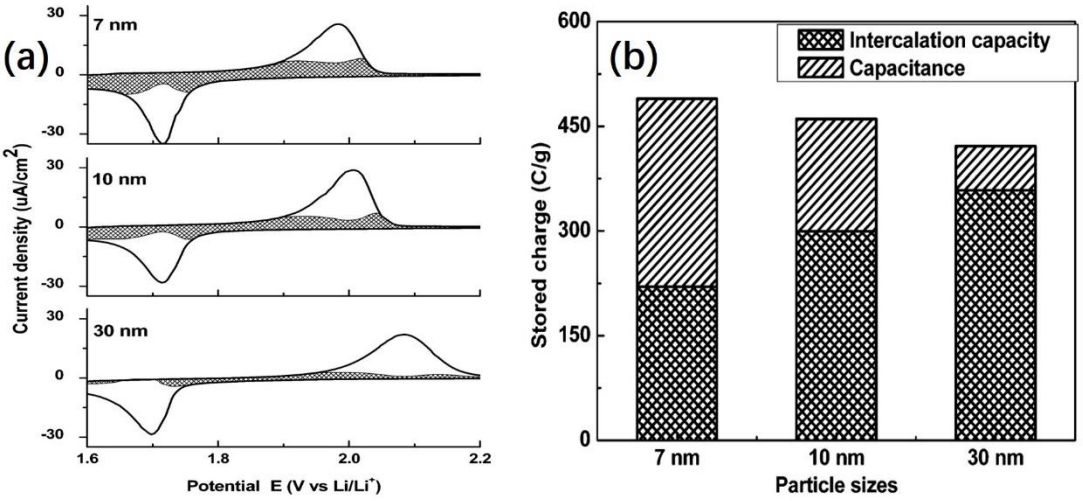

Figure 8. (a) Cyclic voltammetry curves of three TiO_2 films with different particle size (7nm, 10nm, 30nm) at scan rate of 0.5 mV s^{-1}. The total current (solid line) is obtained experimentally and the capacitive currents (shaded regions) are determined from fitting the data with the equation: $i = k_1 v + k_2 v^{0.5}$; (b) the different contributions of battery-type current and capacitive current from different TiO_2 particle sizes (7 nm, 10 nm, 30 nm).[51]

1.6 The research trend in the field of the energy storage electrodes

With the development of the nanoscience, the pseudocapacitive materials achieve a great balance between batteries and electrical double-layer capacitors, much higher capacity than carbon-based materials and much better rate performance than traditional battery electrodes. Despite the advantages, the energy storage devices based on the pseudocapacitive materials are not widely commercialized in the market yet, probably due to the poor rate-performance, high cost of electrode materials, lack of mass-production methods, and safety and environmental issues. Nevertheless, pseudocapacitive materials still have great potentials in the long-term prospective view. The common used pseudocapacitive materials are transition metal based materials (e.g. metal oxide,[52] metal sulfide,[53] and metal nitride[54] etc.), but their poor ions/electrons conductivity still restrict their energy and power output. In recent years, tremendous efforts have been made in the following ways to further improve their performance, so as to meet the market demands.

1.6.1 Improving the electron conductivity of faradic materials

Electron-conductivity is one of the most important cornerstones for the electrode materials and plays a crucial role in the view of energy storage performance. However, transition metal based faradic materials are always suffered from poor conductivity since their electronic structures are unfavorable to the mobility of electrons. To date, two main directions have been developed to improve the conductivity of faradic materials so that to accelerate the faradic reactions.

One way is to dope the faradic materials with heteroatoms, which can tune their electronic structure to facilitate the charge transfer process.[55] Taking the work of John Wang, et al. for an example,[56] their group synthesized a kind of sulfur-doped cobalt phosphide nanotube arrays through combining the hydrothermal method, and thermal-treatment method, schematically shown in **Figure 9**a**.** The impedance spectra have been

used to analyze the energy storage process and the result proves that the electron-conductivity of the material has been improved after doping sulfur inside (**Figure 9**b). Compared with that of pristine CoP, the sulfur-doped CoP gives a smaller x-intercept point in the high-frequency region and a smaller semi-circle in the mid-high frequency region, indicative of the lower internal-resistance and charge transfer resistance, respectively. The better conductivity can finally achieve an improvement in terms of the energy storage performance. As shown in **Figure 9**c, the sulfur-doped CoP can deliver a capacity of ~300 mAh g^{-1} at a current density of 1 A g^{-1} and remain 56% (156 mAh g^{-1}) at a high current density of 20 A g^{-1}. This energy storage performance is much better than that of the pristine CoP electrode——175 mAh g^{-1} at the current density of 1 A g^{-1} and 46% capacity retention at the high current density of 20 A g^{-1}. Not just limited to this example, tremendous studies have proved that the heteroatoms doping strategy is an effective tool to enhance the energy storage performance by increasing the conductivity of the faradic materials.[57–59]

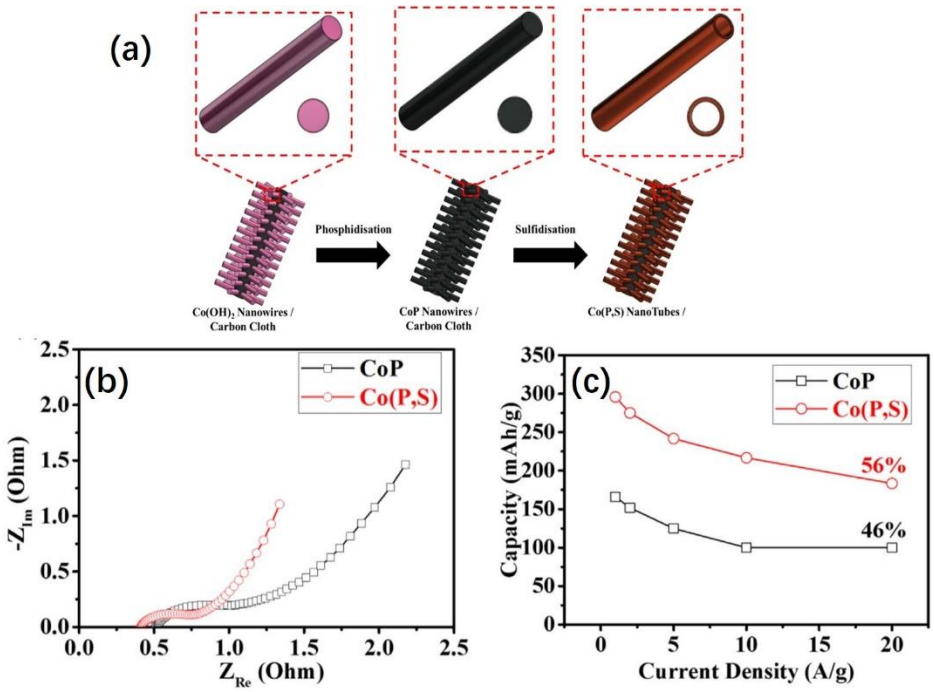

Figure 9. (a) Schematic illustration for the fabrication of sulfur doped CoP nanotube arrays on carbon cloth; (b) Impedance spectra of sulfur doped CoP and pristine CoP; (c) the rate performance difference between the sulfur-doped CoP and pristine CoP

Compositing faradic materials with other highly conductive materials (e.g., carbon-based materials or metals) can also alleviate the poor conductivity issue of the pure faradic materials. The difficulties of this approach are to optimize the ratio and the structure when configuring the composites. High ratio of the faradic materials will cause the electron conduction problem, but a high ratio of the conductive reagents, in turn, will lead to a loss of the capacity. Besides, the rational structure design of the composites is also important to make sure the efficient electron transfer throughout the entire interior of materials. For instance, Timothy S. Fisher et al. synthesized a graphene petal foam by chemical evaporation method and then electrodeposited Ni–Co hydroxide nanopetals on the surface of the foam to obtain the graphene petal foam/Ni–Co hydroxide nanopetals composites (GPF/NCHPs),[60] shown in **Figure 10**a. By controlling the electrodeposition time, they can receive a series of samples with different ratio of contents (longer deposition time will result in a higher proportion of the Ni-Co hydroxide). The SEM images of GPF/NCHPs, given in **Figure 10**b, reveal that the ultrathin graphene sheets with the hollow structure are interconnected, playing the electron-conduction role in the composite, and surface distributed Ni–Co hydroxide nanopetals act as the main active sites to store the energy, which should be very easy to accept/donate electrons from/to the graphene foam. This type of structure should be very favorable in the view of the energy storage. But, as discussed above, the ratio between the faradic materials and the conductive materials is crucial, and excessive loading of faradic materials will not be helpful to the energy storage performance. As shown in **Figure 10**c, if the deposition time longer than 3 min, the loading amount of Ni–Co hydroxide nanopetals getting higher, the rate performance of the composite gets worse and the capacities are even less than the sample with deposition time of 3 min at the high current density of 100 mA cm^{-2}.

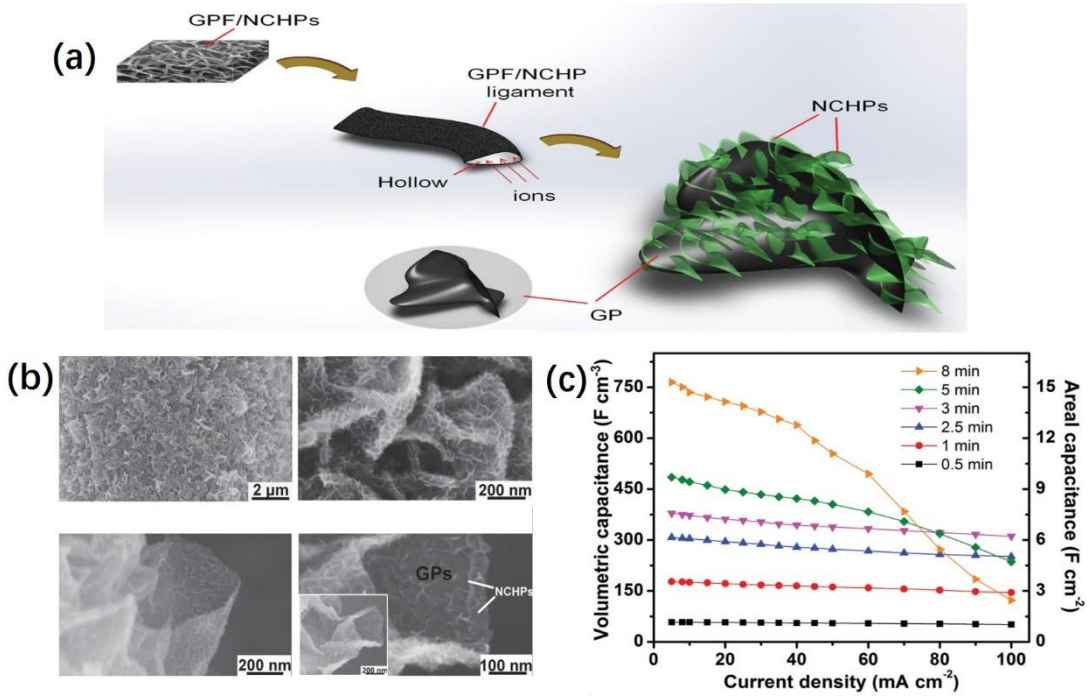

Figure 10 (a) Schematic illustration for the structure of the graphene petal foam/Ni–Co hydroxide nanopetals (GPF/NCHPs); (b) SEM images of GPF/NCHP with different magnifications; (c) Rate performance of the GPF/NCHPs with different ratio of the Ni–Co hydroxide nanopetals (longer deposition time means the higher proportion of the Ni–Co hydroxide nanopetals).[60]

1.6.2 Improving the ions conductivity of faradic materials

Besides the electron conductivity issue, the ions conductivity may also restrict the performance of the faradic materials. As well known, the counter ions compensation processes that neutralize the charge change of redox centers are indispensable to complete the faradic reactions and always become the rate-determine step. Therefore, rationally constructing ions diffusion channels to reduce the ions diffusion resistance is necessary to improve the performance (especially the rate performance) of faradic materials. In recent years, Yury Gogotsi et al., analyzed the relationship between structure and ions diffusion resistance through a single variable control experiment via preparing two titanium carbide electrodes (the chemical structure given in **Figure 11**a) with different structures.[61] From the SEM cross-section views of the two electrodes (**Figure 11**b&c), one electrode shows the compact layer-by-layer structure (labelled as

the hydrogel-electrode or HG-Ti_3C_2), but the other is highly porous (labelled as the Macroporous-electrode or MP-Ti_3C_2). In spite of the same chemical properties of the two electrodes, their energy storage behaviors are significantly different due to the different structure. Compared with that of HG-Ti_3C_2, the highly porous structure of MP-Ti_3C_2 is able to provide a much shorter ions diffusion pathway when the counterions diffuse inside the electrode during the redox reaction (illustrated in the insertions of **Figure 11**b&c**).** Therefore, the ions diffusion resistance inside the MP-Ti_3C_2 electrode is much smaller than that in HG-Ti_3C_2, even if the electrode thickness of MP-Ti_3C_2 electrode is ten times thicker than HG-Ti_3C_2. (See **Figure 11**d) Because of that, the energy storage behaviors of the two different electrodes are tested in 1M H_2SO_4 by cycling voltammetry. As a result, despite the similar capacities at low scan rates, much better rate performance can be observed for MP-Ti_3C_2 electrode **(Figure 11**e**)**, benefited from the much smaller ions diffusion resistance.

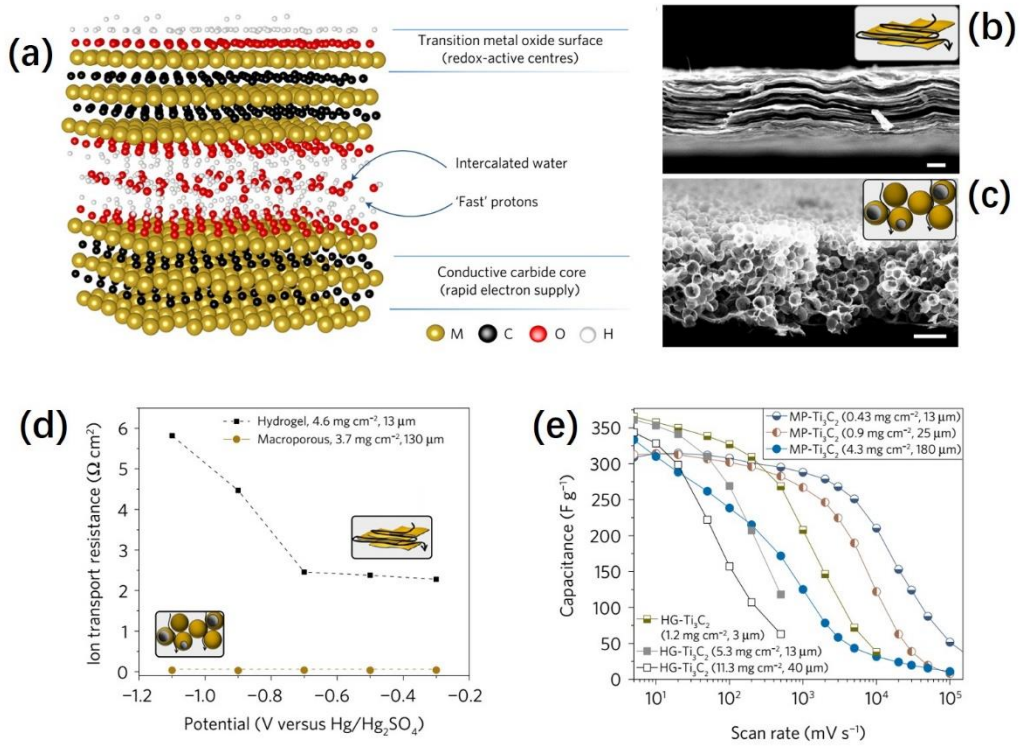

Figure 11 (a) Chemical structure of titanium carbide; the cross-section SEM images: (b) hydrogel-electrode (HG-Ti_3C_2) and (c) macroporous-electrode (MP- Ti_3C_2); (d) Ions diffusion resistance of HG-Ti_3C_2 and MP- Ti_3C_2; (e) Rate performance comparison between HG-Ti_3C_2 electrode and MP- Ti_3C_2 electrode.

Besides, constructing appropriate pore structures/reducing the size of material to increase the surface-volume ratio is also an efficient way to improve the ions diffusion during the redox reaction. There are two ion diffusion stages for the energy storage processes of faradic materials. The first stage is the counterions in electrolyte diffuse onto the interface of the faradic materials, and resistance of this process depends on the porous structure, as we discussed earlier. After this, the counter ions would further insert into the solid phase because the active sites in the bulk phase, especially in the near-surface region, also take part into the redox reaction. However, the ions diffusion inside the solid phase is orders smaller than that in liquid phase.[62,63] Therefore, minimizing the size of the materials to shorten the diffusion length inside the solid phase will be also helpful to reduce the ions diffusion resistance so that can improve the energy storage performance of the faradic materials. For example, Fengxia Geng et al. synthesized two different sizes of tungsten oxide (one with a diameter of ca.3 nm, labeled as Bulk; the other one with a diameter of ca. 1.5 nm, labeled as QDs) and further compared their energy storage behaviors.[64] Compared with Bulk electrode, The QDs electrode owns much faster ions diffusion, illustrated in **Figure 12**a, and much smaller peak-to-peak separations can be observed for QDs electrode, see **Figure 12**b&c, indicative of the more reversible redox reactions due to the reduced ions-diffusion distance in solid phase. The charge-discharge curves of the two electrodes are given in **Figure 12**d, and the two electrodes show very similar capacity at a low current of 0.2 mA. However, with the charge-discharge currents gradually increase, the capacity fades very fast for the Bulk electrode in comparison to that of QDs electrode. This phenomenon indicates the slow ions diffusion in solid-phase may become the rate-determine step at high currents/short charge-discharge time, and reducing the ions diffusion length in solid-phase is an effective approach to improve the performance of faradic materials.

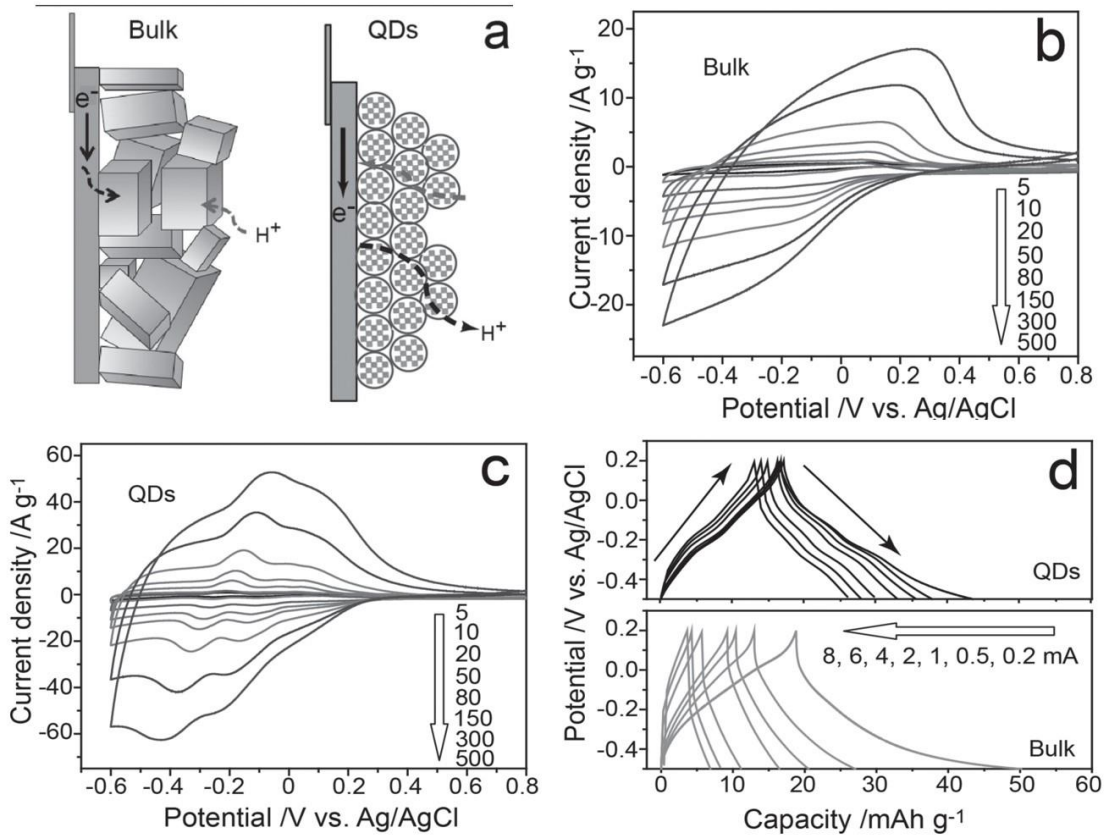

Figure 12 (a) Illustration of the ions transfer processes for the Bulk electrode and QDs electrode during the redox reaction; the cyclic voltammetry responses at different scan rates: (b) Bulk electrode and (c) QDs electrode; (d) Charge-discharge difference between QDs electrode and Bulk electrode.

1.7 Electron-hopping as the mechanism to achieve redox reactions

From the discussion above, we can see that the rate performance of traditional faradic materials depends on two aspects: electron movement rate inside the faradic materials and counterions diffusion rate inside the solid phase. However, the intrinsic electronic structure of most of them are close to isolator that is not favorable for the electrons to move and ions diffusion inside solid phase is very slow (the ions diffusion coefficient inside solid phase is ca.10^{-9} cm^2 s^{-1}) [62]. As discussed above, many strategies have been developed to improve these two aspects of the faradic materials, so that to enhance their energy storage performances. Nevertheless, think of it in another way, whether we can find a new redox manner so that to accelerate the ions/charges transport at same

time.

Back to the 1960s, the electron-hopping phenomenon was discovered, where the electrons can directly transport among active centers without physical connections,[65] The surface-tethered electroactive molecules with flexible linkers can undergo “fast” charge transfer reactions, as reported for self-assembled monolayers [66] or large dendrimers.[67,68] In the following decades, many studies have been done to analyze the electrons transfer behavior and found the distance between redox centers is a very important factor. For example, Christian Amatore et al. prepared two monolayer systems to study the electron-hopping process, and both molecules contain one terminal ferrocene molecule but with different length of hydrocarbon, as shown in **Figure 13**a&b.[69] By analyzing the peak separations during the cyclic voltammetry of the two systems at different scan rates, they found the redox kinetics could reach ca. 10^6 s^{-1} for both systems, which is much faster than that of traditional faradic materials. Besides, the monolayer system with shorter hydrocarbon chain would deliver faster kinetic due to the reduced distance for the ferrocene center. (Redox kinetic constant is 4×10^6 s^{-1} for the system in **Figure 13**a, and 2×10^6 s^{-1} for the system in **Figure 13**b) Compared with conventional redox manner, the electron-hopping mechanism can permit a much higher reaction rate due to the following two reasons. 1) the electron transfer speed is fast, which is not limited to the conductivity of the faradic materials but determined by the transfer speed of oxidation/reduction state of redox centers. 2) the fast counterions compensation rate because the ions diffusion rate in electrolyte is normally ca.10^4 orders higher than in solid phase.[62,63] Despite the great advantage of electron-hopping mechanism, however, as far as we knew, there is no relative work that introduces this mechanism to the energy storage field.

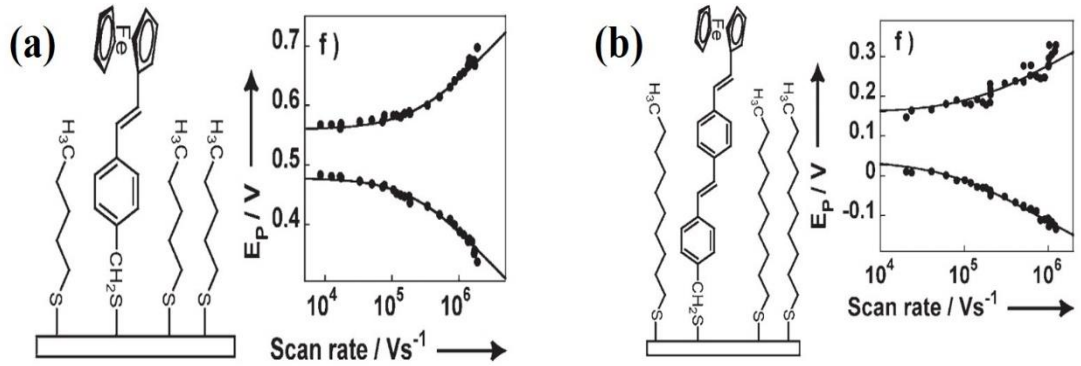

Figure 13. Evolution of the redox peaks separation during cyclic voltammetry at different scan rates: (a) Ferrocene derivate bearing one styrene unit; (b) Ferrocene derivate bearing two styrene units.

1.8 The fabrication of ordered mesoporous silica-based materials and their applications

The synthesis of ordered mesoporous silica materials started from last century,[70] and attracted broad research interest from scientists in the flowing years due to their intriguing characteristics such as large surface area, easy to control morphology and achieve the surface functionalization, high chemical stability and biocompatibility and low cost.[71] A series of novel mesoporous silica materials have been synthesized via using the surfactant micelle as the soft template including the family of SBA (SBA-1, SBA-6, SBA-15 and SBA-16 etc.),[72,73] FDU (FDU-1 and FDU-12 etc.),[74,75] MSU (MSU-G, MSU-H, and MSU-V etc.),[76,77] and KIT (KIT-1 and KIT-6).[78,79] They show incomparable advantages in many fields such as adsorption,[80] separation,[81] catalysis,[82] sensors,[83] biomedicine,[84] environmental protection,[85] and assisting synthesis of nanomaterials.[86] There is an important branch in the family of silica materials, namely self-assembled mesostructured silica films, which are expected to facilitate materials integration in devices (including the miniaturized ones) for target applications. The present work is based on redox active functionalized silica films and there are two main methods to prepare such films: 1)

Evaporation-Induced Self-Assembly method (EISA) method; 2) Electrochemically Assisted Self-Assembly (EASA) method.

1.8.1 Preparing ordered mesoporous silica film with EISA method

At the very beginning, the ordered mesoporous silica thin films were generated on the underlying substrates by the epitaxial growth process at gas-liquid interfaces,[87] liquid-solid interfaces,[88] or liquid-liquid interfaces.[89] However, the film fabrication process with these epitaxial growth methods always suffer from long-time deposition and unevenness problem etc.[90] Jeffrey Brinker et al. firstly proposed the EISA method,[91] which can significantly accelerate the film fabrication process. To be specific, first, a starting solution composed of ethanol, water, surfactant, and silane precursor is prepared, where the concentration of the surfactant does not reach the critical micelle concentration. Then, dip a substrate inside the solution and pull it out soon afterwards. The evaporation of the solvent will let the surfactant reach the critical micelle concentration to form a hexagonal, cubic or layered micelle, and the polycondensation of silane will occur surrounding the micelle generating the silica film on the surface of the substrate. The formation mechanism of silica film is illustrated in **Figure 14**a. From the TEM analysis, the structure of silica film is highly ordered with parallelly aligned cubic channels. (Cross-section view in **Figure 14**b and top-view in **Figure 14**c). A series of silica films with different channel structure can be easily prepared by changing the species/concentration of the surfactant via this approach. The discovery of this versatile method has prompted a lot with respect to the fabrication of ordered mesoporous silica film.

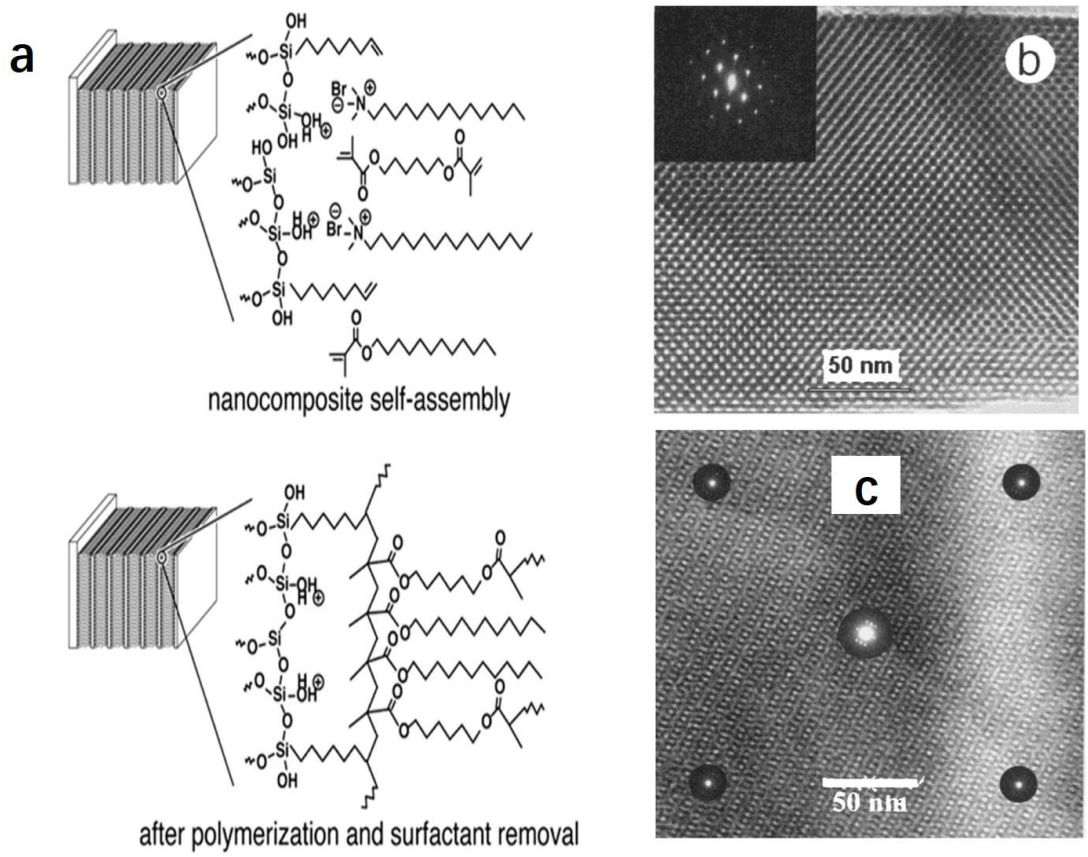

Figure 14. (a) Silica film formation mechanism by EISA method; The TEM images of the film: (b) cross-section view; (c) top-view.[91]

1.8.2 Preparing ordered mesoporous silica film with EASA method

Despite the great superiority of the EISA method, there are still some drawbacks due to the nature of the assembly process. In particular, the orientation of the mesochannels of silica films prepared with EISA method is always parallel to the substrate, which may hinder the mass transport inside the film.[92] Therefore, our group first reported an EASA method in 2007 to generate the vertically aligned mesoporous silica film on the conductive substrate.[93] The silica film can be easily prepared by applying a negative potential on the electrode that is immersed in the water/ethanol precursor solution containing certain amount of a cationic surfactant (CTAB) and the hydrolyzed silane. The applied negative potential will induce the self-assembling of the CTA^+ micelle orthogonal to the substrate and meanwhile generate hydroxide ions to catalyzing the polycondensation of hydrolyzed silane precursors around the surfactant on the surface

of the electrode. After aging at 130℃ overnight, the silica film with vertically aligned mesochannels can be finally prepared on the surface of the electrode. Different from the film prepared from EISA method, its hexagonally-packed channels perpendicular to electrode can be clearly seen from TEM images in **Figure 15**a&b. As illustrated in **Figure 15**c**,** in our following work, the functionalization of the vertically aligned mesochannels has been achieved by the click chemistry to introduce electroactive species onside.[94] (Note the precursor solution to prepare the silica film for the click reaction contains a certain amount of azido-substituted silane.) This kind of silica film owns the features of large surface area, vertically aligned mesochannels and electroactive species on the surface, which laid an important foundation for our work in this thesis.

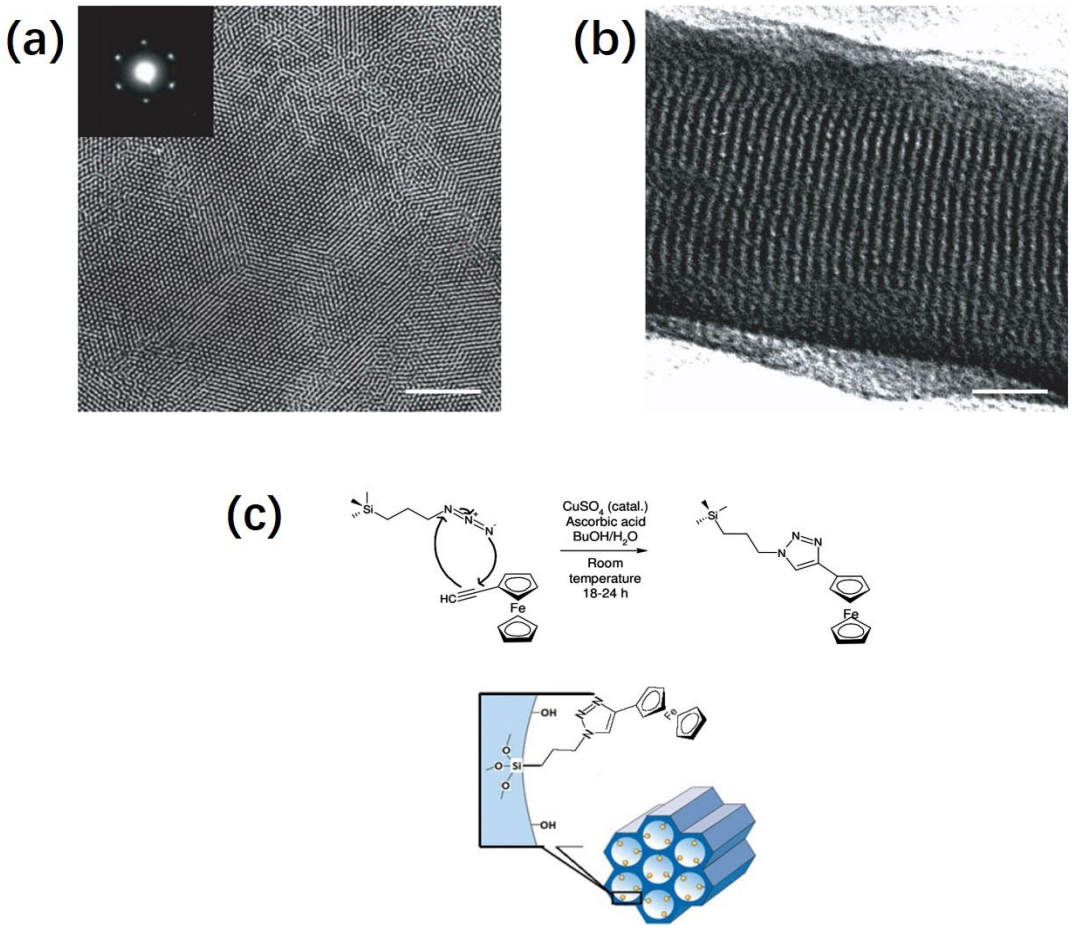

Figure 15. TEM images of the silica film prepared by EASA method: (a) top-view; (b) cross-section view; the illustration of achieving the surface functionalization of the silica film by the click chemistry.[93]

1.8.3 Different methods for the functionalization of silica materials

Besides the structure, the interfacial properties of silica also play a vital role with respect to certain applications. Several methods including: co-condensation, grafting, and click chemistry, have been established in recent years to tailor functional groups on the surface of silica materials. The co-condensation method can achieve the surface functionalization by adding a certain amount of silane derivates containing different functional groups in the starting precursor sol. In such sol, the silane and silane derivates could hydrolyze and condensate together, and finally incorporate the functional groups into the silica framework. For example, Mohamed Abboud et al. synthesized ferrocenylazobenzene-functionalized MCM-41 by adding 4-triethoxysilyl-3′-ferrocenylazobenzene into the TEOS sol, schematically shown in **Figure 16**a.[95] In contrast to the co-condensation method, grafting is a post-treatment functionalization strategy via utilizing the condensation reaction of the functional groups on the surface of silica. As shown in **Figure 16**b, Guangshun Wu et al. successfully grafts 3-aminopropyltriethoxysilane on silica surface via the reaction between the hydroxyl of silica and the ethoxy of 3-aminopropyltriethoxysilane. The functionalization approach of click chemistry is a combination of the grafting method and co-condensation method. Taking the azide-alkyne Huisgen cycloaddition (CuAAC) click reaction for an example, the azido (or ethynyl) groups are firstly introduced onto the silica surface by a co-condensation method, and then the corresponding ethynyl (or azido) containing molecules can be further grafted on the silica surface via the CuAAC click reaction with the catalysis of Cu^{+}. Compared to directly grafting process, the almost 100% conversion rate of click reaction [96] gives the possibility to control the amount of the functional groups onside the silica surface precisely. Moreover, the click reaction is versatile and can be easily carried out in both aqueous or organic solution under room temperature.[96] Thomas Bein et al. successfully bonds Trypsin on the surface of silica through the click chemistry strategy.[97] **(Figure 16**c)

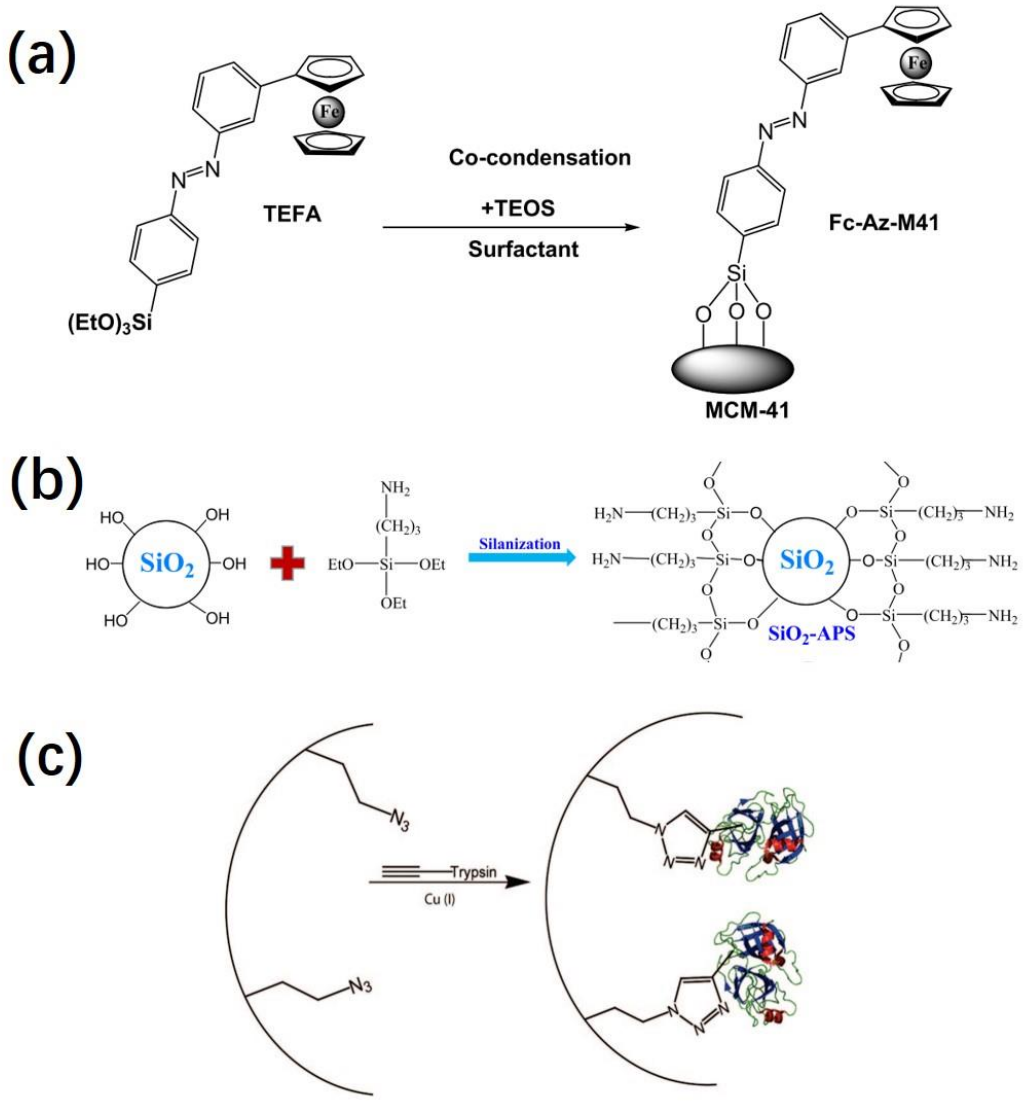

Figure 16. Functionalization silica through a co-condensation (a), grafting (b) and click chemistry method (c)

1.8.4 The applications of the vertically-aligned mesoporous silica thin film

The orientation of the channels has a significant effect on the ions transfer rate inside the film. Ions transfer rate inside the vertical channels is about one order of magnitude higher than that of parallel channels, and significantly better than that of non-ordered mesopores.[93] Therefore, the vertically-aligned mesoporous silica thin film and its derivates hold a great potential in terms of the applications including ions selectivity from size or charge differences, and sensors on the basis of ions accumulation effect. For example, Bin Su et al. prepared a positive charged vertically-aligned mesoporous silica thin film through the EASA method followed by a surface modification via grafting N-Trimethoxysilylpropyl-N,N,N-trimethylammonium chloride (TMAC). (**Figure 17**a) The positive charged vertical channels would form the electrical double layer inside, whose thickness can be controlled by adjusting the ionic strength of the solution, shown in **Figure 17**b&c. At a low concentration of the supporting electrolyte, the electrical-double layers would overlap in the meso-channels, and only anions can pass through the channels to reach the underlying electrode surface. At a high concentration of the supporting electrolyte, the shrinkage of the electrical double layer will occur, and leave free ions diffusion channels for both cations and anions. As a result, there is no redox current of cathodic $Ru(NH_3)_6^{3+}$ ions during the CV of the TMAC functionalized silica film in a relative low concentration of the supporting electrolyte (0.1M ~ 0.2 M acetate buffer solution). With increasing the concentration of the supporting electrolyte (0.4 M to 1 M), a gradually increased redox current can be observed but in a low current density (**Figure 17**d). But, this not the case for the anodic $Fe(CN)_6^{3-}$ redox probe, which shows a high intensity of redox current even in a 1 mM acetate buffer solution. These results can well confirm that the TMAC functionalized silica film can be used for the selective detection of anions. (**Figure 17**e) Our group also observed a similar phenomenon that the existence of the silica film prepared by the EASA method on the electrode could amplify the redox response of anions.[98]

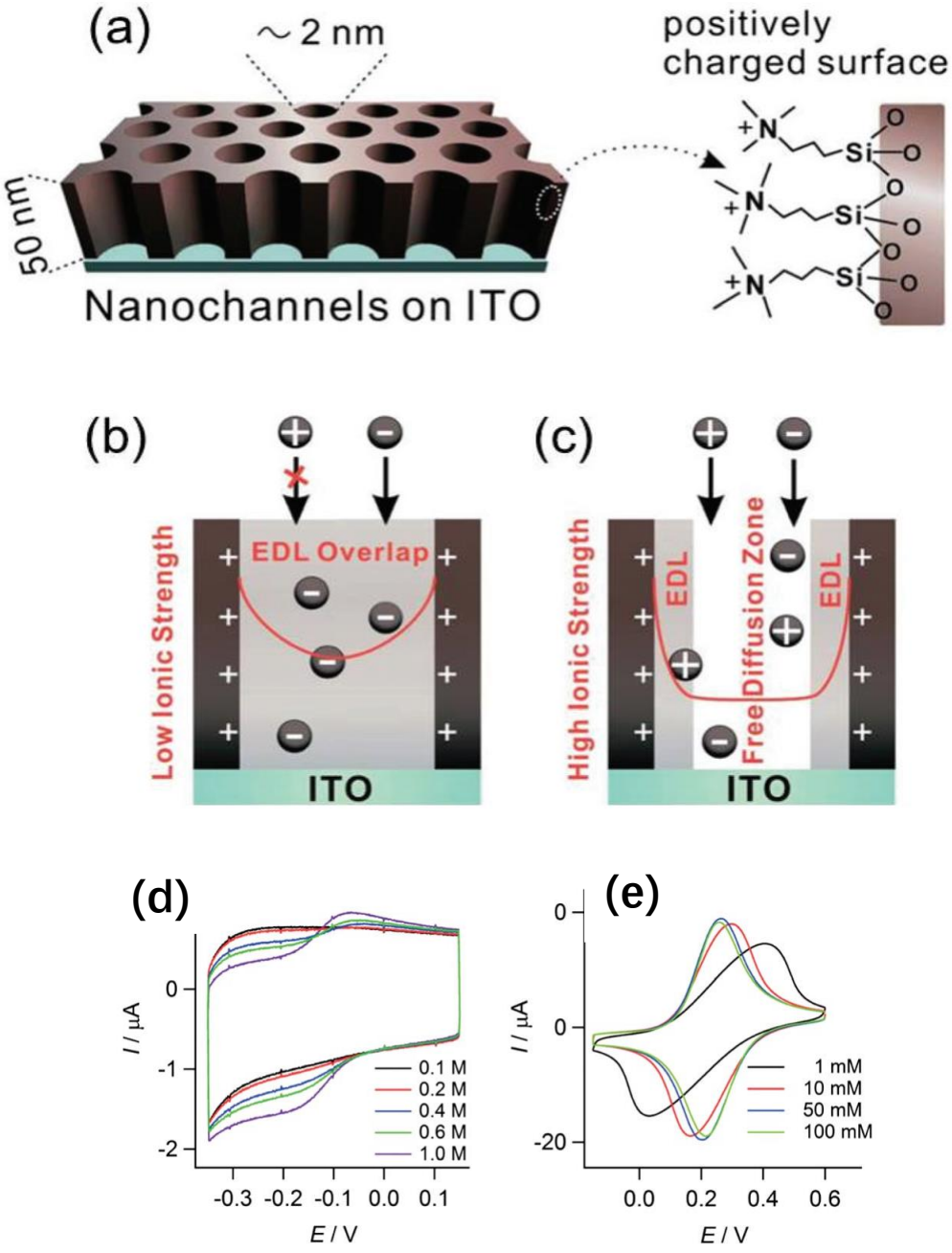

Figure 17. (a) The vertically-aligned mesoporous silica film modified with N-Trimethoxysilylpropyl-N,N,N-trimethylammonium chloride (TMAC) to obtain the positively charged surface. (b&c) The selectivity of cations and anions through adjusting ionic strength to control the thickness of the electrical double layer. (d&e) Voltammetric responses of the TMAC-functionalized silica film in aqueous solutions containing 30 mM $Ru(NH_3)_6^{3+}$ (d) and 30 mM $Fe(CN)_6^{3-}$ (e) and various concentrations of acetate buffer at a scan rate of 50 mV s^{-1}.

Our group has also established a silica film assisted cations sensor with an enhanced sensitivity due to the cations accumulation inside silica channels.[99] The vertically-aligned mesoporous silica film is firstly generated on the glassy carbon electrode (GCE) via EASA method. The negatively charged surface of the silica film at higher pH (i.e. 6) could adsorb cations inside the meso-channels in the form of the electrical double layer, and the higher concentration of cations would lead to a intense current during the cyclic voltammetry. Taking the Paraquat cations as an example (**Figure 18**a), the anodic peak current reaches ca. 60 μA after coating the silica film on the GCE, which is 4 times higher than that on bare GCE electrode. Besides, the detection of the Paraquat by the silica film coated electrode also shows a linear current increase with concentration, showing a much better sensitivity of (-7.79 ± 0.27) A M^{-1} for the modified electrode against a relative poor sensitivity of (-0.32 ± 0.01) A M^{-1} for the bare electrode.

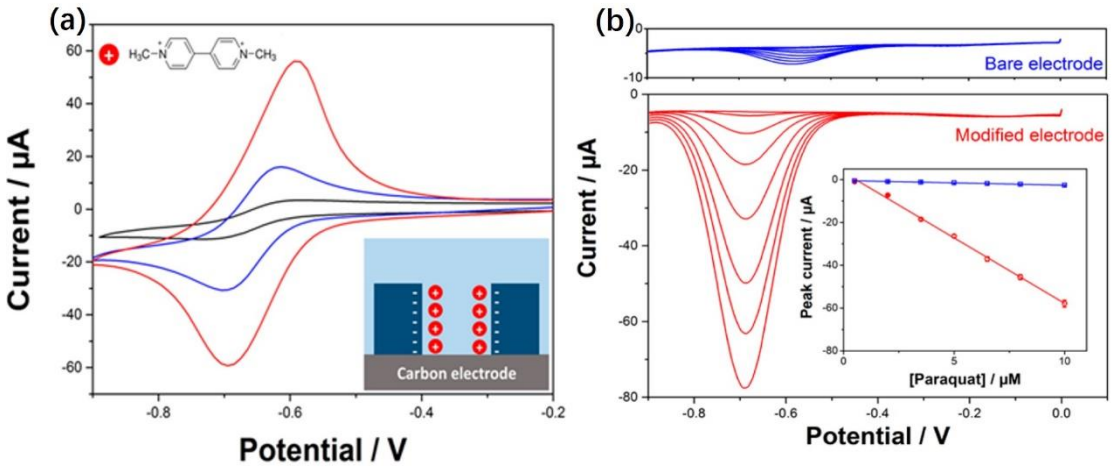

Figure 18. (a) Cyclic voltammetry of 0.5 mM of Paraquat at a bare GCE (blue), GCE modified with the mesoporous silica film before (black) and after (red) template extraction. ν = 100 mV s^{-1}; (b) Square wave voltammograms of 0.5-10 μM paraquat at bare (top, blue curves) and modified (bottom, red curves) GCE. Inset shows calibration curves. Background electrolyte: 0.1 M NaCl, pH 6.

In the category of electrochemistry, such silica films have attracted tremendous research interest as electrochemical sensors, but their potentials in energy storage field are long-time over looked due to their insulating nature. However, in contrast to the carbon based

materials (widely used as energy storage materials), such silica films own inimitable structural advantages including well-organized structure, large surface area, and high flexibility for their surface functionalization. Taking the silica film prepared from the EASA method as an example, the vertical-aligned mesoporous silica thin films possess uniform mesopores with size of ca. 2 nm in diameter, a high pore density of 75 000 μm^{-2} and highly ordered vertical channels. These films should be the potential candidates as energy storage materials after tackling the electron-conduction problem.

Chapter II

Electron-Hopping System Constructed with Vertically-Aligned Mesoporous Silica Films: The Potential and Influence Factors for Energy Storage Applications

2.1 Introduction

Improved energy storage devices with higher energy density, better rate capability and prolonged lifespan are ever urgently needed for the keep surging demands. Supercapacitors featuring high power density and short charge-discharge time appear as a competitive candidate.[100–102] Two types of materials (i.e., carbonaceous or related electrically conductive materials and faradic materials) with their respective advantages and limitations are typically used as the electrodes. Carbonaceous materials own large surface area and good conductivity, but charges can be stored only through physical accumulation at the electrode-electrolyte interfaces (double-layer process), restricting the energy density and some practical applications of such electrical double layer capacitors, even if the use of nanomaterials and/or nanostructured materials can help to circumvent this problem somewhat.[56,103,104] By contrast, faradic materials can store more charges through faradic reactions, but the slow reaction rates (both in terms of electron transfer kinetics or diffusional limitations) restrict their power output, even if some strategies are proposed to improve the performance of such so-called pseudocapacitive materials.[105–108] These materials are also of interest for being used in battery-capacitor hybrid devices.[109–111] As such, seeking a way that could accelerate the redox reactions in pseudocapacitive materials to the extent of the double-layer processes would be of great help to solve the paradox between the energy and power density.

On the basis of our understanding of these technical needs, a system based on an electron-hopping mechanism between redox adjacent sites inside an ordered, large

surface area and transparent matrix may have the potential to improve the charge transfer processes. Different from the traditional electron transfer mechanism where the physical contact between the redox sites is required, the electrons can freely transfer between the close but separated adjacent redox centers through an electron-hopping process (as that operating in redox polymers,[112] for instance). As investigated for self-assembled monolayers on electrodes, the kinetics of this electron hopping mechanism has been proven efficient enough as far as the active sites are close enough.[113] However, the limited amount of active sites of monolayer-based systems restrict their energy density, and the implementation of redox molecular junctions in large-scale and three-dimensional assemblies remains challenging, especially in view of avoiding other possible charge transfer ways (e.g., translational motion of polymer chains in redox-active supramolecular systems[114]). To best our knowledge, there is no related work that systematically assesses the value and potential influence factors of molecular electron-hopping processes in the energy storage field.

Our group has established an Electro-Assisted Self-Assembly (EASA) method to generate thin layers of vertically-aligned mesoporous silica on various conductive substrates,[92,93] and further achieved their surface functionalization by the click chemistry (Copper-catalyzed Azide-Alkyne Cycloaddition, CuAAC)) to introduce large amounts of organic groups onto the internal silica walls.[115,116] Introducing redox active centers in such system, the resulting rigid organic-inorganic hybrid becomes electroactive and electron-hopping becomes the only possible way to conduct the electrons among the redox centers due to the isolating nature of the silica walls.[1] Furthermore, the density of the redox molecules in the film can be adjusted by varying the components of the precursor solution.[115] Both features make such thin, ordered and oriented organic-inorganic hybrid film an ideal platform to evaluate the interest of the electron-hopping process in offering possibilities to construct new types of energy storage materials. This is what we have investigated here on the basis of electrodes modified with mesoporous silica films generated by EASA and functionalized with metallocene redox centers (ferrocene, cobaltocenium).

2.2 Experimental section

Preparation of AzPTES: The (3-azidopropyl) triethoxysilane (AzPTES) precursor was synthesized from the reaction between (3-chloropropyl)trimethoxysilane and sodium azide in the presence of tetrabutylammonium bromide.[116],[117] Its preparation was achieved by adding 2.0 g Cl-PTES, 1.08 g NaN_3 and 1.29 g TBAB in 100 mL ACN, which was stirred and refluxed at 90°C for 24 h under nitrogen atmosphere. Then, the ACN solvent was removed by rotary evaporation at 80°C under a reduced pressure of 0.2 bar. The residual mixture was suspended in cyclohexane and filtered with filter paper. The remaining cyclohexane was removed using the rotary evaporator as above and the oily AzPTES product can be finally obtained. Yield: ~1.3 g, 65 %. ^{1}H NMR (400 MHz, $CDCl_3$, δ): 0.66 (t, 2H, J = 0.85 Hz), 1.21 (t, 9H, J = 6.88 Hz), 1.66-1.73 (m, 2H), 3.25 (t, 2H, J = 7.16 Hz), 3.80 (q, 6H, J = 6.88 Hz).

Preparation of the ferrocene functionalized mesoporous silica (Fc-MS) thin films: The precursor sol for the deposition of the azido-containing silica films was prepared with the following procedure. Firstly, the silane sol was prepared by adding 120 mM TEOS and 80 mM AzPTES (the molar ratios of Az-PTES/TEOS can also be adjusted to different ratio e.g., 20%, 60%) in a solution containing 20 mL ethanoland 20 mL water with 0.1 M $NaNO_3$. Then, 1.35 mmol CTAB was added under stirring and the pH was adjusted to 3 by using 0.1 M HCl aqueous solution. The resulting sol was stirred at room temperature for 2.5 h for ageing.

The azido-containing silica films were grown on ITO electrode via a potentiostatic method by applying a cathodic potential of -1.3 V (vs. Ag wire pseudo-reference) on the electrodes that are immersed in the prepared sol for 20 s. The obtained azido-containing silica film can be further functionalized by a copper(I)-catalyzed alkyne-azide cycloaddition (CuAAC) click reaction to covalently introduce the electroactive species onside the surface of silica surface. Typically, several pieces of samples

containing the azide silica film were putted in inside a mixed-solvent medium (8 mL H_2O + 12 mL DMF) containing 3.5 mg copper sulfate, 7.5 mg ascorbic acid and 10 mg ethynylferrocene for 24 h in dark. After that, several samples were collected and rinsed with 1 mM sodium diethyldithiocarbamate trihydrate ethanol solution to remove the remaining copper catalyst and the ferrocene functionalized silica film can be finally obtained. Several kinds of samples containing different amount of ferrocene molecules were prepared by adjusting the ratio between the AzPTES and TEOS in original precursor solution. The samples derived from precursor solutions of 40 mM AzPTES/160 mM TEOS, 80 mM AzPTES/120 mM TEOS, and 120 mM AzPTES/80 mM TEOS were labelled as Fc-MS-20, Fc-MS-40, Fc-MS-60, respectively. (The higher ratio of AzPTES in the precursor solution means higher density of azide groups in the silica film, resulting in the higher density of ferrocene molecules after the click reaction.)

Preparation of a cobaltocenium functionalized mesoporous silica (Co^+-MS) thin film： A Co^+-MS-40 film was prepared similarly as the Fc-MS-40 sample, but by replacing ethynylferrocene by the ethynylcobaltocenium molecule,[118] to get the surface of the silica channels covered with covalently-bonded cobaltocenium moieties.

Preparation of the graphene counter-electrode: The graphene oxide (GO) was prepared from graphite powder following the classical Hummers' method.[119] The graphene electrode was prepared by the electrophoretic deposition of GO onto ITO, by applying -1.2V (vs. Ag/AgCl) to the ITO electrode for 30s in 30 mL solution containing 50 mg GO and 0.32 g $LiClO_4$ as supporting electrolyte.

Preparation of the asymmetric solid-state device*:* A PVA/LiCl gel was prepared by dissolving 6.37 g LiCl and 3 g PVA in 37 mL water at 90 ^oC.[120] The device was assembled with a sandwich configuration by using the Fc-MS-40 (1 cm^{-2}) as the cathode, the graphene electrode (1 cm^{-2}) as the anode, and a PET plate (thickness ~1 mm) with a hole in the center as separator. Several droplets of the PVA/LiCl gel were added between the two electrodes and several clamps were used to fix the device.

2.3 Results and discussions

2.3.1 Main characteristics of the ferrocene-functionalized mesoporous silica films

The overall preparation of ferrocene-functionalized vertically-aligned mesoporous silica thin films is schematically illustrated in **Figure 1**, involving the EASA generation of an azide-functionalized silica membrane onto the ITO surface, which is further derivatized with ferrocene units by copper-catalyzed azide-alkyne Huisgen reaction.

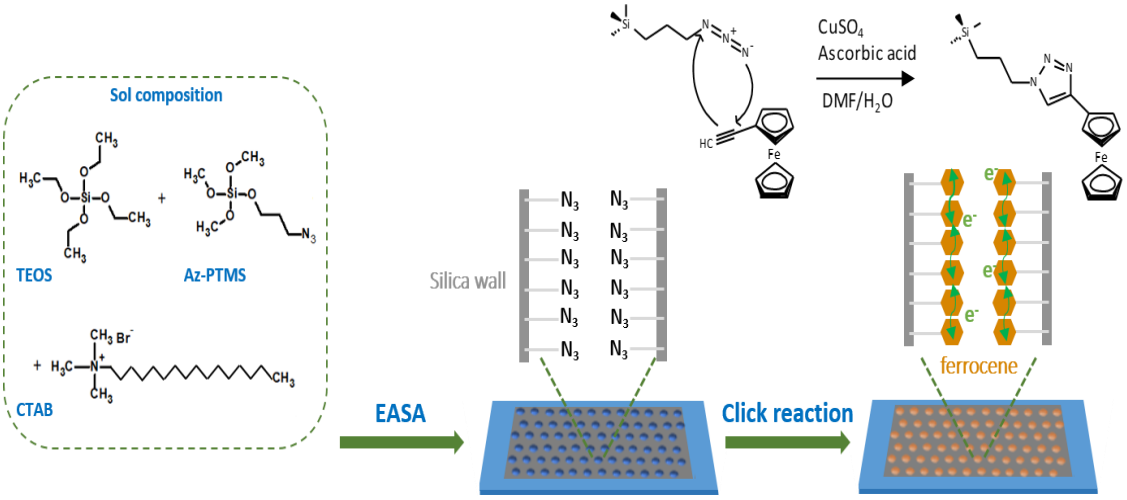

Figure 1. Schematic illustration of the preparation process of the ferrocene-functionalized vertically-aligned mesoporous silica thin films on a piece of flat ITO electrode. After hydrolysis of the silane precursors the azide-functionalized silica thin films are further functionalized with ferrocene units by copper-catalyzed azide-alkyne Huisgen reaction.

The main structural characteristics of the ferrocene-functionalized silica thin film prepared with 40% AzPTMS + 60% TEOS precursors (Fc-MS-40) are shown in **Figure 2**. Top view TEM micrographs (**Figure 2**a) indicate a highly porous film composed of fairly ordered hexagonal mesopores, as also identified by the hexagonal diffraction spots of the corresponding Fast Fourier Transformation (FFT) diffractogram. The cross-section view of the sample (**Figure 2**b) further reveals the vertical channels run directly from the top to the bottom of the film, and the thickness of the film is ~105 nm, a value

which was also confirmed by profilometry. Grazing Incidence Small Angle X-ray Scattering (GISAXS) is further used to analyze the internal structure of the film in order to obtain the statistically averaged lattice information. Two sharp diffraction spots can be observed in the equatorial plane of the scattering in (**Figure 2**c), indicating the long-range ordered perpendicular structure of the film, along with a very shallow ring in-plane arising from few silica beads with wormlike mesostructured on the film surface (as commonly observed for films prepared by EASA.[121,122]) Moreover, the q_y value of 1.81 nm^{-1} can be obtained by measuring the distance between the light source and the diffraction spots (**Figure 2**f). This value can be used to calculate the lattice spacing, d, of the structure using the equation $d = 2\pi/q$,[123] giving rise to a d value equal to 3.47 nm, which is consistent with TEM results.

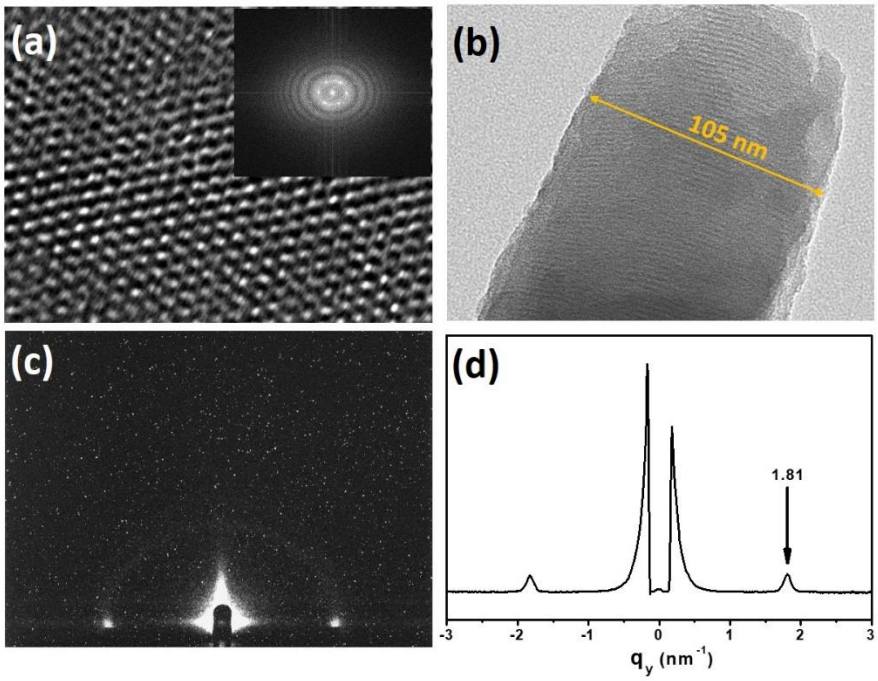

Figure 2. Structural characterization of the Fc-MS-40 film. TEM micrographs: (a) top views, (b) cross-section view, and corresponding FFT pattern (inset in (a)); (c-d) GISAXS pattern and corresponding fitting curve.

Similar mesostructure characteristics can be observed for the less functionalized Fc-MS-20 film, in agreement with previous observations,[94] whereas the film generated from a sol containing 60% of the organosilane AzPTMS (Fc-MS-60) was no more

ordered (because of interference in the self-assembly of the mesophase structure[124]), as illustrated in **Figure 3**.

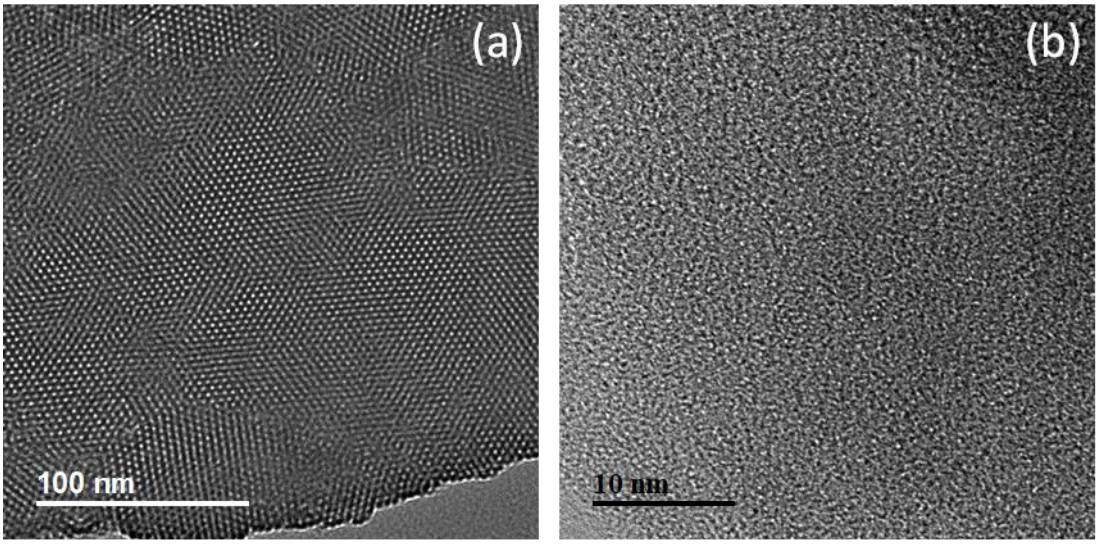

Figure 3. (a) The TEM micrographs of Fc-MS-20, and (b) Fc-MS-60.

The incorporation of the organic groups and effectiveness of click coupling with ferrocene moieties can be checked by infrared spectroscopy (IR). Comparing the evolution of the azide signature (stretching asymmetric band located at 2095 cm^{-1}) in the IR spectra for samples prepared from sols containing 20 to 60% AzPTES (**Figure 4a**) clearly indicates the presence of increasing amounts of azide groups. After the click reaction (**Figure 4b**), the area of this absorption band decreased by 85% (for Fc-MS-20), by 79% (for Fc-MS-40) and by 75% (for Fc-MS-60), confirming that a large part of the azido groups took part in the click reaction (100% yield cannot be reached for steric hindrance reasons). The formation of triazole units incorporating ferrocene functions can be also noticed on the figure, via their characteristic band located at 1610 cm^{-1}, yet located in a noisy region of the spectra. Overall, the ferrocene molecules are successfully anchored to the silica walls through covalent bonding as expected, proportionally to the amount of azide groups in the starting material.

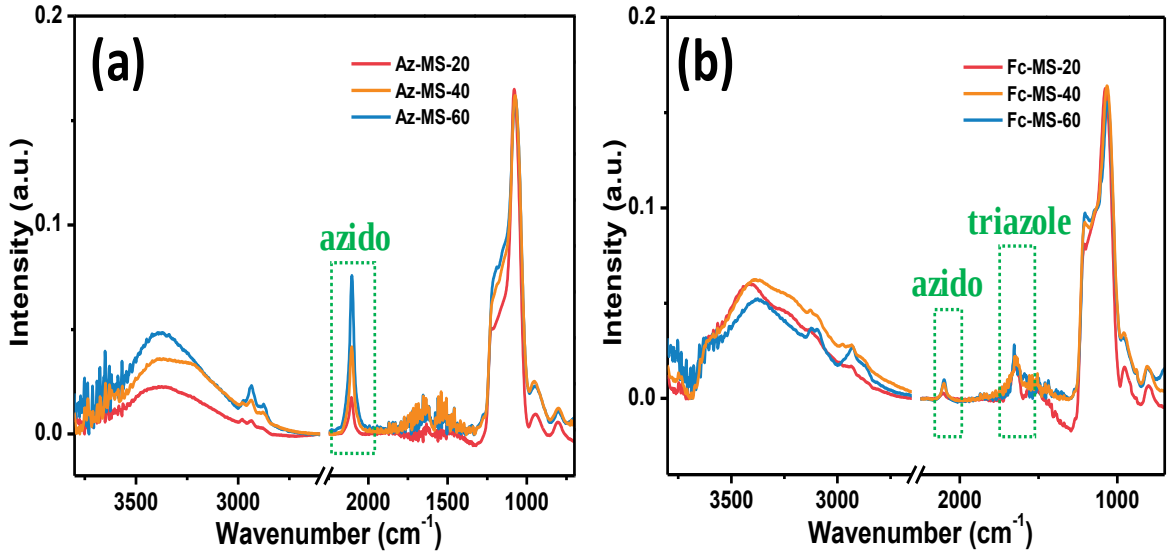

Figure 4. (a) IR spectra of Az-MS-20, Az-MS-40 and Az-MS-60; (b) IR spectra of Fc-MS-20, Fc-MS-40 and Fc-MS-60 (i.e., after click coupling of Az-MS samples). All spectra have been normalized based on the characteristic silica band at 1070 cm^{-1}.

2.3.2 Electrochemical characterization of the ferrocene-functionalized films

The energy storage performance of the as-prepared Fc-MS samples was first evaluated by cyclic voltammetry (CV) in 1 M LiCl aqueous solution. Comparing the CV curves recorded at a scan rate of 5 mV s^{-1} for samples bearing various ferrocene contents (**Figure 5**a) reveals the absence of any noticeable electrochemical signal for the azide-functionalized film (*i.e.*, without ferrocene grafted onto the silica walls) while well-defined redox peaks, yet significantly distinct in shape, can be observed in the potential window from 0.0 to +0.6 V *vs.* Ag/AgCl for the Fc-MS films. Clearly, the best performance is achieved for Fc-MS-40 (*i.e.*, prepared from 40% AzPTES and 60 %TEOS as silane precursors), from both points of view: (i) smaller anodic-to-cathodic peaks separation and (ii) larger peak currents. This can be explained taking into account the electron transfer mechanism involving the electron hopping between adjacent ferrocene sites attached to the insulating silica film and associated counter-anions transport through the mesopore channels to maintain electroneutrality (Eq. 1):[1]

$$Fc - 1\,e^- + X^-_{(sol)} \Leftrightarrow Fc^+,X^-_{(film)} \quad (1)$$

(with Fc = ferrocene; Fc^+ = ferricinium; X^- = counter-anion; sol = solution)

In doing so, the Fc-MS-40 sample is characterized by the most attractive energy storage behavior, exhibiting an almost ideal surface-controlled redox reaction (with a pair of intense bell-shaped peaks located at +0.35 V vs. Ag/AgCl, with a peak-to-peak separation of 12 mV). This is due to the large density of redox-active sites in the material enabling efficient electron hopping between close together ferrocene molecules uniformly distributed on the mesopore walls and easy transport of charge-compensating ions thanks to the regular and oriented mesostructure. By contrast, the Fc-MS-20 sample containing a lower amount of ferrocene (nearly twice as less as Fc-MS-40) not only resulted in (expected) lower peak currents (by almost two times) but also resulted in less reversible diffusion-limited signals (peak-to-peak separation equal to 70 mV) arising from redox sites located at a longer distance between each other (slower pseudo-diffusion of the electrons in the hopping mechanism).[125] On the other hand, the sample with more ferrocene loading amount (*i.e.*, Fc-MS-60 prepared from 60% AzPTES and 40 %TEOS as silane precursors) also exhibited a smaller current response and the redox peaks shifted to higher potential values (*i.e.*, +0.38 V, with a peak-to-peak separation of 28 mV). This can be explained by the loss of mesostructural order (**Figure 3**b) and steric hindrance limiting the number of electrochemically accessible ferrocene molecules in the film and slowing down the charge compensation process (Eq. 1). Similarly, a nonordered film prepared by drop coating did not give any noticeable signal for ferrocene, confirming again the interest of EASA to provide highly electroactive mesoporous films. The Fc-MS-40 film was thus chosen as the most appropriate for energy storage application, and used exclusively afterwards. Note however that increasing the potential scan rate contributed to induce charge transfer limitations in the Fc-MS-40 film (**Figure 5**b), the fast thin-layer behavior being maintained up to 20 mV s^{-1} and then becoming more and more rate-limited at faster scan rates (**Figure 5**c).

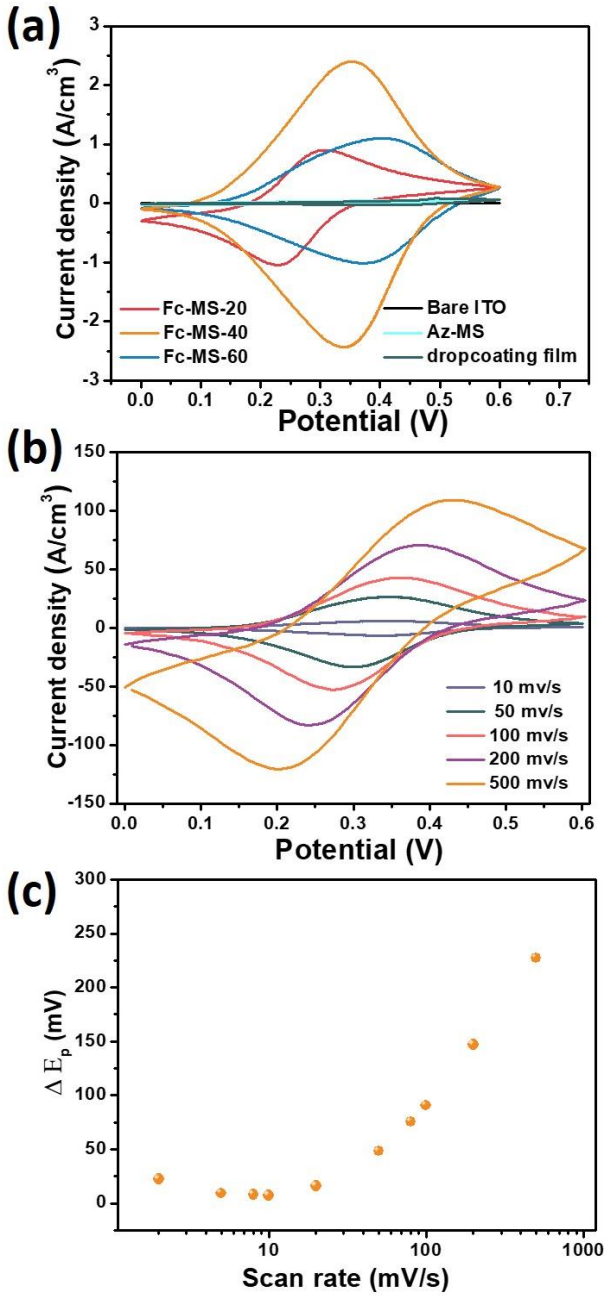

Figure 5. (a) Comparison of the CV curves recorded at of 5 mV s^{-1} in 1 M LiCl using bare ITO and ITO electrodes coated with Fc-MS-20, Fc-MS-40, Fc-MS-60, Az-MS and a ferrocene-functionalized film prepared from drop-coating method; (b) CV curves of the Fc-MS-40 film at scan rates varying from 10 to 500 mV s^{-1}; (c) Variation of the anodic-to-cathodic peak separation for Fc-MS-40 as a function of the potential scan rate (in the 2 mV s^{-1} to 500 mV s^{-1} range).

In order to evaluate the energy storage performance, the galvanostatic charge-discharge curves of Fc-MS-40 were recorded at various current densities from 0.4 to 20 A cm^{-3} (**Figure 6**a). Different from the typical triangular curve of double-layer capacitance, the charge/discharge curves are distorted but with no clear platform (the sign of a battery behavior). This phenomenon can be explained by the fast surface redox reaction without limitation of the diffusion process.[126] Besides, the similar charge and discharge time also proves that there is no side reaction, and almost all stored charges can be released during the discharge process. The capacities are calculated based on the galvanostatic charge-discharge curves and expressed as a function of current density (**Figure 6**b). The Fc-MS-40 film can deliver a capacity of 105 C cm^{-3} (1.10 mC cm^{-2}) at the current density of 0.4 A cm^{-3} and the capacity retention can achieve 48% (50.4 C cm^{-3}) at the current density of 20 A cm^{-3} (2.8 s charging time).

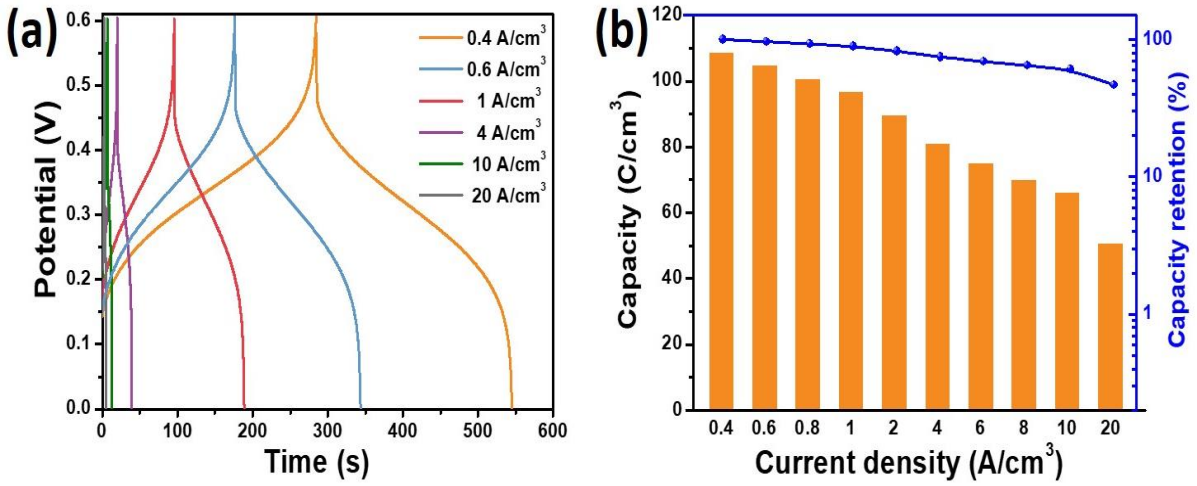

Figure 6. (a) Charge and discharge plots of Fc-MS-40 at various current densities from 0.4 A to 20 A cm^{-3}; (b) Specific capacity *vs.* current density plots of Fc-MS-40;

By contrast, the capacities of Fc-MS-20 and Fc-MS-60 were lower than that of Fc-MS-40 at the same current density (**Figure 7**), confirming the most attractive features of Fc-MS-40. Besides, the onset potentials for the energy storage process of Fc-MS-20, Fc-MS-40, and Fc-MS-60 are consistent with the redox peaks of the CV results.

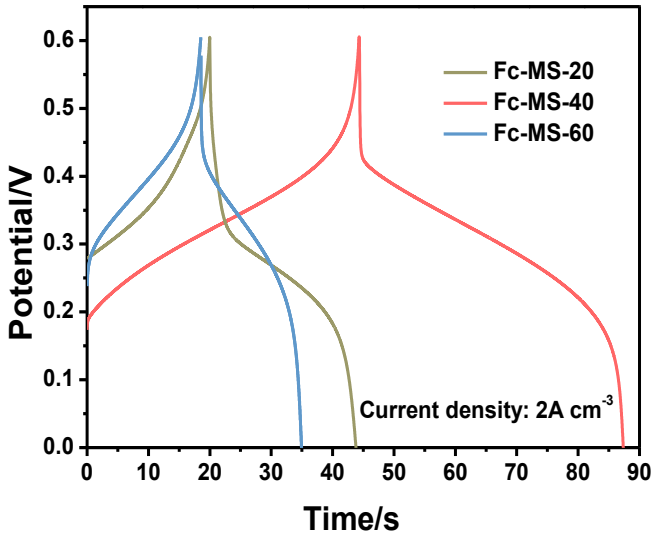

Figure 7. Charge-discharge curves of FcMS-20, Fc-MS-40 and Fc-MS-60 samples recorded at a current density of 2 A cm^{-3}.

The Fc-MS-40 film electrode also exhibits a robust cycling performance with 75% capacity retention after 1,000 successive CV cycles at a scan rate of 200 mV s^{-1} (**Figure 8**a) owing to the durability of covalently bonded ferrocene molecules. The Fc-MS-40 also exhibits a good volumetric energy density, when compared with similar thin-film systems reported in literatures (**Figure 8**b). Due to the large surface area of the vertically-aligned mesoporous silica film, a high density of ferrocene molecules can be obtained in Fc-MS-40 (~1 mmol cm^{-2}, calculated on the basis of charge storage ability), resulting in a superior charges storage ability. Overall, the novel electron-hopping based redox material shows competitive energy storage performance, compared with traditional carbon-based or faradic materials.

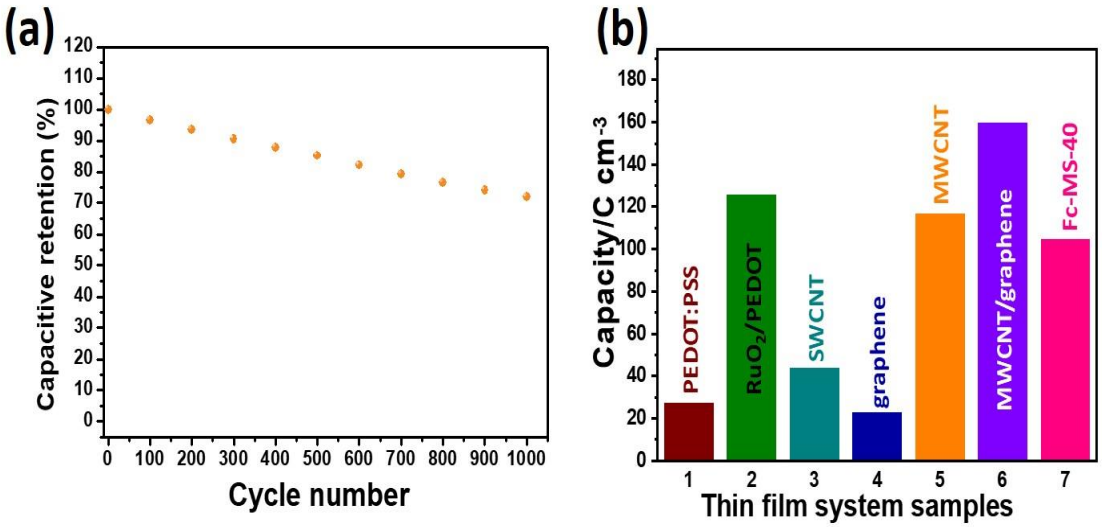

Figure 8. (a) The cycling performance of Fc-MS-40 at scan rate of 200 mV s^{-1}; (b) Comparison of volumetric energy density of Fc-MS-40 with other materials: PEDOT:PSS,[127] RuO_2/PEDOT,[128] SWCNT,[129] Graphene,[130] MWCNT,[131] MWCNT/Graphene.[132]

Electron-hopping is the only way to transfer electrons in our system because of the insulating character of the silica walls (the resistivity of silica is very huge, ranging from 10^{12}~10^{14} Ω/cm)[133]. A control experiment has further been done to prove that. As shown in **Figure 9**, compared with that of bare ITO electrode, the signals of the $Ru(NH_3)_6^{3+}$ redox species in solution is absent when the electrode surface is covered with a surfactant-templated mesoporous silica film. In such electrode, the silica film blocks the ITO surface and the silica film becomes the only interface that can contact the $Ru(NH_3)_6^{3+}$ redox probe in solution. The disappearance of the $Ru(NH_3)_6^{3+}$ redox signal demonstrates that silica layer coated on the surface of ITO electrode is isolated and cannot transfer electrons. Therefore, the redox reaction of ferrocene molecules in Fc-MS can only take place through the electron-hopping process—the redox species (ferrocene/ferrocenium here) near the ITO surface are oxidized/reduced first and then transfer to the adjacent molecules until propagate to the whole system with the help of the vertically-aligned channels.

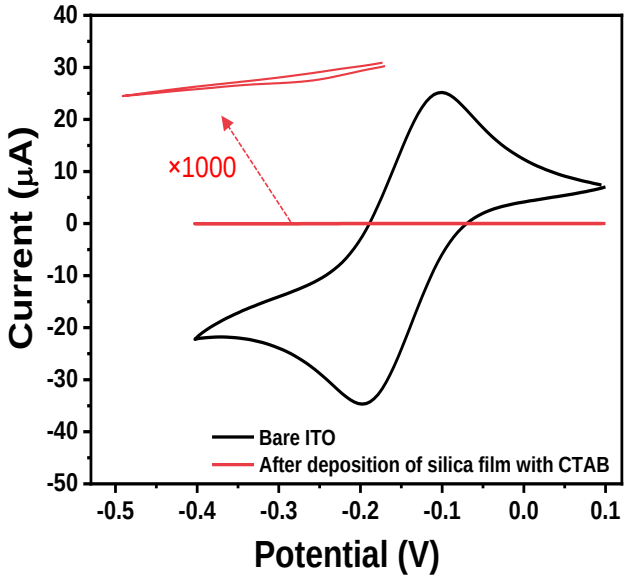

Figure 9. Cyclic voltammograms recorded in 1 mM $Ru(NH_3)_6^{3+}$ using either bare ITO electrode or a mesoporous silica-coated electrode, at a scan of 50 mV/s.

In the goal to characterize the electron-hopping processes in a more quantitative way and to determine the possible influence factors, one can go deeper in the analysis of the CV curves of ferrocene-functionalized silica films recorded at different scan rates (**Figure 10**). First of all, the redox peak currents (i) vs. scan rates (v) are fitted with the equation of $i = av^b$, where the empirical b value is an indicator of the energy storage behavior. If b value is equal to 0.5, it means that the energy storage process proceeds according to a diffusion-controlled behavior (battery-type electrode). If b value equal to 1, then it is an ideal surface-controlled behavior (supercapacitor system). By fitting the CV data obtained for Fc-MS-40, the results (**Figure 10**b) reveal that b values are very close to 1 for both the cathodic (0.97) and the anodic voltammetric peaks (0.90) over a wide sweep rate range varying from 5 mV s^{-1} to 50 mV s^{-1} and then tended to decrease. This suggests that the energy storage of Fc-MS-40 is an almost exclusive surface-controlled process and that diffusion starts to become a bottleneck only at larger scan rates.

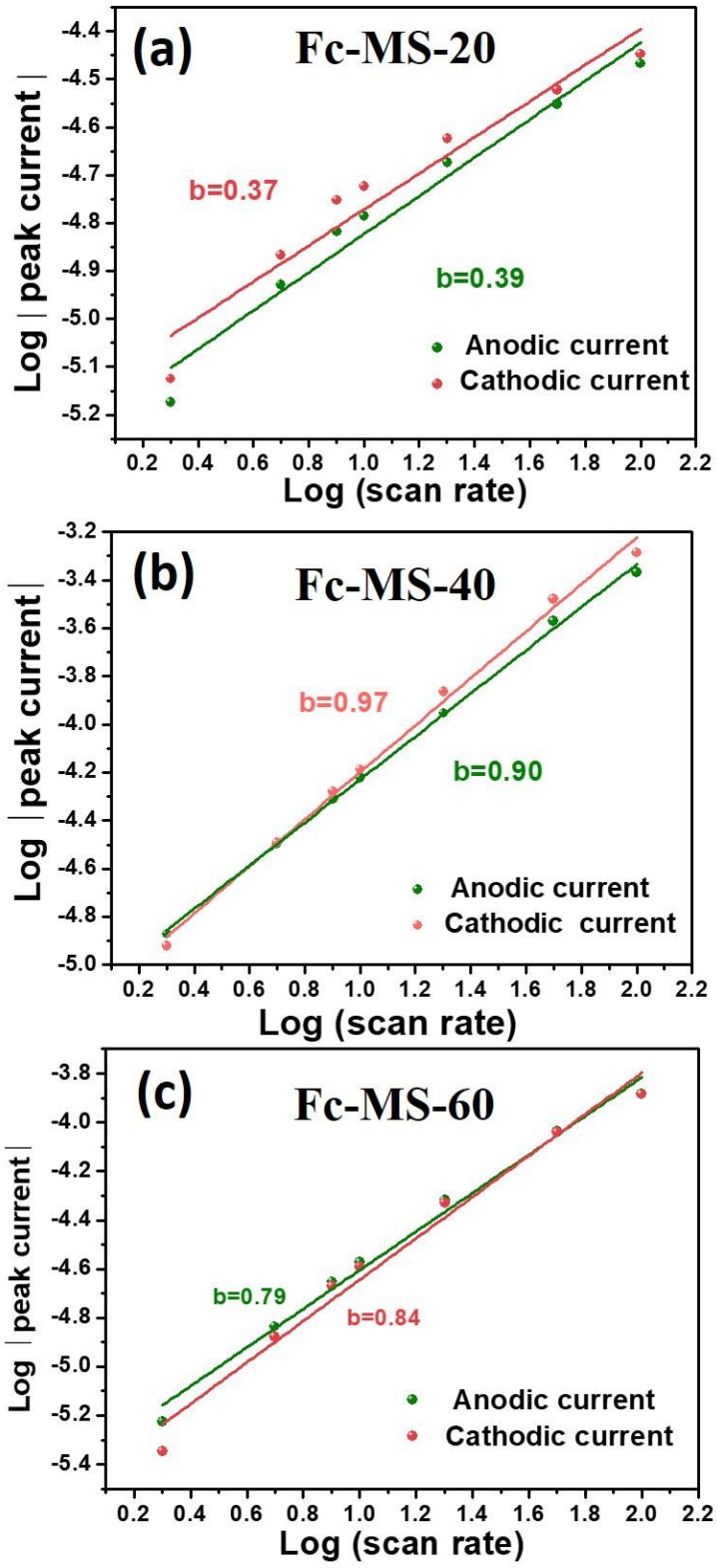

Figure 10. Variation of the anodic and cathodic peak currents recorded by CV as a function of the potential scan rates (log scale) for Fc-MS-20, Fc-MS-40, and Fc-MS-60.

By contrast, b values calculated for Fc-MS-20 (**Figure 10**a) are only around 0.4 (probably due to slow electron diffusion in the hopping process between more distant ferrocene moieties or the large internal resistance), whereas the ferrocene-functionalized film with higher density of redox centers but lacking mesostructural order (i.e., Fc-MS-60), gave rise to b values around 0.8 (**Figure 10**c) indicating an overall charge transfer mechanism mainly governed by surface-controlled redox processes but also limited by the slow diffusion of counter ions. As the result, Fc-MS-40 shows the best rate performance among the three Fc-MS samples even if suffering from some diffusional limitations at higher potential scan rates but much less than Fc-MS-20 and Fc-MS-60 samples (**Figure 11**).

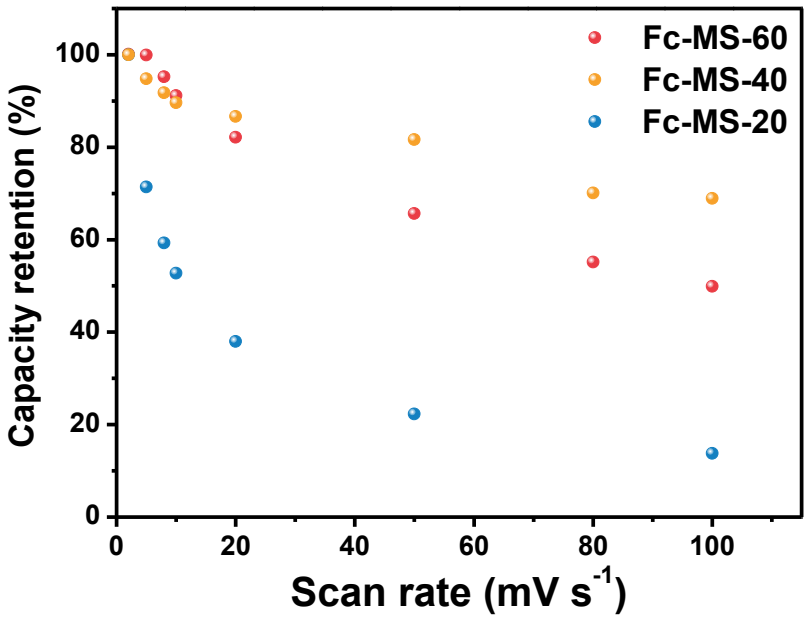

Figure 11. The capacity retention of Fc-MS-20, Fc-Ms-40 and Fc-MS-60 calculated at various potential scan rates (from 2 mV s^{-1} to 100 mV s^{-1}).

Besides, to further quantitatively evaluate the contribution of surface-controlled current at a fixed scan rate, the electrochemical data extracted from CV measurements for Fc-MS-40 can be further fitted with the following equation: $i(V) = k_1 v + k_2 v^{0.5}$; where *i(V)* is the current at a given potential and $k_1 v$ and $k_2 v^{0.5}$ represent the surface-controlled

current and diffusion-controlled current, respectively.[134] The results (**Figure 12**a) demonstrate that the greatest part of the total faradic current comes from a surface-controlled contribution (91.2% at the scan rate of 20 mV s^{-1}), pointing out further that the existence of a high density of the redox species contributes to facilitate the electron hopping process (as reported for other densely packed redox-active systems[112,113]) and the suitable pore structure to reduce the ions diffusion resistance (**Figure 2**a&b). A scheme (**Figure 12**b) has also been prepared to illustrate the electron-hopping process. No electron transfer can occur through the isolating silica walls, but only via electron hopping between adjacent ferrocene moieties (thanks to the flexibility of the alkyl arm linking them to the silica) and concomitant charge neutralization by the electrolyte ions, of course after a first electron transfer between the electrode surface and the ferrocene group located close to this surface. Finally, one can estimate the charge transfer resistance for the electron-hopping process with impedance spectroscopy (see the impedance spectrum in **Figure 12**c). In the impedance spectroscopy, the intersection of x-axis at high frequency region represents the internal resistance of the system, including the resistance of the electrolyte between the working electrode and reference electrode, and the internal resistance of the electrode. The semi-circle in the middle-to-high frequency region stands for the charge transfer resistance during the redox reaction. The long tail in the low-frequency region is due to the resistance of counter ions diffusion during the redox reaction. For the Fc-MS-40, the intercalation point at x-axis is ca. 15 Ω, mainly coming from the resistance of the electrolyte. The diameter of the semi-circle is of ca. 60 Ω, confirming the possible long-range charge transport in a film, however, made of an insulating material. Besides, the almost vertical line in the low-frequency region demonstrates the fast ions diffusion inside the silica thin film, proving the low ions diffusion resistance in the vertically aligned mesochannels.

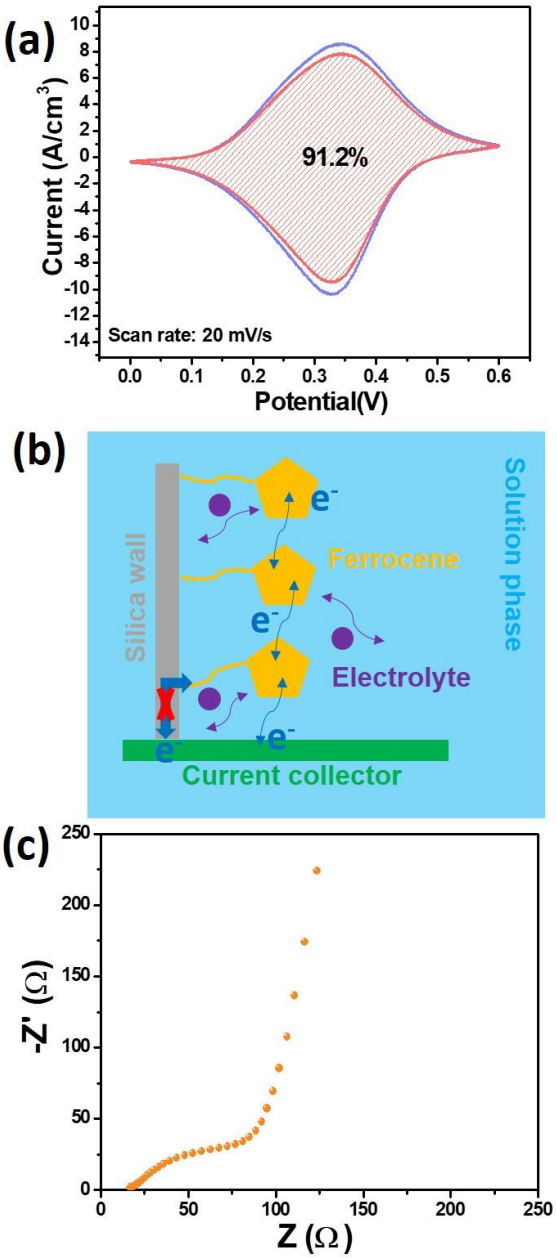

Figure 12. (a) Capacitive contribution of the oxidation process at the scan rate of 20 mV s^{-1} marked by the shaded region. (b) Illustration of the electron-hopping redox process taking place in the ferrocene-functionalized mesoporous silica film (electron hopping between adjacent ferrocene sites and charge neutralization by the electrolyte anions, according to equation 1, whereas no possible electron transport through the insulating silica walls). (c) Impedance data obtained for Fc-MS-40 at open circuit potential in a three electrode system within the frequency range from 100 kHz to 0.1 Hz.

2.3.3 Extension to cobaltocenium-functionalized mesoporous silica thin films

Not only limited to ferrocene, further derivatization of the azide-functionalized mesoporous silica films can be extended to other species with the only requirement of containing an alkyne function in their structure. In this sense, a cobaltocenium-functionalized vertically-aligned silica thin film (Co^+-MS-40) has been prepared by following an analogous procedure to the one previously described in the case of the Fc-MS films. As shown in **Figure 13**a, the CV curves of the Co^+-MS-40 exhibits a pair of well-defined redox peaks at potentials around -1 V, proving that redox reactions of the immobilized cobaltocenium/cobaltocene system can also occur through the electron-hopping process in the mesoporous film. Similar to those of Fc-MS-40, the redox curves are symmetrical even at the scan rate of 500 mV s^{-1}, illustrating the fast charge transfer and associated ion transport processes. The galvanostatic charge-discharge curves of Co^+-MS-40 were also recorded at various current densities from 4 to 20 A cm^{-3} and the obtained results (**Figure 13**b) are indicative of fast surface-controlled redox reactions as no obvious platform can be observed during the charge-discharge processes. However, compared with that of the Fc-MS-40 sample, the coulombic efficiency of Co^+-MS-40 is relatively low, only ~36% at the current density of 4 A cm^{-3}. The reason could be the existence of trace amount of oxygen in solution (even after bubbling with nitrogen) which would chemically oxidize back the cobaltocene (generated during the electrochemical reduction process) into cobaltocenium. Based on the discharge curves, the capacity of Co^+-MS-40 can reach 105 C cm^{-3} at the current density of 4 A cm^{-3} and still be able to retain 68% at the current density of 40 A cm^{-3} (**Figure 13**c).

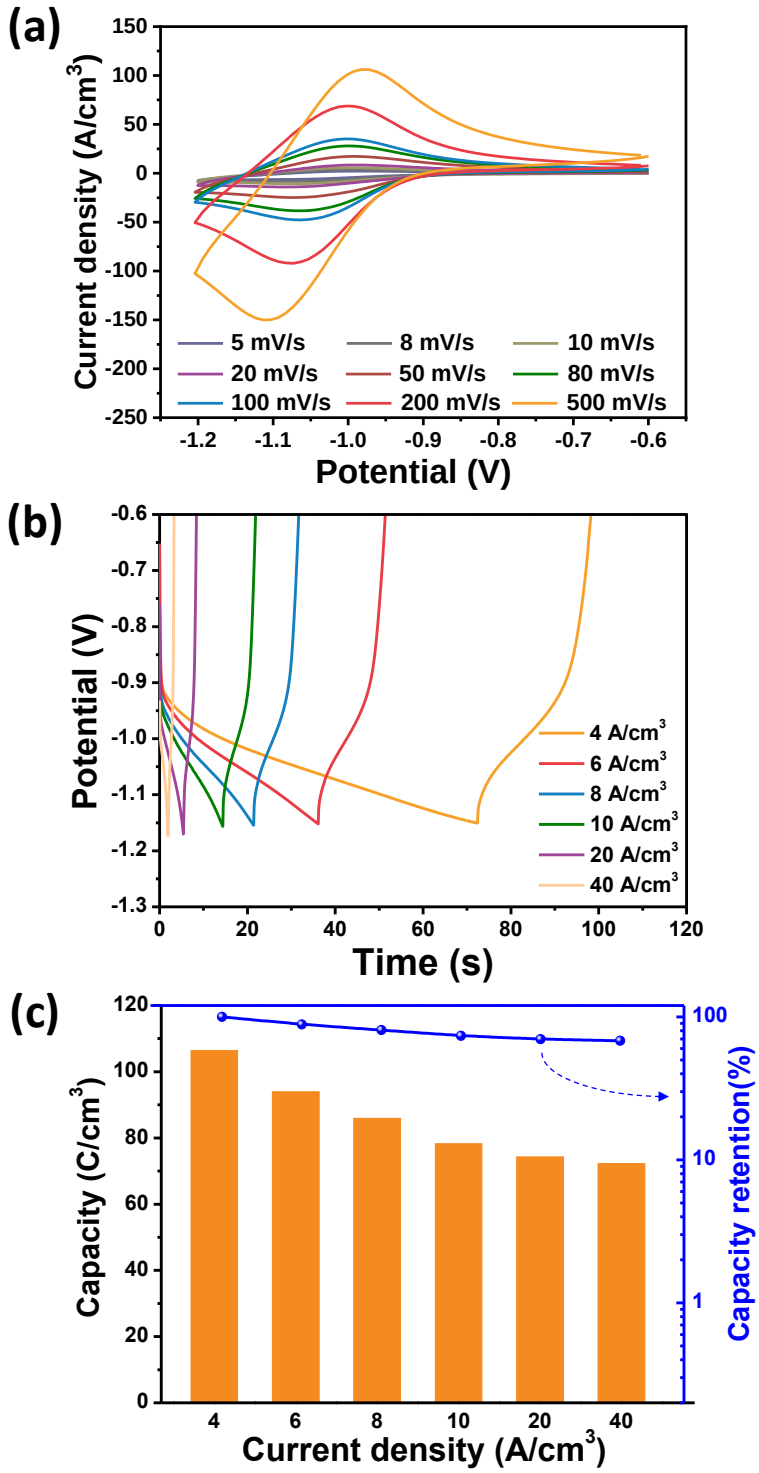

Figure 13. Energy storage performance of the cobaltocenium-functionalized film electrodes. (a) CV curves of the Co^{+}-MS-40 film at scan rates varying from 10 to 500 mV s^{-1}. (b) Charge and discharge plots at various current densities from 0.4 A to 20 A cm^{-3}. (c) Specific capacities vs. current density plots.

2.3.4 The fabrication of the Fc-MS//Co^{+}-MS solid-state energy storage devices

As discussed above, the vertically-aligned silica thin film can be functionalized with either ferrocene or cobaltocenium, achieving the redox reaction in different potential regions. As shown in **Figure 14**a, both of the two electrodes well operate in 1M LiCl and the potential separation between the two redox reactions could reach 1.4 V, a large voltage range considering the theoretical water-splitting voltage of 1.23 V. Therefore, a solid-state device with Fc-MS-40 as the cathode, Co^{+}-MS-40 as the anode, and the LiCl/PVA as the solid-state electrolyte has been assembled to inspect its energy storage performance. As shown in **Figure 14**b, the assembled device exhibits a pair of redox peaks at about 1.4 V during the cyclic voltammetry at a scan rate of 300 mV s^{-1}, in line with the observation in a three electrodes system. However, the redox peaks are ill-shaped with a much bigger anodic peak in comparison to the cathodic counterpart. Moreover, the redox reaction is not stable, and the intensities of the redox current fast fade away with continuous CV cycles. Regarding this certain device, the anodic peak represents the oxidation of ferrocene to ferrocenium while the cobaltocenium is reduced to the cobaltocene, whereas, the formation of the cathodic peak is due to the reduction back the ferrocenium to ferrocene and the oxidation back the cobaltocene to the cobaltocenium. However, the cobaltocene is not environmentally stable and could be reoxidized back to cobaltocenium by the trace amount of oxygen in the electrolyte, instead of the electrochemical pathway, as similar behaviors can be observed in the three-electrode system. As a result, the generated ferrocenium can hardly be reduced back since the chemically consumption of cobaltocene counterpart, which would be the possible reason for the smaller cathodic peak and the fast fading energy storage performance. Consistent with the CV results, the galvanostatic charge-discharge curves at 0.2 mA cm^{-2} (**Figure 14**c) also shows the stored charges cannot properly release and the corresponding columbic efficiency is less than 30%. These features demonstrate the Fc-MS//Co-MS solid-state device cannot meet the energy demand in the practical scenarios.

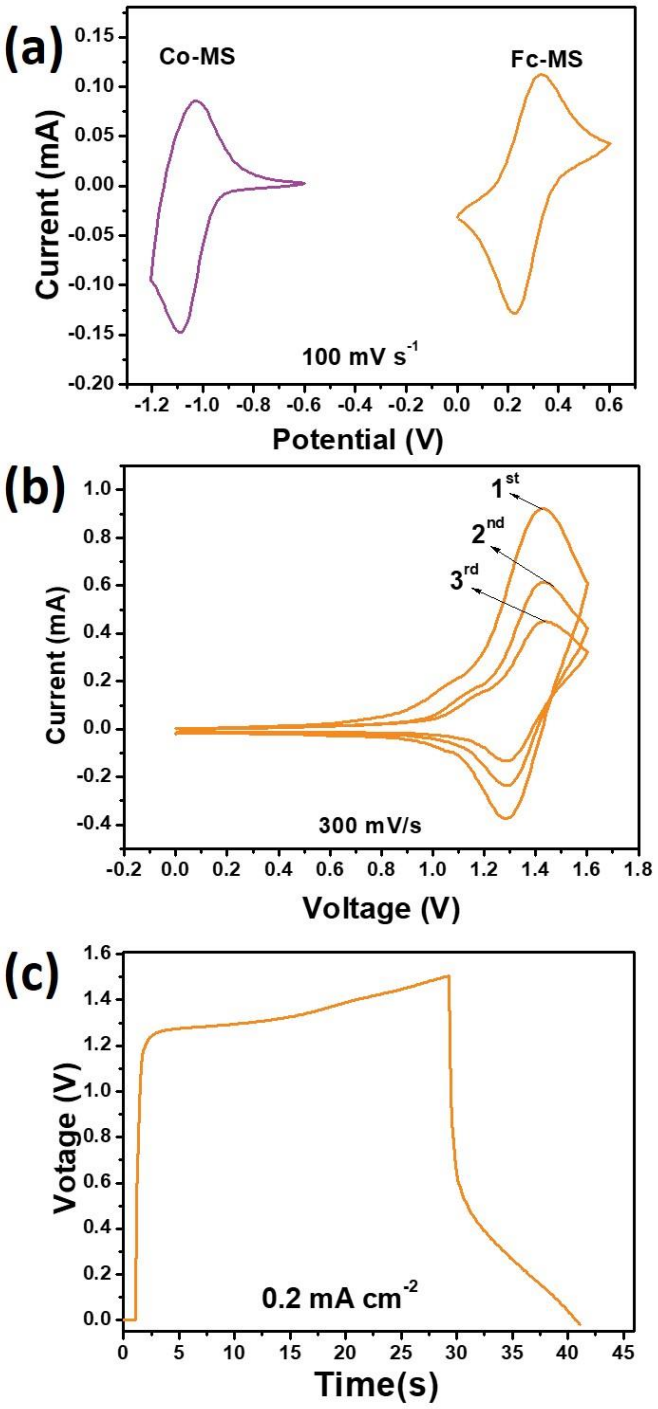

Figure 14. (a) The CV curves of ferrocene/cobaltocenium functionalized silica films at a scan rate of 100 mV s^{-1} in a 3-electrode system with 1M LiCl electrolyte; (b) the continuous three CV cycles of the as-prepared Fc-MS//Co-MS solid state device at a scan rate of 300 mV s^{-1}; (c) the galvanostatic curve of Fc-MS//Co-MS solid state device at a current density of 0.2 mA cm^{-2}.

3.3.5 The fabrication of the Fc-MS//Graphene solid-state energy storage devices

Since the Co^{+}-MS electrode cannot associate to the energy storage requirement, a graphene anode has been further prepared to pair with the Fc-MS electrode. The capacity of graphene electrode can be adjusted by controlling the graphene deposition time, and such electrode can run well in the potential range of 0 V to -0.8 V, complementary to Fc-MS electrode. (**Figure 15**a (the inset is the digital photo of the graphene electrode)) The electro-deposited graphene electrode with capacity equal to that of Fc-MS-40 electrode has been prepared. (see the corresponding CV curves in different potential window with 1 M LiCl electrolyte in **Figure 15**b).

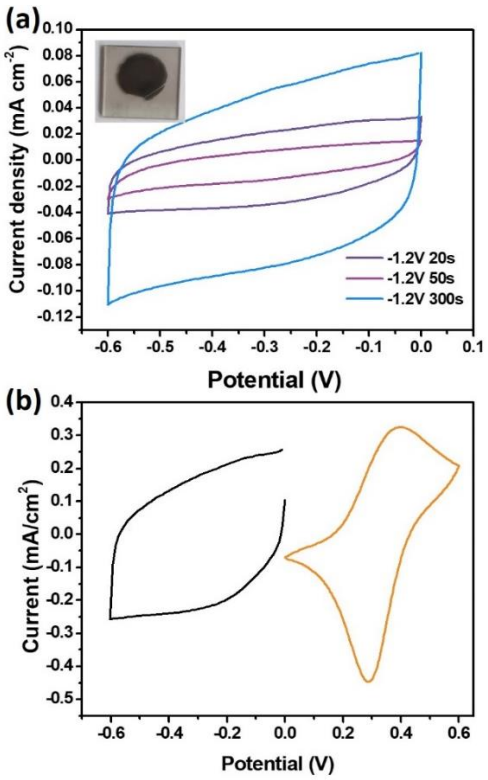

Figure 15. (a) The CV curves of the graphene electrode prepared with the deposition time of 20s, 50s, and 300s (the inset is the digital photo of the graphene electrode); (b) The CV curves corresponding to Fc-MS-40 and electrodeposited graphene electrode recorded at the same potential scan rate of 50 mV/s (but different windows) in 1M LiCl solution.

A new solid-state hybrid-device is further assembled by using the Fc-MS-40 as the anode, polyvinyl alcohol/lithium chloride gel as separator electrolyte, and electrodeposited graphene as the cathode material. The digital photo of the hybrid device is given in the inset of **Figure 15**a. The energy storage characteristics of the as-prepared Fc-MS-40//Graphene hybrid-capacitor device are illustrated in **Figure 15**. As shown, it is able to work over the potential window from 0V to 1.2V at various scan rates ranging from 20 mV s^{-1} to 1000 mV s^{-1} (**Figure 15**a). Despite the hybrid nature of the asymmetrical device, a pair of broad voltammetric signals corresponding to the redox processes related to ferrocene can be still observed in this potential window. The CV curves are well defined and symmetrical even at the scan rate of 1000 mV s^{-1}, indicating the good rate performance. The charge-discharge curves (**Figure 15**b) exhibit, in contrast to battery, a distorted triangle charge-discharge shape with gentle slope but without obvious plateau, also revealing the pseudo-supercapacitor nature of the Fc-MS-40//Graphene device. Besides, the charge-discharge curves are highly symmetrical at different current densities, indicating a high coulombic efficiency and most stored charges can be released during the discharge process. The cycling stability of the device, as also determined by the CV method (see the corresponding results in **Figure 15**c) is quite robust as 74% capacity retention is maintained after 500 successive cycles.

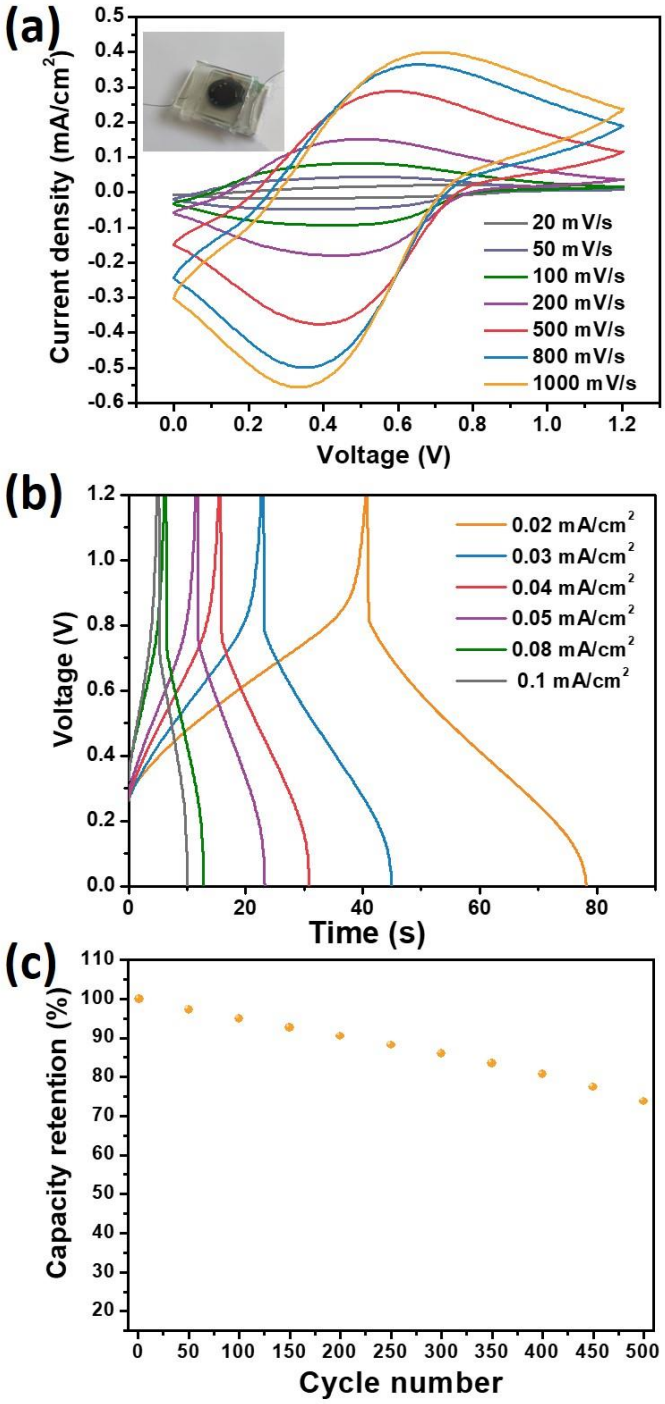

Figure 15. Energy storage performance of the asymmetrical solid-state device (Fc-MS-40 as the anode, graphene as the cathode and the PVA/LiCl as the electrolyte). (a) CV curves at various scan rates from 20 to 1000 mV s^{-1}. (b) Charge/discharge curves at various current densities from 0.02 mA cm^{-2} to 0.1 mA cm^{-2}; (c) Cycling performance as evaluated by CV at a potential scan rate of 200 mV s^{-1}.

Based on the obtained CV curves, the specific capacities can be calculated by integrating the area bounded by the closed curves at all scan rates. (Note that the total areas are calculated on the basis of the two electrodes). As shown in **Figure 16**a, this device can deliver 0.74 mC cm^{-2} at the scan rate of 20 mV s^{-1}, and it can still maintain 57% at a scan rate of 500 mV s^{-1} (2.4 s for the charging/discharging time) and even 45% at a scan rate of 1000 mV s^{-1} (only 1.2 s for the charging/discharging time). This outstanding performance demonstrates that the redox reaction rate of the assembled redox molecules system through the electron-hopping process is fast and comparable to its double-layer type graphene counter electrode. The Ragone plots (**Figure 16**b) further reveal that a high energy density of 0.13 μWh cm^{-2} can be achieved at a power density of 12.8 μW cm^{-2}, a value still remaining as high as 0.07 μWh cm^{-2} at higher power density (180 μW cm^{-2}), which is better than the reported similar thin film energy storage devices.

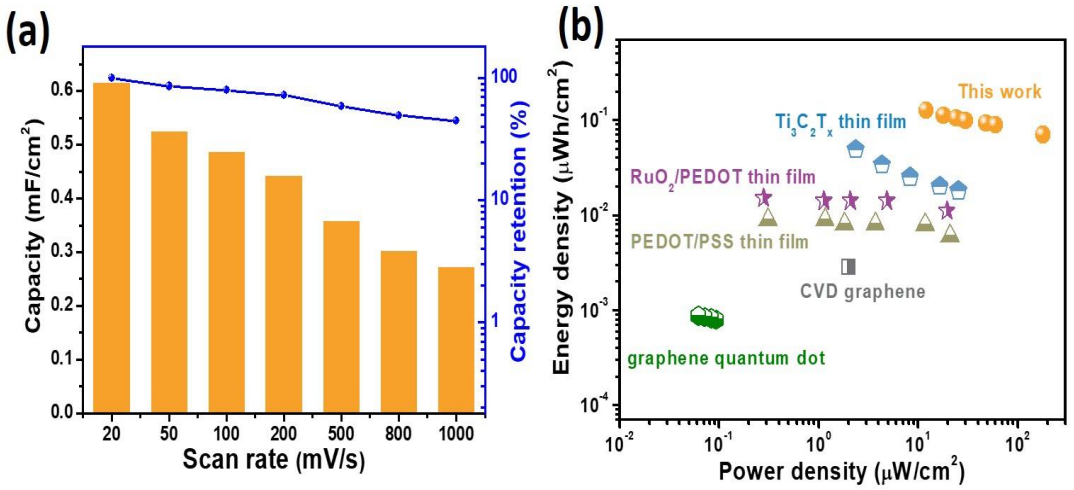

Figure 16. (a) The capacities of the Fc-MS//graphene devices on the basis of CV curves at various scan rates; (b) the Ragone plot of this device Ragone plots of this device and PEDOT/PSS,[127] RuO_2/PEDOT,[128] $Ti_3C_2T_x$,[135] Graphene quantum dot,[136] CVD graphene.[137]

3.4 Conclusions

Vertically-aligned mesoporous silica thin films anchoring redox-active species on their internal surface have been generated onto ITO electrodes and investigated as a novel family of energy storage materials. Charge propagation through such insulating coatings occurred via an electron-hopping process between the adjacent redox centers spatially isolated from each other by covalent bonding to the mesopore walls. Two processes governed their behavior as energy storage material, the charge transfer itself via electron hopping and the diffusion of counter ions to maintain the electroneutrality, both of them possibly restricting the rate of redox reactions. From experiments made on boundary cases (in terms of density of redox centers and degree of mesostructural order), it appears that the best performance of such electron-hopping based energy storage materials can be achieved by increasing the density of active sites (to improve the charge transfer rate) and the construction of widely-open and regular channels (in order to reduce the resistance to mass transport necessary to maintain charge balance). On that basis, the Fc-MS-40 thin film fulfilling well these two requirements can deliver a capacity of 105 C cm^{-3} (1.1 mC cm^{-2}) at a current density of 0.4 A cm^{-3}, and retain 48% of its capacity at a short charging time of 2.8 s. A solid-state battery-capacitor hybrid device was also prepared by using graphene as counter-electrode, and it can deliver an energy density of 0.07 μWh cm^{-2} at the high power density of 180 μW cm^{-2}. Moreover, such transparent nanoporous silica membranes can be manufactured with other ethynyl-containing redox molecules (e.g., ethynylcobaltocenium), which broadens their possible application scenarios in the field of electrochemical energy storage.

Chapter III

Construction of the Ferrocene Functionalized Mesoporous Silica Film on Graphene/Graphite 3D Architectures with Enhanced Energy and Power Densities

3.1 Introduction

The energy storage behavior of the ferrocene-functionalized vertically-aligned mesoporous silica thin film generated on the surface of ITO has been systematically demonstrated in the last chapter, showing competitive energy density and power density in comparison to the similar thin film systems. However, this nano-level silica film can be hardly extended to micro/millimeter level by simply prolonging the deposition time or enlarging the applied biased-potential, as the single-layer film growth could meet a threshold somehow when the thickness reaches ca. 400 nm, beyond which numerous silica beads with randomly oriented worm-like mesochannels will be generated on the top of the film[92,138]. As a result, the expansibility of the electron-hopping governed silica thin film system has been restrained to meet the practical energy storage demands due to the lack of assembled active sites. Therefore, developing a feasible approach to integrate more active centers has become a pressing need for achieving the breakthrough of such electron-hopping system.

Compared to the classical sol-gel deposition methods (i.e., based on evaporation[139]), one definite advantage of the electrochemically induced film formation (EASA) is its ability to generate uniform silica coatings on surfaces with very complex morphology, such as macroporous electrodes,[140] metal microfibers[141] or graphene nanosheets[142] , for instance. By passing the way of extending thickness, this versatile property offers the possibility to increase the density of redox-active sites via directly generating such silica film on a large surface-area substrate. Graphene, a type of two-

dimensional carbon material featuring extremely large theoretical surface area (2630 $m^2 g^{-1}$) and electrical conductivity ($\approx 10^4$ S cm^{-1}), is widely used as electrode for double-layer capacitors. It can be also functionalized to boost its capacitance,[143,144] but its modification via covalent bonding remains to date restricted to oxidation, monolayer functionalization or the formation of hybrid composites with polymers or inorganic phases.[145,146] Therefore, the construction of the sandwich structure by growing the vertically aligned mesoporous silica film on the surface of mono/few layers graphene could be a wise choice, where the interlayer graphene not only provides large enough surface to accommodate much more silica film but also plays the role to conduct the electrons inside the composite. Besides, the configuration of the composite structure is also pivotal to fully release its energy storage potential, such as optimizing the pores structure to reduce ions diffusion resistance, constructing the internal conductivity network to smooth the electron transfer, and providing the suitable interface properties to stabilize the hybrid framework.

Here, a ferrocene functionalized mesoporous silica film was generated by the EASA method and subsequent click coupling on the surface of an electro-exfoliated graphene foam, where few-layers graphene sheets distributed on the graphite surface provide large area to grow the organic-inorganic hybrid silicate film, the three-dimensionally porous graphite skeletons offer fast internal migration channels for both electrons and counter ions, and the abundant oxygen containing groups of graphene further enhance the stability of the silica film onside. Compared with the two-dimensional ITO substrate that we proposed in last chapter, such graphene-graphite electrode is capable of bearing much high density of fixed ferrocene molecules and could achieve breakthrough in view of capacity density. Several physic-chemical characterizations, including scanning electron microscopy (SEM), X-ray photoelectron spectroscopy (XPS), Raman spectra, etc., have been used to monitor the structural evolution, and also to decouple the structure-performance relationship of such novel hybrid pseudocapacitive material. In

the end, its energy storage behavior has further been evaluated in an asymmetric hybrid device, which shows orders higher energy and power densities than its ITO counterpart.

3.2 Experimental section

Preparation of the electro-exfoliated graphene/graphite electrode:

The electro-exfoliated graphene foam on graphite electrode was prepared according to a slightly modified procedure as those described in the literature[147,148]. The electro-exfoliation process was performed in 0.1 M Na_2SO_4 aqueous solution with a two electrode system, where a piece of graphite foil (0.5 cm × 1 cm) and platinum mesh (2.5 cm × 2.5 cm) were used as the working and counter electrode, respectively. The exfoliation was achieved by applying a voltage of 5 V to the graphite foil for 10 minutes, and the distance between the two electrodes was 5 cm. The exfoliated graphite electrode, labeled as EG, was then thoroughly washed with deionized water and dried at room temperature overnight. Besides, different exfoliation times of 1 min, 5 min, 15 min were also applied to further investigate the structural evolution, and the corresponding products were labeled as EG-1 min, EG-5 min, and EG-15 min, respectively.

Preparation of the electro-exfoliated graphene/graphite coated with ferrocene functionalized mesoporous silica films (EG@Fc-MS):

The mesoporous functionalized silica films were grown on EG electrode via a potentiostatic mode by applying a cathodic potential of -1.5 V (vs. Ag wire pseudo-reference) on the electrodes immersed in silane sol (described in the experimental section) for 10 s. The modified electrode was rapidly removed from the solution and rinsed with water and then dried at 130°C for 2 h. The azide functionalized mesoporous silica film on exfoliated graphite/graphene electrode was denoted EG@Az-MS. Prior to the derivatization with ferrocene, the EG@Az-MS electrode was dipped into an ethanol solution containing 0.1 M HCl, for 30 min, in order to remove the surfactant template (this material was labelled as “CTAB-removal EG@Az-MS”). The CTAB-removal EG@Az-MS were further performed to the click reaction through the typical

click procedure (described in last chapter) to introduce the ferrocene molecules on the surface of silica film, labelled as EG@Fc-MS.

3.3 Results and discussions

3.3.1 Main characteristics of the EG@Fc-MS

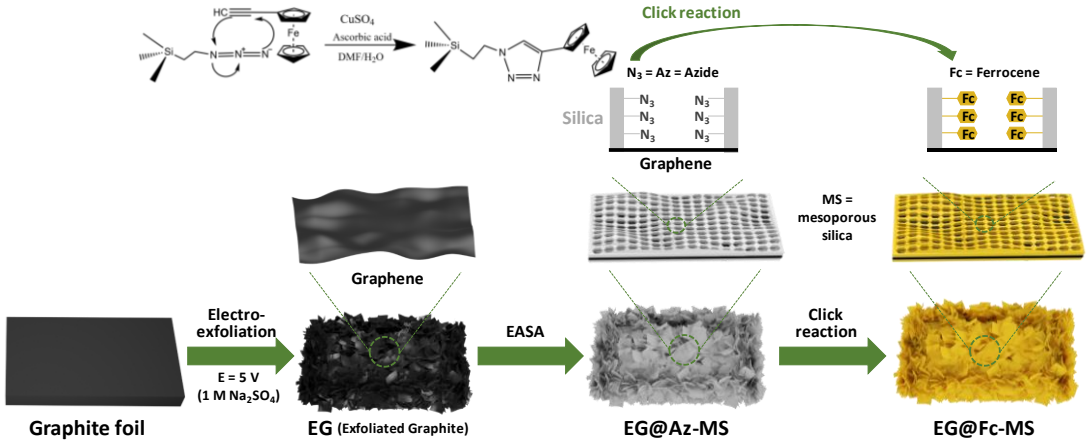

Figure 1. Schematic illustration of the formation of EG@Fc-MS. It involves the formation of exfoliated graphite (EG), its modification with an azide-functionalized mesoporous silica (Az-MS) and a final derivatization by click chemistry to form the ferrocene-grafted mesoporous silica (Fc-MS).

The overall synthesis procedure to get the ferrocene grafted mesoporous silica film on exfoliated graphite/graphene electrode (EG@Fc-MS) is schematically illustrated in **Figure 1**. First of all, an efficient electro-exfoliation method is adopted to open the channels of the low-cost graphite foil and to form a layer of graphene on its surface. Compared with the time/energy-consuming or environment-unfriendly chemical or physical graphene preparation processes, this method only takes a few minutes without harmful by-products throughout the whole process[147,148]. Subsequently, the EASA method[94] is used to generate the mesoporous silica deposits containing azide groups on the electrode surface, which is expected to form a hierarchically porous silica/graphene sandwich structure[142]. Finally, ethynylferrocene molecules acting as

the redox active sites are covalently anchored on the surface of the silica wall, at the highest density compatible with fast charge transfer processes (as optimized for flat electrodes[1,149]) with the help of Cu(I)-catalyzed azide-alkyne cycloaddition (CuAAC) click reaction[94,116].

The morphology evolution during the preparation is analyzed by scanning electron microscopy (SEM). It can be seen from **Figure 2**a, that the structure of pristine graphite foil is compact without obvious channels. However, after electro-exfoliation (**Figure 2**b&c), the interlayer of graphite has been expanded, and macrochannels are formed due to the swell effects of inserted SO_4^{2-} ions and in-situ generated O_2 and SO_2 gases during the electrochemical process[150]. The high-resolution SEM micrograph further reveals that the surface of the EG skeleton is coated by numerous ultrathin nano-sheets with most of the thickness distributed at 9±6 nm, proving the formation of few-layers graphene (**Fig. 2**c&d).

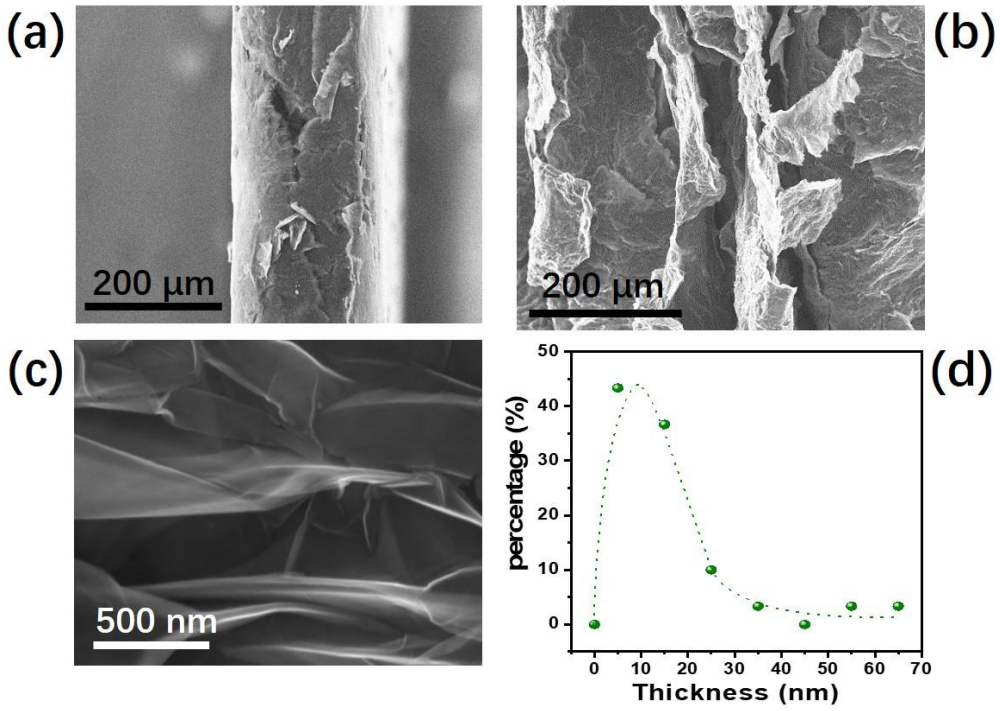

Figure 2. The SEM images of (a) original graphite, (b&c) electro-exfoliated graphite, and (d) the thickness distribution profile of the graphene sheets coated on the surface of the electro-exfoliated graphite electrode.

The exfoliation time plays an important role on the EG morphology, which can have some effects on the energy storage behavior. As shown in **Figure 3**a, the graphite foil becomes thicker and the channels gradually expand to 780 μm as the exfoliation time reaches 10 minutes. However, the thickness of the porous layer significantly declines (to 220 μm) when further extending the exfoliation time (to 15 min), since the shedding of graphene flakes into the solution becomes dominating. As the consequence, the highest current response is also observed for the 10 minutes exfoliated sample on the basis of cyclic voltammetry tests (**Figure 3**b).

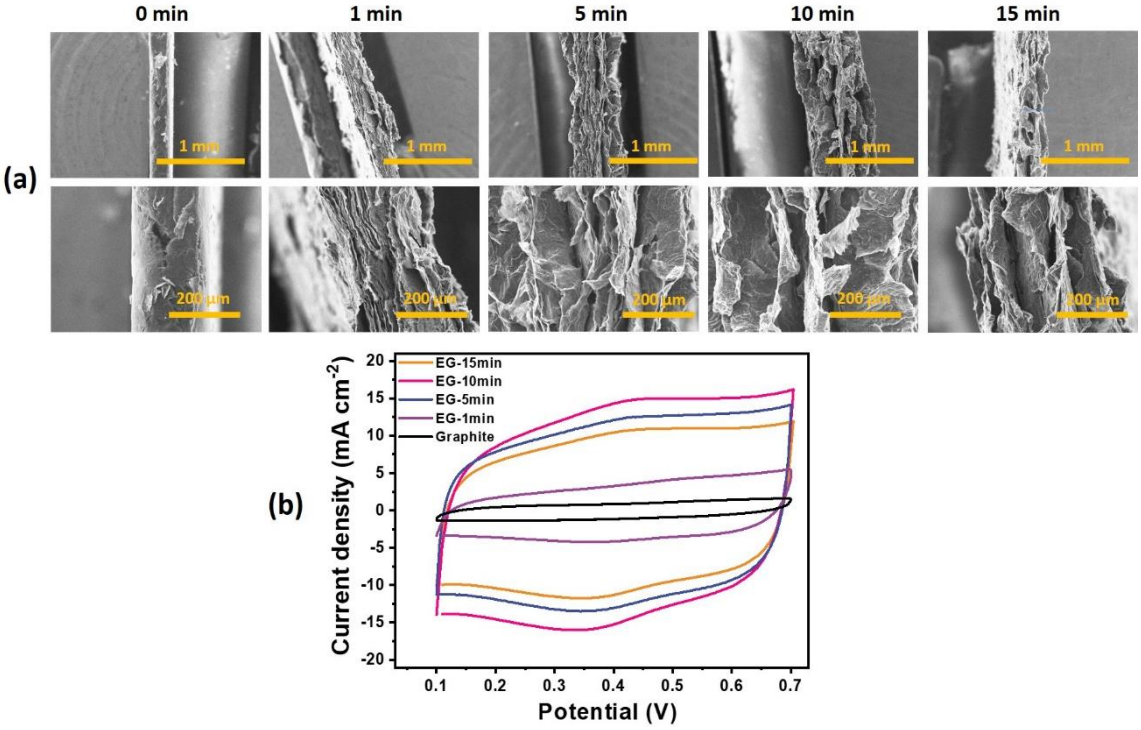

Figure 3. (a) The morphology evolution of graphite during the exfoliation process as a function of time; (b) the corresponding CV curves at a scan rate of 100 mV s^{-1} in 1M H_2SO_4 electrolyte.

After coating with a thin layer of ferrocene functionalized silica film, the morphology of EG@Fc-MS doesn't change too much, but the serious charge accumulation and some cracks on its surface indicate there is an insulating silica layer onside. (**Figure 4**a&b) Besides, compared with that of EG, the sheet thickness of EG@Fc-MS increases to about 75±15 nm (**Figure 4**c), which means that the thickness of the silica layer coated

onside is ca. 65-70 nm. The EDS mapping results of EG@Fc-MS also show uniform distribution of the C, Si, Fe elements (**Figure 4**d), further confirming the rather homogenous coating of ferrocene functionalized silica layer on its surface.

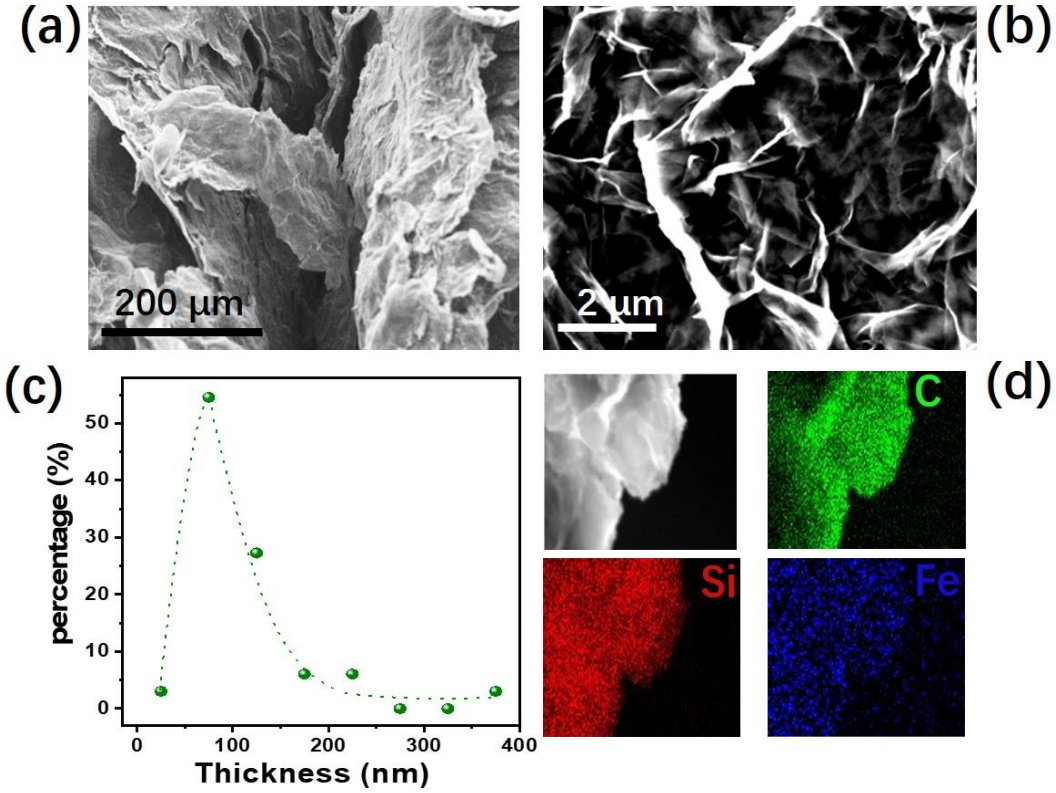

Figure 4. (a-b) The morphology of EG@Fc-MS; (c) The thickness distribution profile of the graphene sheets coated on EG@Fc-MS; (d) The EDX mapping of EG@Fc-MS showing the distribution of C, Si, and Fe.

To identify the structural and compositional evolution of the graphite electrode upon the various modification steps (leading to the materials EG, EG@Az-MS and EG@ Fc-MS), a series of Raman spectra is presented in **Figure 5**. The strong G band (~1580 cm^{-1}), 2D band (~2760 cm^{-1}) and negligible D band (~1360 cm^{-1}) visible for the original graphite foil (see curve (a) in **Figure 5**a) indicate that it is highly graphitized with few defects[151]. By contrast, an obvious D band and a small 2G (~2920 cm^{-1}) band, corresponding to the defect signals from the edge sites of graphene, in addition to the remaining G and 2D bands of graphite can be detected for EG (see curve (b) in **Figure**

5a). This proves that graphene is successfully obtained through the electro-exfoliation method[148][152]. After deposition of azide functionalized silica, no significant changes except that several new peaks (marked with green stars on the images, see curves (c) in **Figure 5**a&b) can be observed for EG@Az-MS, which can be ascribed to the long alkyl chain of CTAB surfactant[153,154]. Unfortunately, the typical Raman signature for azidopropyl-grafted silica materials appearing in the 1250-1500 cm^{-1} region[156] cannot be noticed here because it is obscured by the intense D band of graphene. Nevertheless, a broad band from ~375 cm^{-1} to ~570 cm^{-1} and another one located at ~2110 cm^{-1} can be attributed to the Si–O–Si vibrational mode[154] and the antisymmetric stretching mode of azide group[157,158], respectively (see curve (c) in **Figure 5**b), which verifies the azide functionalized silica film has been formed on the surface of graphene. After CTAB extraction and click coupling with ethynylferrocene, the signals from CTAB and azide disappear for EG@Fc-MS (see curves (d) in **Figure 5**a&b), indicating the surfactant is removed and most azide groups take part in the click reaction. [159]

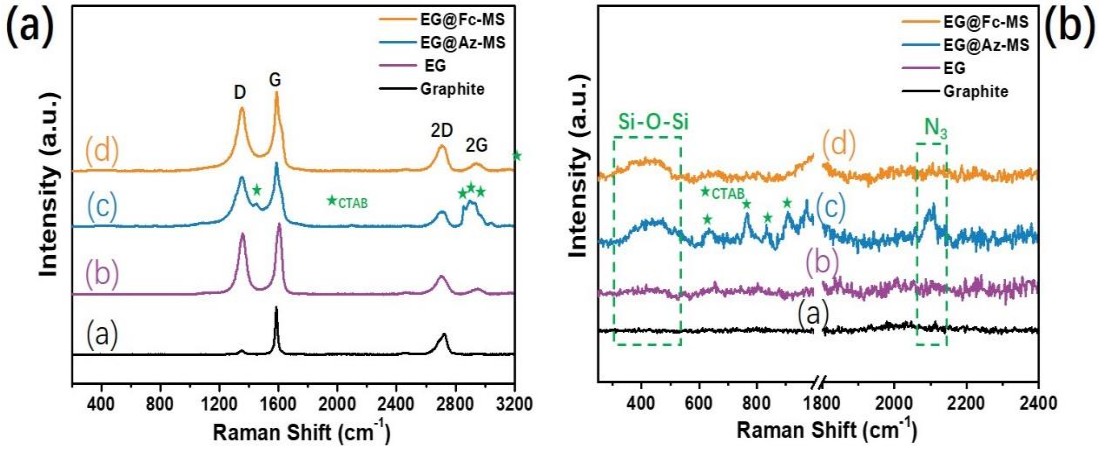

Figure 5. (a-b) The morphology of EG@Fc-MS; (c) The thickness distribution profile of the graphene sheets coated on EG@Fc-MS; (d) The EDX mapping of EG@Fc-MS showing the distribution of C, Si, and Fe.

XPS is further used to complete the materials characterization and to monitor semi-quantitatively the click reaction. The survey scan spectra of graphite foil, EG, EG@Az-

MS and EG@Fc-MS are given in **Figure 6**a, and the detailed element ratio is given in **Table 1**. It can be seen clearly that an increment of the oxygen contents occurs, from 5.0% in graphite to 14.8% in EG, indicating the partial surface oxidation of graphite during the electro-exfoliation process. Besides, the signals from silicon, nitrogen, and iron can be detected in sequence after the silica deposition and click reaction. As shown in the high resolution C_{1s} spectra (**Figure 6**b), a band for C-O at ~287 eV and another for C(O)-O at ~288.7 eV can be detected for EG (in addition to the expected C-C and C=C signals of graphene), which constitutes an evidence for the existence of hydroxyl and carboxyl groups on the carbon surface[147]. The existence of oxygen-containing groups on the surface may facilitate the anchoring and stabilize the silica layer being deposited subsequently[155,160]. One can also see some contribution of C-N (C_{1s} signal at ~286.6 eV) after deposition of the silica film (EG@Az-MS sample), which comes from the CTAB surfactant and disappears while a new one grows at ~286.2 eV for EG@Fc-MS, indicating the effective removal of the template and the formation of 1, 2, 3-triazole group, respectively. This is seen more clearly on the high-resolution N_{1s} spectra (**Figure 6**c). For EG@Az-MS, four contributions can be recognized: the neutral and negative nitrogen species from azide groups (401.0 eV), the positively charged nitrogen species from CTAB (402.9 eV) and azide groups (404.5 eV), as well as some residual nitrate ions originating from the electrodeposition electrolyte (406.8 eV), which are consistent with literature data for the azidopropyl moieties[161,162], the quaternary ammonium centers of CTAB[163] and nitrate[164]. After being washed with HCl/EtOH solution, both signals from CTAB and nitrate disappears, and after click reaction with ethynylferrocene, the characteristic signals from the azide groups (at 401.0 eV and 404.5 eV, with 2:1 ratio[165]) vanishes and a new broadened peak emerges (with chemically distinct nitrogen contributions located at 400.2 eV and 401.3 eV), which corresponds to the 1,2,3-triazole groups[166]. A semi-quantitative estimation of the proportion of azido groups involved in the click reaction can be roughly obtained from comparing the ratio of azido peak at ~404.5 eV for both EG@Fc-MS (**Figure 6**c) and EG@Az-MS after CTAB removal (**Figure 6**d), giving rise to a

yield of 82%. The presence of ferrocene on the EG@Fc-MS electrode is evidenced by the Fe_{2p} signal (**Figure 6**a). Finally, trace amounts of N (0.6%) and S (1.5%) can be also observed for EG (i.e., prior to film formation), possibly due to some impurities in the graphite foil (**Table 1**).

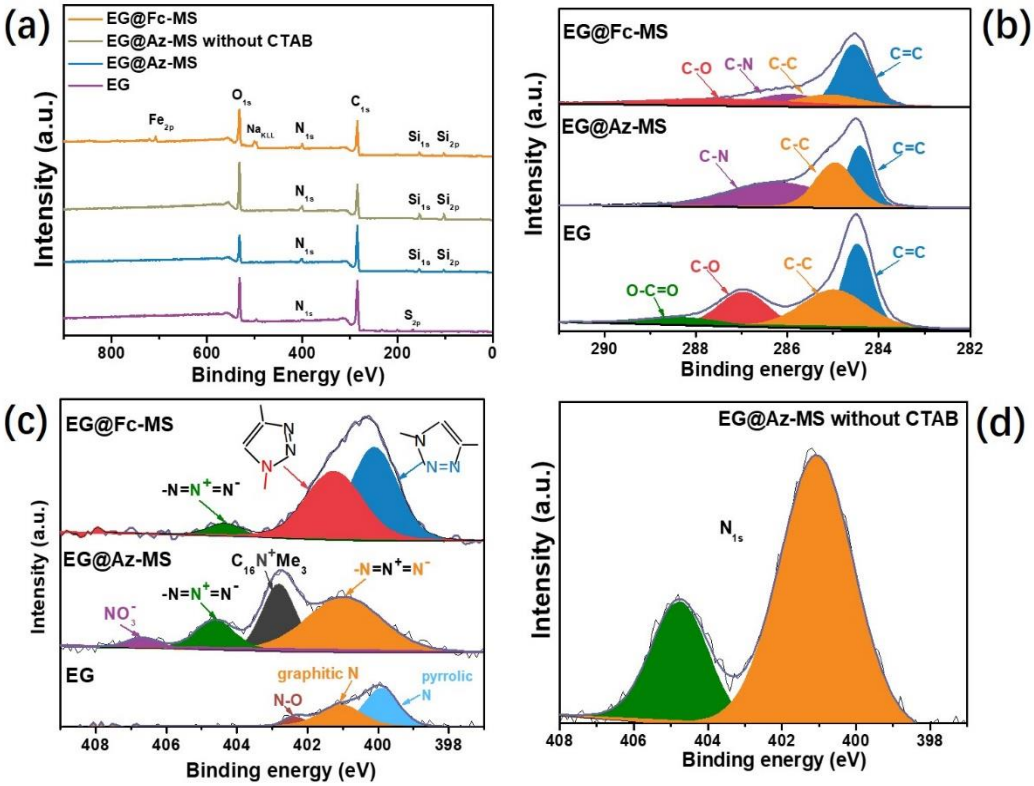

Figure 6. (a) XPS survey scan spectra of EG, EG@Az-MS (before and after CTAB removal) and EG@Fc-MS; (b) High resolution C1s spectrum of EG, EG@Az-MS, and EG@Fc-MS; (c) High resolution N1s spectrum of EG, EG@Az-MS, and EG@Fc-MS; (d) The high resolution N1s spectrum of EG@Az-MS (after CTAB removal).

Table 1. Elemental ratios obtained from XPS for graphite, EG, EG@Az-MS (before and after removal of the surfactant template) and EG@Fc-MS samples.

	O	**C**	**N**	**Na**	**S**	**Si**	**Fe**
Graphite	5.0	93.8	-	-	1.1	-	-
EG	14.8	82.3	0.6	0.2	1.5	-	-
EG@Az-MS (prior CTAB removal)	11.5	79.2	3.2	-	0.6	5.1	-
EG@Az-MS (after CTAB removal)	20.5	64.3	3.7	-	-	11.7	-
EG@Fc-MS	18.0	68.3	3.1	2.5	-	7.7	0.4

Nitrogen adsorption-desorption isotherms for EG, EG@Az-MS and EG@Fc-MS materials are given in **Figure 7**a. Typical IV isotherms with H_3 or H_4 hysteresis loop can be observed for the three samples, which means the existence of mesopores formed by the assembly of plate-like particles[167]. At the relatively high pressure (P/P_0>0.85), a steep increase of nitrogen adsorption amount occurs for the three samples, a sign of the existence of macropores resulting from agglomerates of graphene sheet[168], consistent with the morphology observation (**Figure 2**c&**4**b). The corresponding pore distributions calculated from the Barret–Joyner–Halenda (BJH) model with adsorption branches are given in **Figure 7**b. There is not too much difference for pore structure of EG and EG@Az-MS, but a new type of pores located at ~3 nm appears for EG@Fc-MS due to the removal of CTAB template, which proves the silica layer coated on the surface of graphene is highly mesoporous.

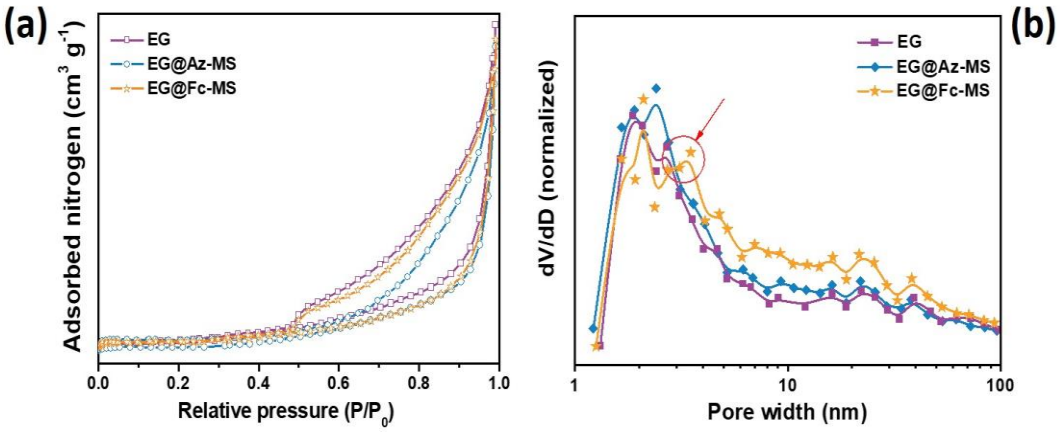

Figure 7. (a) Nitrogen adsorption-desorption isotherms and (b) Pore distribution curves for EG, EG@Az-MS, and EG@Fc-MS.

3.3.2 Energy storage performance of graphite, EG, and EG@Fc-MS

The energy storage performance of graphite foil, EG and EG@Fc-MS are firstly compared from cyclic voltammetry experiments in 1 M H_2SO_4 aqueous electrolyte with a three-electrode setup. The CV curves of original graphite foil, EG, and EG@Fc-MS, as recorded at a scan rate of 50 mV s^{-1}, are shown in **Figure 8**a. The original graphite foil shows a negligible current response due to its compact structure and low surface area. In contrast, the EG delivers much higher current with an obvious rectangular shape, a sign of the electrical double layer capacitance, demonstrating the significantly increased active area from its porous structure and the wide effective surface area due to the presence of large amount of graphene sheets. After introducing the ferrocene functionalized silica film, a pair of well-defined redox peaks originating from the reversible redox reaction of ferrocene molecules can be observed for EG@Fc-MS. Besides, the double-layer capacitance of this EG@Fc-MS electrode remains similar to that of EG in the non-faradic potential region from 0.1 V to 0.2 V, demonstrating that the existence of mesoporous silica thin film on its surface does not cause obvious resistance for electrolyte transport through the silica-on-graphene layer. This is indeed important, also for the faradic process, as the mechanism of electron self-exchange reactions between adjacent ferrocene moieties operating here (an electron-hopping

process well accepted for electroactive polymers consisting of fixed molecular redox sites[169] or surface-tethered redox molecules with flexible linkers[170], which is also valid for organic polymers with pendant ferrocenes[171]), involves charge neutralization by the electrolyte ions from the solution (Eq. 1).

$$Fc - 1\,e^- + X^-(sol) \Leftrightarrow Fc^+,X^-(film) \quad (1)$$

(with Fc = ferrocene; Fc^+ = ferricinium; X^- = counter-anion; sol = solution)

The highly porous structure of EG@Fc-MS thus contributes to facilitate the transport of such ions necessary to maintain charge balance, which is a key parameter in pseudo-capacitive energy storage always looking at improved ion accessibility to redox-active sites[61]. The CV curves of EG@Fc-MS recorded at various scan rates ranging from 20 mV s^{-1} to 200 mV s^{-1} (**Figure 8**b) reveals symmetrical redox current responses with rather small cathodic-to-anodic peak potential separation (yet increasing with potential scan rates, see **Figure 8**c). This confirms the efficient charge transfer and the electrolyte transport processes of the electron-hopping system. Unlike polyferrocenylsilanes, which generally exhibit two oxidation signals at distinct potentials[172], only a single couple of anodic and cathodic peaks is observed here, indicating no electronic interaction between ferrocene centers in the nanochannels. Compared to soluble redox mediators (also used in electrochemical capacitors[173]), the present system is made of supported mediator species covalently bonded to the electrode material, offering easier processability for accommodation in a device (i.e. no need for additional membrane, for instance).

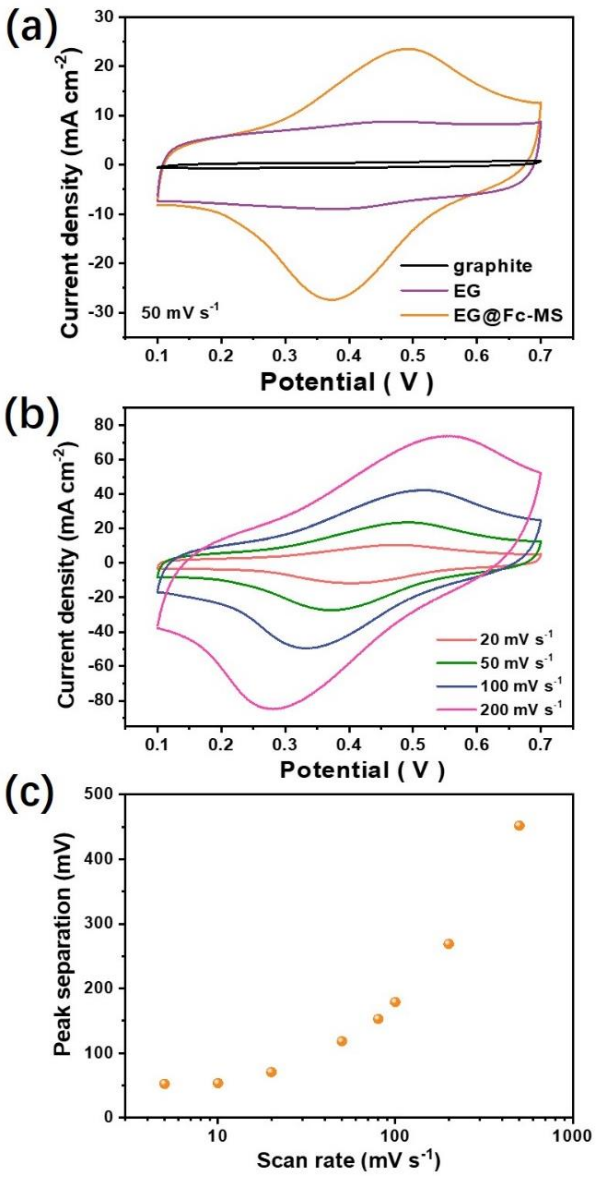

Figure 8. CV curves recorded for the three electrodes system at a scan rate of 50 mV s^{-1} (a); CV curves recorded for EG@Fc-MS at various potential scan rates, from 20 mV s^{-1} to 200 mV s^{-1} (b); The peak separation of EG@Fc-MS at various scan rates (c).

To further evaluate the energy storage behavior and its capacity, the charge-discharge curves of EG@Fc-MS at various current densities from 2 mA cm^{-2} to 100 mA cm^{-2} are displayed in **Figure 9**a. Different from the triangular charge-discharge curve of double-layer capacitance, the curves are distorted but without obvious charge-discharge plateau. This phenomenon illustrates that the redox reaction of ferrocene molecules is not an ion diffusion-controlled process but a surface-controlled one[3]. Furthermore, the nearly

symmetric curves also verify the highly reversible redox reaction and the coulombic efficiencies at different current densities are all above 95% (**Figure 9**b).

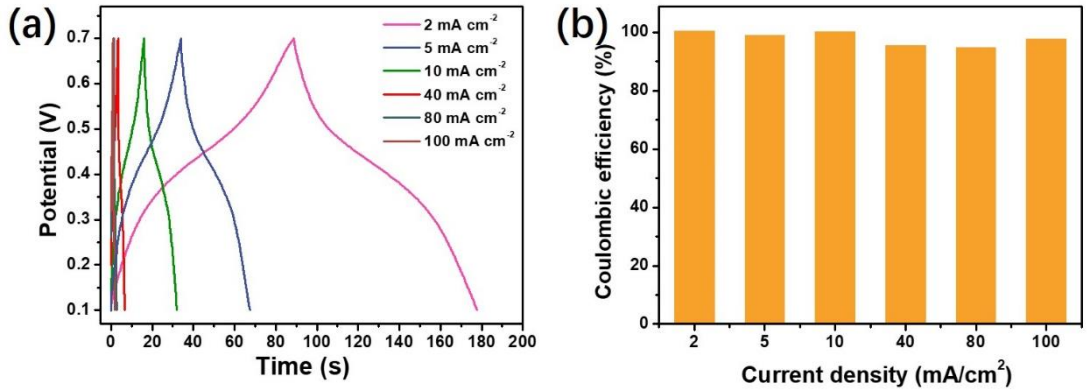

Figure 9. (a) Charge-discharge curves of EG@Fc-MS; (b) The corresponding coulombic efficiency.

Similarly, the charge-discharge curves of EG are also given in **Figure 10**a, also delivering a high coulombic efficiency——above 98% (**Figure 10**b). Based on these curves (**Figure 9**a&**10**a), the specific capacities of both electrodes as a function of current density are given in **Figure 10**b. It can be seen clearly that the EG@Fc-MS exhibits a specific capacity of 196 mC cm^{-2} (or a capacitance of 326 mF cm^{-2}) at a current density of 2 mA cm^{-2}, which is almost twice than that of EG (107 mC cm^{-2} or 178 mF cm^{-2}). The contribution of the faradic Fc-MS material is thus equal to 89 mC cm^{-2}, a value larger by almost two orders of magnitude than that reported for a similar ferrocene functionalized film deposited onto a flat electrode surface[149], confirming the interest of the large area and highly porous EG support. Generally, compared with double-layer materials, the faradic materials always show limited rate performance due to the slow electrons and ions transfer processes. But the electron-hopping governed redox process operating here is a very fast reaction, and the capacity of EG@Fc-MS can remain at 69% of its larger value at a current density as high as 100 mA cm^{-2} (135 mC cm^{-2} or 224 mF cm^{-2}), which is even better than the 52% observed for the purely capacitive EG electrode under the same condition.

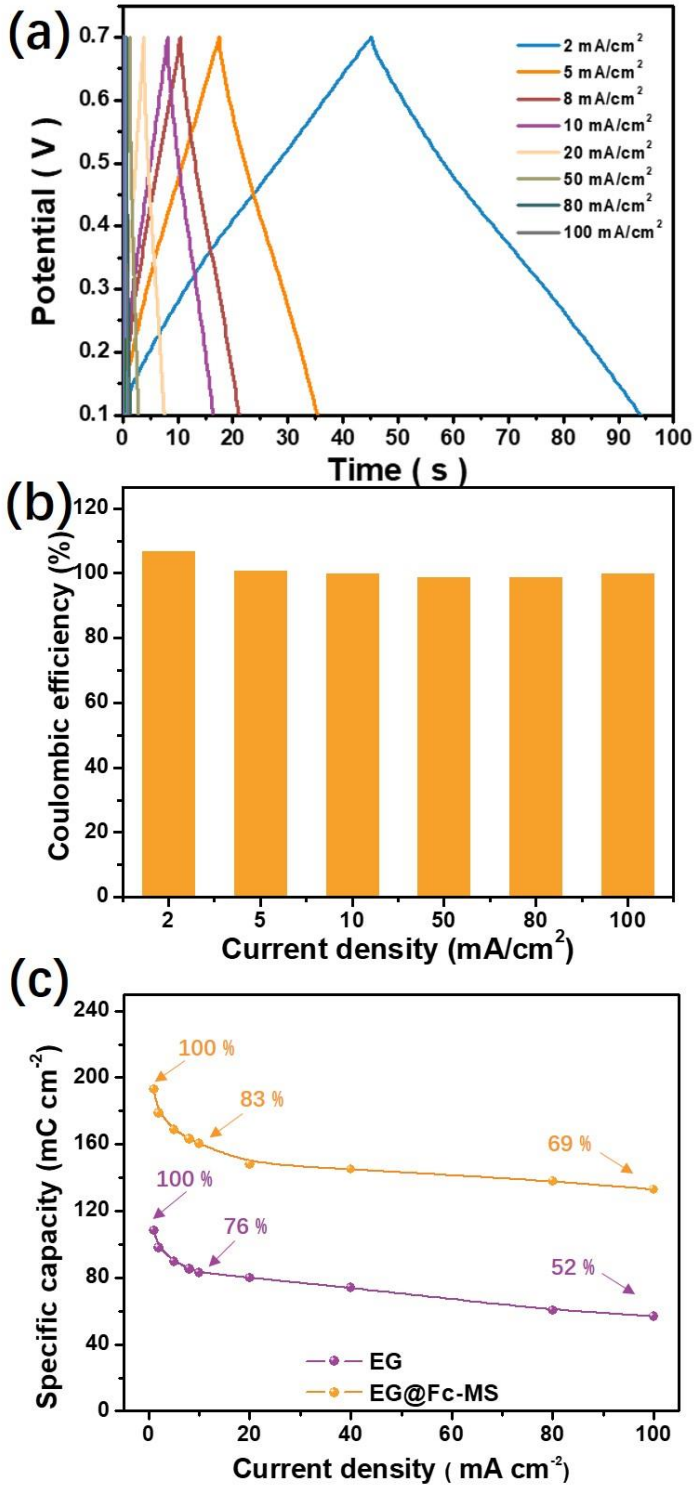

Figure 10. (a) Charge-discharge curves of EG; (b) The corresponding coulombic efficiency; (c) The rate performance comparison between EG and EG@Fc-MS.

The normalized rate performance (excluding the effect of capacity) of EG@Fc-MS and some recently reported faradic materials[120,174–180] are plotted in **Figure 11**. The rate performance of EG@Fc-MS is better than traditional faradic materials, with a capacity retention of 69% even at a C-rate value of 3800 h^{-1}, which is even comparable to the graphene thin film electrode, further demonstrating the advantage of the electron-hopping processes. Capacitance and capacity retention can also be evaluated from integrating the CV curves at various potential scan rates (**Figure 12**a), giving rise to the same conclusions as for galvanostatic experiments. The EG@Fc-MS also delivers a long cycle lifespan and 98% of the initial capacitance can remain after 1000 successive CV cycles (**Figure 12**b). Moreover, from such integration, one can estimate an amount of electrochemically accessible redox molecules of ca. 0.2 mg cm^{-2}, which represents about 80% of its total content in the film (0.25 mg cm^{-2}, as obtained from chemical analysis). This means the electron hopping occurs efficiently in most of the composite material volume despite the isolating properties of the silica matrix.

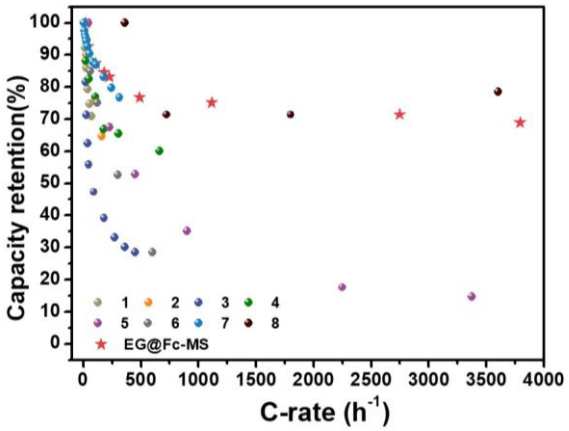

Figure 11. Comprehensive plots of normalized rate performance for EG@Fc-MS and several faradic materials reported in recent years: 1) Ni-Mn hydroxide on carbon nanofoam; 2) Co-Cd selenide nanorods; 3) Li_2MnO_3 nanorods; 4) Ni-Co hydroxide on carbon fibers; 5) Fe_2O_3/polypyrrole nanoarrays on carbon cloth; 6) n-butyllithium-treated Ti_3C_2Tx MXenes; 7) amorphous Ni-Co-Mn hydroxides； 8) graphene thin film electrode.

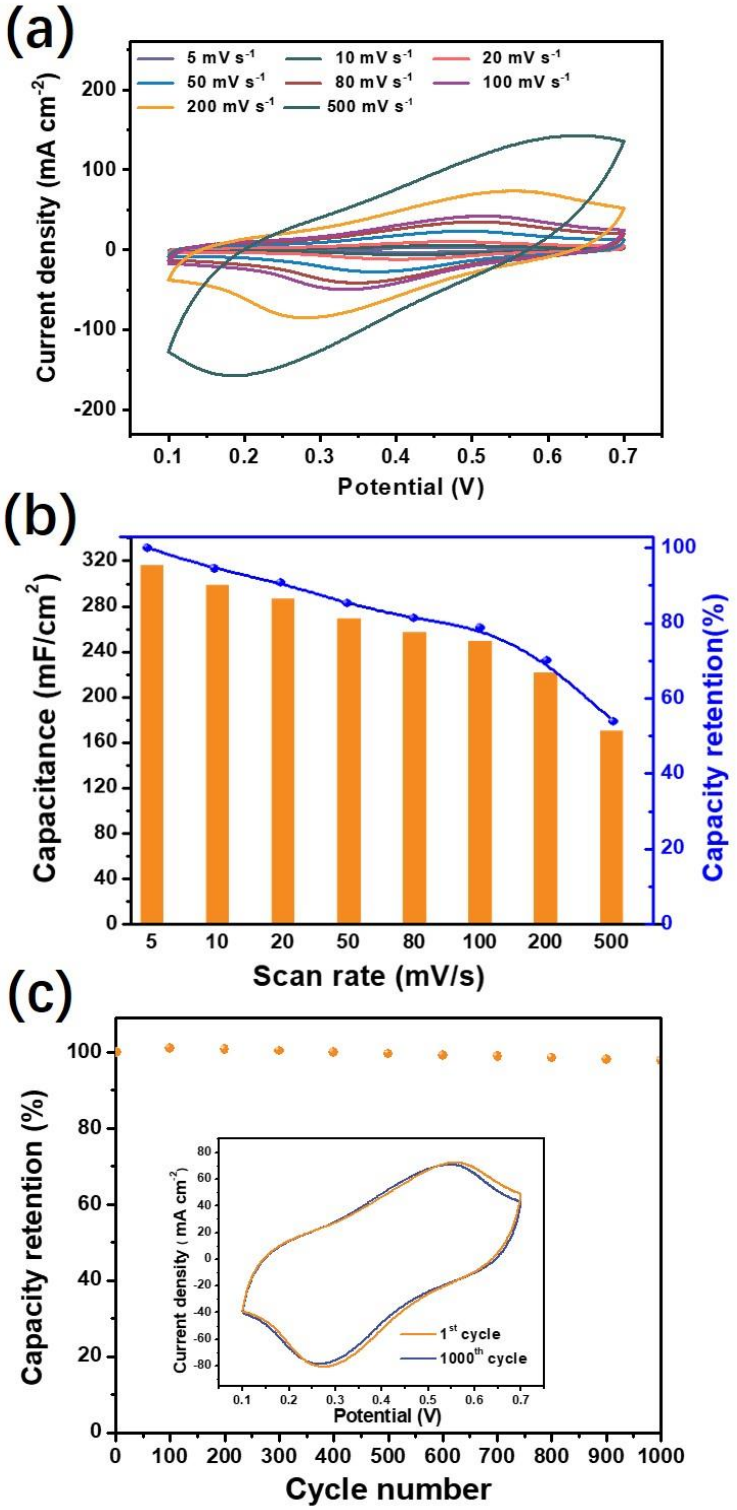

Figure 12. (a) The CV curves of EG@Fc-MS at various scan rates, and (b) Corresponding capacitance calculated from by the integration method; (c) The cycling performance tested by the consecutive CV method.

The energy storage behavior of EG@Fc-MS is firstly analyzed by analyzing CV curves over a wide range of scan rates from 5 mV/s to 500 mV s^{-1} (**Figure 12**a). Its behavior can be evaluated by fitting the redox peak currents vs. scan rates with the equation of $i = av^b$, and the empirical b value is an indicator of the type of reaction. A b value of 0.5 represents a diffusion-controlled behavior (battery-type), while b value of 1 is indicative of surface-controlled charge transfer (ideal capacitive energy storage process). As shown in **Figure 13**a, the fitting results of EG@Fc-MS approach the ideal value of 1 (0.91 in average for cathodic redox peaks and 0.88 for anodic redox peaks), over a wide range sweep rate from 5 mV s^{-1} to 500 mV s^{-1}, indicating the redox of ferrocene is mostly a fast surface-controlled reaction. To obtain the quantitative capacitive contribution at a fixed scan rate, the CV results of EG@Fc-MS are further fitted with the following equation (2):

$$i(V) = k_1 v + k_2 v^{0.5} \quad (2)$$

Where $k_1 v$ and $k_2 v^{0.5}$ represent the surface-controlled current and diffusion-controlled current respectively.

The fitting result reveals that 85.5 % of the total current of the anodic peak comes from the surface-controlled process at the scan rate of 20 mV s^{-1} (**Figure 13**b). Such high ratio for EG@Fc-MS further confirms the fast transport of counter-ions, which are not restricting the charges transfer processes by electron-hopping (Eq. 1), in contrast to conventional faradic materials (e.g. insertion or intercalation type of faradic materials[105,181]).

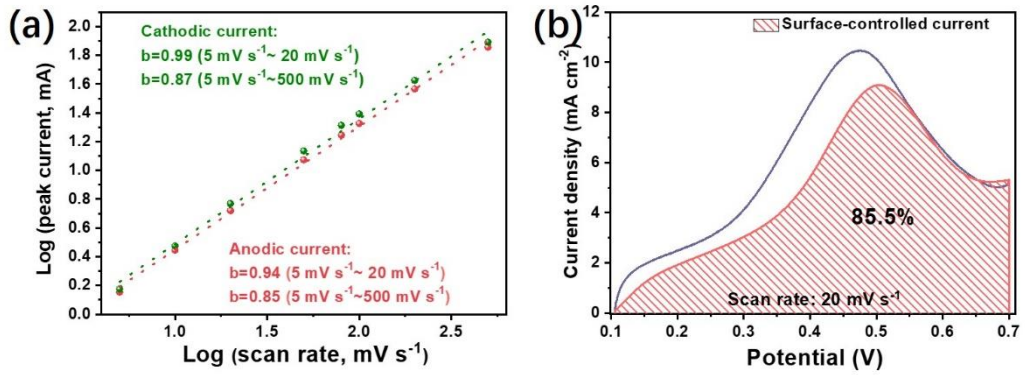

Figure 13. (a) Variation of CV peak currents for EG@Fc-MS as a function of the logarithm of scan rates (from 5 to 500 mV s^{-1}); (b) Ratio of the surface-controlled current of the oxidation process at the scan rate of 20 mV s^{-1} (marked by the shaded region).

Electrochemical Impedance Spectroscopy (EIS) is also used to analyze the energy storage originating from the electron hopping process, in the frequency range from 100 kHz to 0.1 Hz at the open circuit potential, and the Nyquist plots for EG and EG@Fc-MS are given in **Figure 14**a. At high frequency, the intersection point on the real axis represents the ohmic resistance of the electrolyte and the internal resistance of the electrode (R_s), which is very small and similar for both EG (0.95 Ω) and EG@Fc-MS (0.65 Ω) due to the good conductivity of the graphene/graphite substrate. In the high to middle frequency region, a semi-circle indicative of the charge transfer resistance (R_{ct}) is usually observed for faradic materials[182–184], the diameter of which being as small as high are the charge transfer kinetics. Here, such charge transfer resistance is negligible (no noticeable semi-circle) not only for EG but also for EG@Fc-MS, which demonstrates a fast and efficient electron hopping process involving the redox-active ferrocene moieties attached to the material. The tail at low frequency of the Nyquist plot corresponds to the diffusion limiting process. The similar and nearly vertical lines for EG and EG@Fc-MS show both of them own fast ions diffusion and prove the coating of the silica layer on the surface of graphene will not affect significantly the ions diffusion, confirming the interest of graphene sheets to facilitate electrolyte

penetration and pseudocapacitance[185]. The electrolyte ions diffusion coefficient (D_0) can be evaluated with the aid of equations (3) and (4):

$$D_0 = R^2T^2/2A^2n^4F^4C^2\sigma^2 \quad (3)$$

$$Z' = R_s + R_{ct} + \sigma\omega^{0.5} \quad (4)$$

Where D_0 is the diffusion coefficient, R is the gas constant, T is the absolute temperature, A is the electrode surface area, n is the number of electrons, F is the Faraday's constant, C is the concentration of ions, ω is the frequency, and σ is the Warburg factor which is the slope of $\omega^{-0.5}$*vs* Z' plot.

By fitting our data (**Figure 14**b), D_0 values of 1.9×10^{-5} cm^2 s^{-1} and 1.4×10^{-5} cm^2 s^{-1} are obtained, respectively for EG@Fc-MS and EG electrodes. The similar and fast diffusion rates prove: 1) the existence of the highly porous silica film on the surface of graphene does not block the ions diffusion; 2) there is no solid diffusion process during redox reaction of ferrocene molecules, indicative of the fully solution-phase exposed active sites (contrary to what happens in insertion-based materials for instance). The phase angle variation on frequency (Bode phase plot) for EG and EG@Fc-MS is plotted in **Figure 14**c. At the low frequency of 0.1 Hz, the phase angle can achieve -79° for both of them, suggesting the behavior much likes an ideal capacitor[186]. The frequencies at the phase angle of -45° (f_0) representing the point at half-maximum capacitance are 1.70 Hz and 1.27 Hz for EG and EG@Fc-MS, respectively, indicating that the presence of the ferrocene functionalized silica film does not affect too much the charge-discharge rate performance[187]. The corresponding time constants τ_0 ($1/f_0$), i.e. the minimum time needed to discharge all the energy with an efficiency greater than 50%, are very short: only 0.59 s for EG and 0.78 s for EG@Fc-MS, yet not at the level of purely carbon nanomaterials[188]. but satisfactory for a porous carbon electrode covered with an electroactive layer[187]. Similar τ_0 for EG and EG@Fc-MS also demonstrates the low resistance to charge transfer and ions diffusion processes in Fc-

MS.

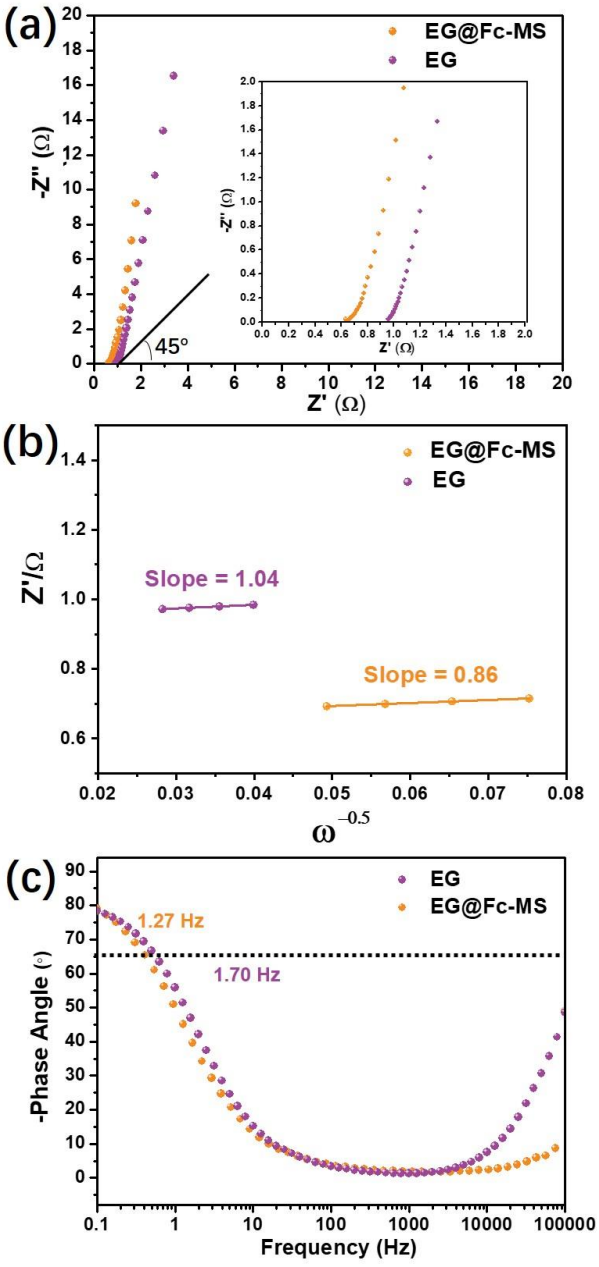

Figure 14. EIS data for EG and EG@Fc-MS electrodes recorded at open circuit potential in the frequency range 100 to 0.1 Hz: (a) Nyquist plots, (b) The variation of Z' as a function of frequency to the minus one half power, and (c) Bode phase plots.

3.3.3. Asymmetric hybrid cell assembly

In order to show the practical potential of the EG@Fc-MS electrode, a pseudocapacitor is further assembled by employing EG@Fc-MS as anode, EG as cathode (the area ratio of EG@Fc-MS to EG is 2) and 1M H_2SO_4 as the electrolyte. As shown in **Figure 15**a, the EG@Fc-MS//EG pseudocapacitor is able to stably work over the potential window from 0 to 1.2 V at scan rates ranging from 10 to 500 mV s^{-1}. Besides the double layer capacitance of graphene, an additional pair of broad peaks originating from the redox reaction of ferrocene confirms the energy storage contribution form the faradic reaction. The specific capacitances at various scan rates are calculated from CV curves, based on the total areas of the two electrodes (**Figure 15**b). A capacitance of 67 mF cm^{-2} can be delivered at the scan rate of 10 mV s^{-1}, and it can still maintain 32 mF cm^{-2} (47%) at 500 mV s^{-1}, 2.4 s discharging time. In contrast to the obvious plateau of batteries, the distorted triangle charge-discharge curves reveal the pseudocapacitor nature of the EG@Fc-MS//EG device (**Figure 15**c). The galvanostatic charge-discharge curves (at current density of 13.3 mA cm^{-2}), showing no obvious capacity fading even after 10 000 successive cycles (**Figure 15**d).

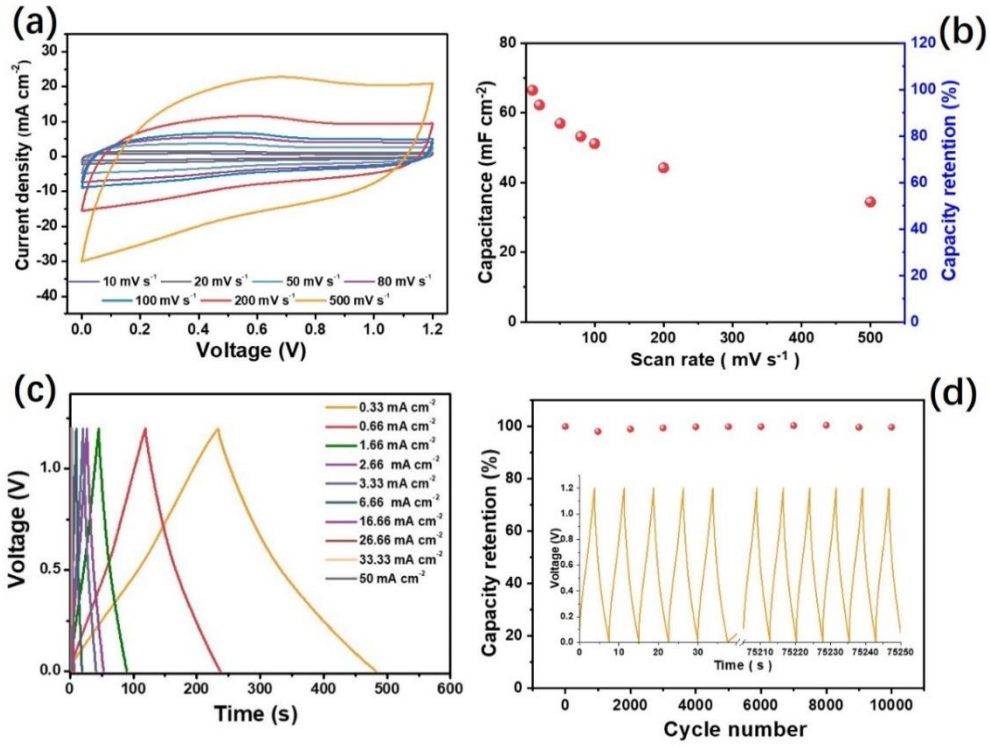

Figure 15. (a) The energy storage performance of EG@Fc-MS//EG hybrid pseudocapacitor in 1M H_2SO_4 (a) CV curves at various scan rates (from 10 to 500 mV s^{-1}); (b) Capacity values calculated from CV curves as a function of scan rate; (c) Galvanostatic charge-discharge curves of the device; (d) Cycling performance at constant current density of 13.3 mA cm^{-2} (initial and final five charge-discharge curves);

Ragone plots further reveal that the high energy density of 17.7 μWh cm^{-2} can be achieved at power density of 0.53 mW cm^{-2} and still remains as high as 9.2 μWh cm^{-2} at high power density of 13.7 mW cm^{-2}, being really competitive regarding recently reported supercapacitors performance[189–194] (**Figure 16**).

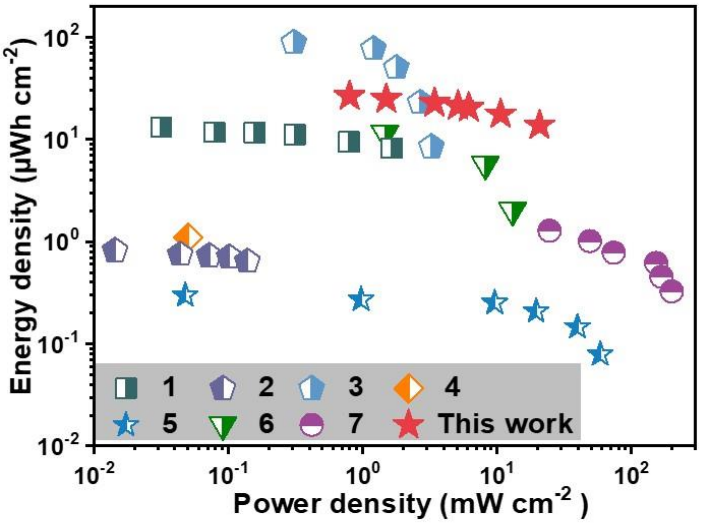

Figure 16. Ragone plots of the EG@Fc-MS//EG pseudocapacitor and previously reported capacitors: 1) polyethylene fibers covered by polydopamine, Ag and poly(3,4-ethylene dioxythiophene)/poly(styrenesulfonate); 2) poly(3,4-ethylene dioxy-thiophene): poly (styrenesulfonate)/ferritin nanoclusters within multiwalled carbon nanotube sheets; 3) graphene/MnO_2 ; 4) carbon nanotube yarns dotted with Co_3O_4 and NiO nanoparticles; 5) 3-D graphene carbon nanotube carpet; 6) actived carbon; 7) onion-like carbon.

3.4 Conclusions

An organic-inorganic hybrid material acting as a large-scale redox junction system has been developed through covalently anchoring ferrocene molecules on a mesoporous silica thin film electrogenerated onto the surface of a graphene-based electrode produced by electro-exfoliation of a graphite foil. Different from the traditional redox reactions (electrochemical insertion or intercalation), the electron-hopping mechanism operating here enables efficient and reversible transformation of surface-tethered ferrocene moieties with flexible linkers, thanks to fast charge transfer processes and low resistance to counter-ions diffusion. By further coupling with the good conductivity and large surface area of graphene/graphite substrate, the EG@Fc-MS electrode

exhibits a capacity of 196 mC cm^{-2} (326 mF cm^{-2}) at a current density of 2 mA cm^{-2}, of which 45% originates from the faradic Fc-MS layer. It delivers a remarkable capacity retention of 69% even at a high current density of 100 mA cm^{-2} (C-rate of 3800 h^{-1}). Finally, a pseudocapacitor (EG@Fc-MS//EG) is constructed and achieves a large energy density of 9.2 μWh cm^{-2} at a high power density of 13.7 mW cm^{-2}. This work well demonstrates the advantages of the electroactive mesoporous hybrid system consisting of a high density of molecular redox sites in terms of fast charge and mass transfer processes, high level of electroactivity and long cycling life, which may pave a new avenue on the construction of high-performance electrode materials for energy-related storage and conversion devices.

Chapter IV

Fabrication of Flexible Planar Micro-Devices Operating with Electron-Hopping Mechanism for Energy Storage Applications

It should be mentioned that this chapter only shows the feasibility of the developed protocol to fabricate flexible planar micro devices. However, more work has to be done in order to fully characterize the obtained material, and what we present here only some preliminary results.

4.1 Introduction

The last few decades have witnessed continuously surging demands of flexible and wearable microelectronics in various fields, such as biomedical sensors, wearable products, and sports assist devices etc.[195,196] Therefore, these cutting-edge applications put further forward more rigorous requirements for the energy storage systems beyond higher energy and power densities, including being easily-miniaturized, robust mechanical properties, as well as higher flexibility.[197] Generally, conventional energy storage devices, mostly having vertical sandwich structures with two electrodes, one separator membrane, and filled electrolyte, are too difficult to be fabricated into flexible micro-devices due to the complex configurations. [198] In contrast, in-plane interdigitated devices, comprising planarly-aligned but spatially-separated energy storage materials with electrolyte coating onside directly, have gained more and more research interest in recent years. This idiosyncratic design offers several merits over the traditional sandwich structure in terms of the energy storage devices: 1) the distance between the adjacent working and counter electrodes could be minimized to some extent through advanced patterning techniques, which could reduce the internal resistance of the devices and improve their power output; [199] 2) the monolayer nature

of the in-plane structure could largely increase the volume energy density by decreasing the thickness of devices, and also reduce short-circuit risks triggered by the external forces. 3) the simplified architecture also makes it easier to be incorporated into electronic devices, and even suitable as the wearable power sources when utilizing superior flexible supporting materials as substrates that can bear the long-term twisting and folding distortions.

Featured with large surface area (~2630 $m^2 g^{-1}$), excellent electrical conductivity (~10^4 S cm^{-1}), and robust mechanical properties (Young's modulus of ~1TP) [200], graphene is widely used as the active material for flexible in-plane energy storage devices when integrated on various flexible substrates, such as polyethylene terephthalate (PET), polydimethylsiloxane (PDMS), and textiles etc.[201–203] Instead of directly utilizing graphene, graphene oxide is always chosen as the starting material to assemble these devices owing to its abundant functional groups, hydrophilic property, and high surface adhesion energy.[204] However, after the reduction processes, the products cannot recover the pristine graphene structure either in thermal, chemical or electro-chemical ways, therefore they always suffer from relative low conductivities.[205] Besides, one more technical difficulty to fabricate such devices lies in how to precisely pattern graphene on substrates so as to make full use of the surface space while avoiding the short-circuit problem. Several possible strategies have been developed in recent years including chemically coating graphene on prepatterned current collectors, [206] laser writing on in-situ reducing graphene oxide,[207] plasma etching,[208] and inkjet printing[209] etc. Nevertheless, these methods are still facing some drawbacks: dependence of sophisticated facilities, complicated preparation processes, utilization of organic solvent, limited graphene-loading amount. As such, developing a low-cost and facile method to assemble the high-quality graphene on flexible substrates in a dense and patterned way is pivotal to promote the development of this kind of interdigitated devices.

3D-printing, also known as additive manufacturing, is an advanced object fabrication technique based on the digitally controlled deposition in a layer-by-layer fashion. [210] This technology advances rapidly in recent years, and several mechanisms of 3D printing have been developed including photo-polymerization, extrusion, lamination, and powder bed fusion, with the resolution as high as 100 nm.[211] Therefore, utilization of printed items with the high resolution and programmable shapes as templates could be a low-cost and versatile way to pattern in-plane devices. Besides, a bottom-up electro-chemical method to in-situ exfoliate graphite into high-quality graphene with superior conductivity has been established by applying a large biased potential on the graphite electrode in sulfate-containing aqueous solution.[147] The sulfate ions could insert into the interspace between graphite layers under the electric field force, and meanwhile water is rampantly split into oxygen at the electrode interface, both of which could expand the graphite into few-layers graphene. However, the as-formed graphene flakes are more likely to be peeled into solution phase when prolonging the exfoliation time due to the lack of binding sites at graphite electrode, probably limiting the graphene density on the surface of graphite. In this work, an electro-exfoliation strategy of surface-confined graphite patterned with 3D printed templates is proposed to prepare the flexible graphene planar micro-devices with editable pattern, superior conductivity, and high graphene density. Moreover, as what we did in previous chapters, the mesoporous silica film functionalized with redox molecules has been further generated on the surface of graphene to achieve the construction of flexible planar electron-hopping systems, and to enhance its energy storage performance.

4.2 Experimental section

Preparation of the graphene planar micro-electrodes patterned with 3D printed objects (GPMs):

The 3D printed items with digitally editable shapes were first exposed into an inkpad to adsorb ink oil on their surface. The ink-covered templates were further put on the

sticky side of scotch tape to transfer the ink pattern onside. Subsequently, the as-patterned scotch tape was pasted on the surface graphite foil, followed by a peeling-off process, to hand over a layer of graphite on the scotch tape, where the ink-covered surface is blank due to the loss of stickiness. Similar to the electro-exfoliation method we used in the last chapter, the electro-exfoliation process was further performed in 0.1 M Na_2SO_4 aqueous solution with a two-electrode system, where a piece of graphite coated scotch tape electrode (graphite/scotch electrode) and platinum mesh (2.5 cm × 2.5 cm) were used as the working and counter electrode, respectively. The exfoliation was achieved by applying a voltage of 4 V for 240 s with a distance of 5 cm between the two electrodes. In order to recover the conductivity of the electrodes, an activation process has been used to remove the inserted sulfate ions via applying 0 V on the exfoliated electrode for 240s in a three-electrode system with Ag/AgCl as the reference. Finally, the as-prepared electrode, labeled as GPM-240, was thoroughly washed with deionized water and dried at room temperature overnight. Besides, different exfoliation times of 30 s, 60 s, 120 s, and 360 s were also conducted to investigate the structural evolution, and the corresponding products were labeled as GPM-30, GPM-60, GPM-120, and GPM-360, respectively.

Functionalization of GPMs with ferrocene functionalized mesoporous silica films (Fc-MS-GPM-240):

Similar to the method we used in the last chapter, the mesoporous functionalized silica films were grown on GPM-240 via a potentiostatic method by applying a cathodic potential of -1.5 V (vs. Ag wire pseudo-reference) on the electrodes immersed in the silane sol (described in chapter Ⅱ) for 8 s. The modified electrode was rapidly removed from the solution, rinsed with water, and dried at 130°C for 2 h, successively. The azide functionalized mesoporous silica film on GPM-240 was denoted Az-MS-GPM-240. Prior to the derivatization with ferrocene, the Az-MS-GPM-240 was dipped into an ethanol solution containing 0.1 M HCl, for 30 min, in order to remove the surfactant template. The CTAB surfactant free Az-MS-GPM-240 were further

functionalized through the typical click procedure (described in chapter II) to introduce the ferrocene molecules on the mesopores of the silica film, labelled as Fc-MS-GPM-240.

4.3 Results and discussions

4.3.1 Main characteristics of the GPMs and preliminary results showing the feasibility

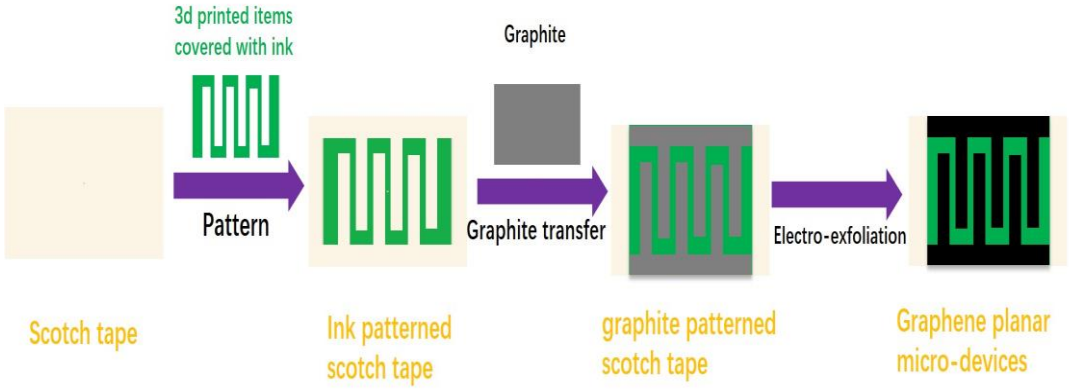

Figure 1. The scheduled process for the fabrication of graphene planar micro-devices.

The scheduled preparation process is illustrated in **Figur**e 1. A 3D printed object covered with ink has been used to pattern the scotch tape first, followed by a graphite transfer process by taking use of the adhesive property of the scotch tape, and a fast electro-exfoliation process to insitu convert the graphite into graphene within several minutes. It's a pity that the 3D-printing-related pattern processes have not been done yet because of the time limitation. Nonetheless, the feasibility of this proposed method is verified by a simple pre-experiment: the scotch tape with an ink line pre-drawing on the scotch tape by a marker has been used to peel off a thin layer of graphite from the graphite foil to simulate the proposed pattern processes. **Figure 2** shows the corresponding result, and it can be clearly seen that the ink line acts as the boundary separating two pieces of graphite layers on the scotch tape. Therefore, one could imagine that the pattern processes could also work if drawing ink patterns by 3D printed

objects. Of course, these are preliminary results, and the parameters, including the type and the thickness of ink lines, need to be optimized to improve the quality of the patterned graphite onside as the untidy boundary. At all events, the preliminary results have shown the feasibility of our idea somehow.

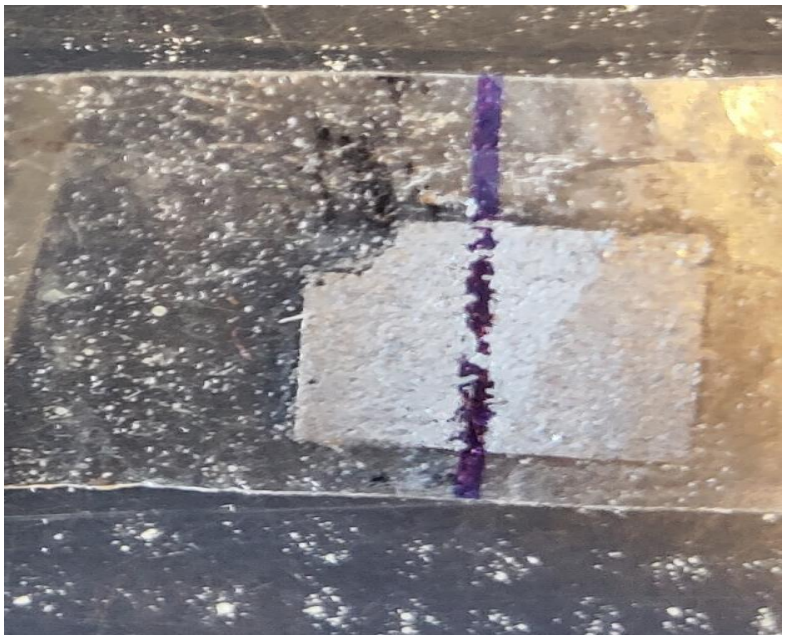

Figure 2. Preliminary result of the patterning process of graphite on the scotch tape.

The electro-exfoliation of graphite on the scotch tape has been conducted first to evaluate the graphene-formation processes. The electro-exfoliation curve under 4 V, given in **Figure 3**, is recorded in a two-electrode system, where graphite/scotch tape as the working electrode, platinum mesh as the counter electrode, and 0.1 M Na_2SO_4 aqueous solution as the electrolyte. After a fast drop from 75 mA cm^{-2} to 60 mA cm^{-2} within a few seconds, the exfoliation current gradually goes down from 60 mA cm^{-2} to 10 mA cm^{-2} until the exfoliation time reaches ca. 250s, and faces a steady region after that. The initial sharp fall of the current is probably due to the formation of electrical double layer process, which could normally finish the charging within a few seconds. Afterwards, the anodic current mainly comes from the sulfate ions inserted into the graphite interlayers and the oxygen evolution reaction, [147] both of which help to expand and separate the graphite layer into mono/few-layers of graphene. The

continuously decreased current indicates the consumption of the graphite reactant and the increasing resistance of the graphite/scotch electrode, because the inserted sulfate ions inside the exfoliated graphene could deteriorate the conductivity, which is confirmed by the later activation experiments. The following current-steady region could be a signal that all graphite on scotch tape has been converted into graphene, and the remaining current could be the balance of the inserted sulfate ions between the electrical driving force and the thermodynamic distribution. The inset of **Figure 3** also gives several digital photos of the electro-exfoliated graphite electrodes with different exfoliation time. The color of the exfoliated electrode, the part above the yellow line, gets darker from grey with prolonging the exfoliation time, indicative of the graphene formation.

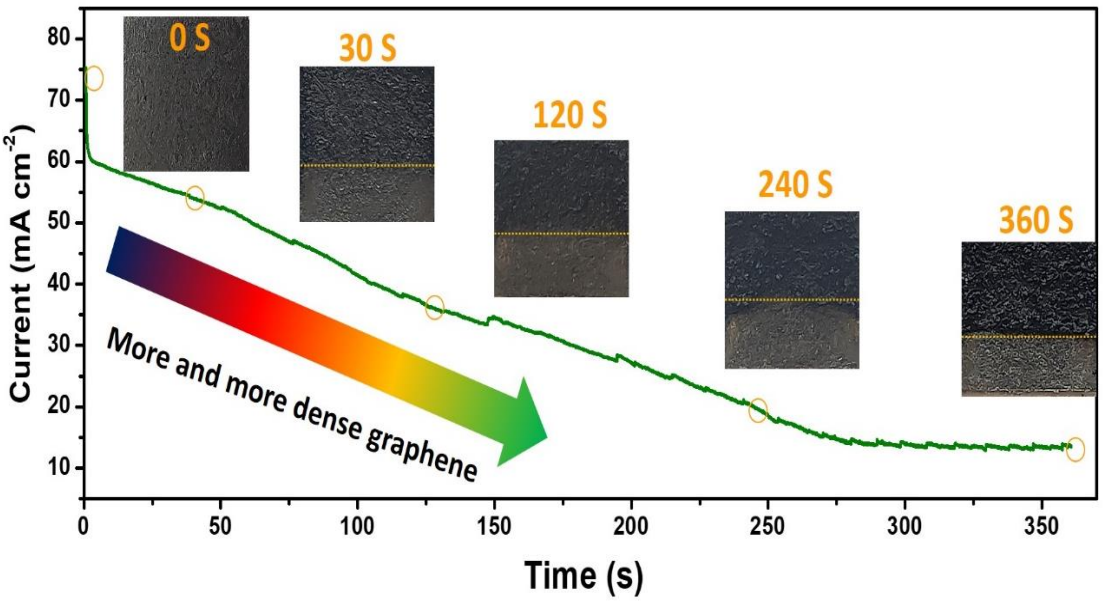

Figure 3. Chronoamperometry curves of the exfoliation process of the graphite/scotch electrode, and digital photos of the electrode at the different exfoliation time.

As shown in the I-V curve of **Figure 4**b, compared with that of pristine graphite/scotch electrode, the resistance of the obtained electrode increases a lot after the electro-exfoliation processes, making it difficult to be directly used in the energy-related fields. The decrease of electrode conductivity could be mainly due to the insertion of insulating sulfate ions into the graphite crystal, and the strong electric field will keep them inside

even after finish the exfoliation process. From another point of view, the almost total loss of conductivity indicates that the whole graphite on the scotch tape takes part in the electro-exfoliated reaction. A simple electro-activation process is adopted by applying a 0 V potential (vs. Ag/AgCl reference electrode) on the exfoliated electrodes in 0.1M Na_2SO_4 aqueous solution for 240s to expel the inserted sulfate ions and to recover the conductivity. The current of the activation process is recorded and shown in **Figure 4**a**,** and a strong cathodic current ranging from -35 mA cm^{-2} to -1 mA cm^{-2} can be observed at the beginning 40 s, which may come from the fast move-out of the negatively charged sulfate ions located at the surface/near-surface of graphene. For the period from 40s to 240s, the current delivers a slowly decreased trend from -1 mA cm^{-2} to -0.25 mA cm^{-2}, and the much smaller but relative steady current may reflect the leaching of sulfate ions from the lattice of few layers of graphene and un-exfoliated graphite. After activation, most sulfate ions are removed from the graphene electrode, and its conductivity recovers back to the same level of the graphite/scotch tape electrode, despite a little bit worse.

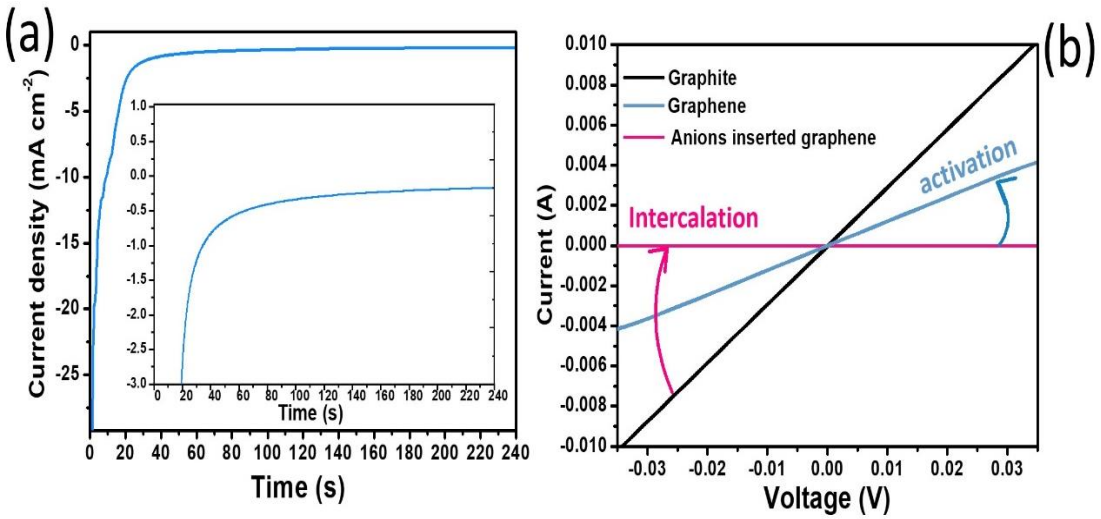

Figure 4. (a) Chronoamperometry activation curve of the electro-exfoliated graphene electrode via applying a 0 V potential onside for 240 s in a three electrode system where graphene/scotch tape, Ag/AgCl, and platinum act as the working electrode, the reference electrode, and the counter electrode, respectively; (b) The I-V curves of the graphite/scotch electrode, GPM-240 before activation, and GPM-240 electrode.

The impedance spectra of this set of electrodes (**Figure 5**) well agree with the previous hypothesis. The x-axis intercept in the high-frequency region represents the electrode internal resistance. As it can be seen, the resistance of graphite/scotch electrode is ~4 Ω, while its resistance soars to as high as ~1500 Ω after the electro-exfoliation process due to the sulfate ions intercalation. The internal resistance of the GPM recovers back to the same level of the graphite/scotch electrode, ~12 Ω after the removal of sulfate ions, well agreed with the I-V results. Compared with that of the graphite/scotch tape electrode and the GPM, the small slop of the sulfate-inserted graphene in the low-frequency region also implies a slow solid-phase ions diffusion process.

These results confirm that anions, sulfate ions here, will insert into the graphite lattice during the high-voltage exfoliation process, and thus deteriorate the conductivity of the as-obtained electrode. Nevertheless, the anions inside the electrode could be reversibly expelled out via applying a 0 V potential, and thankfully the conductivity of the electrode can be recovered to a great extent. Overall, a scotch tape assisted exfoliation has been proved an efficient method to generate graphene planar micro-electrode, and the conductivity of the as-formed electrodes can be recovered by a subsequently simple electro-activation process to expel the inserted sulfate ions.

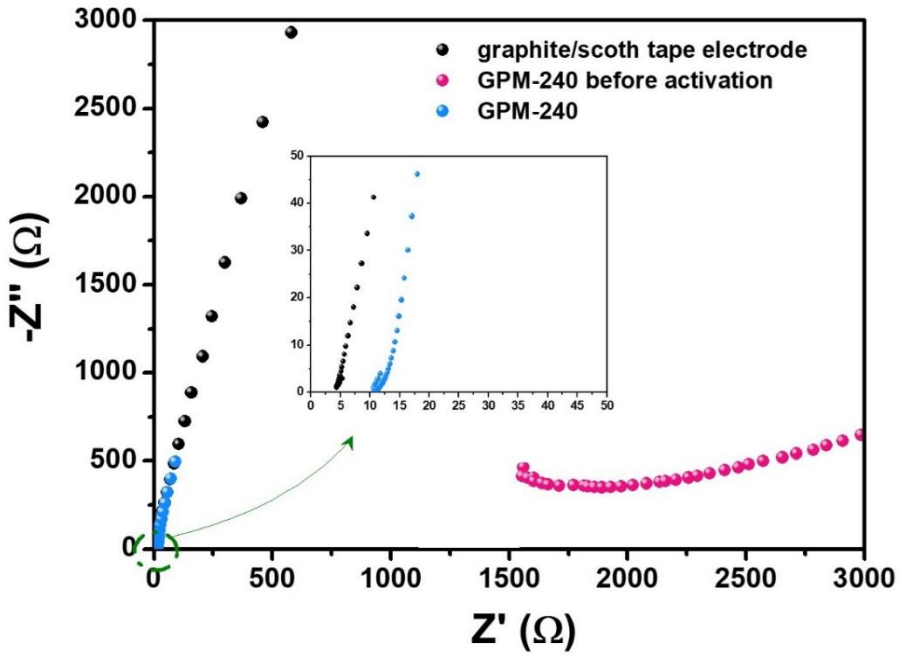

Figure 5. Nyquist plot of the graphite/scotch tape electrode and GPM-240 before and after activation, at the open circuit potential in a three-electrode system.

The microstructure of the graphite/scotch electrode and GPM-240 electrode have been characterized by the field emission scanning electron microscopy (FE-SEM) to provide the solid proof of the conversion from graphite to the graphene during the electro-exfoliation process. The corresponding images with different magnifications are given in **Figure 6**. As shown in **Figure 6**a, the compact graphite layer with a thickness of ~50 μm can be observed for the graphite/scotch electrode, and the underlying brightest region arose from charges accumulation effect is the insulating scotch tape substrate. After the electro-exfoliation, taking the GPM-240 as an example, the thickness of graphite layer significantly expand to ~ 110 μm with highly porous and sheet-like structure. (**Figure 6**b) The corresponding high-resolution image (**Figure 6**c) further confirms graphene sheets with the thickness of ~8 μm (4-layers graphene) can be formed during the exfoliation.

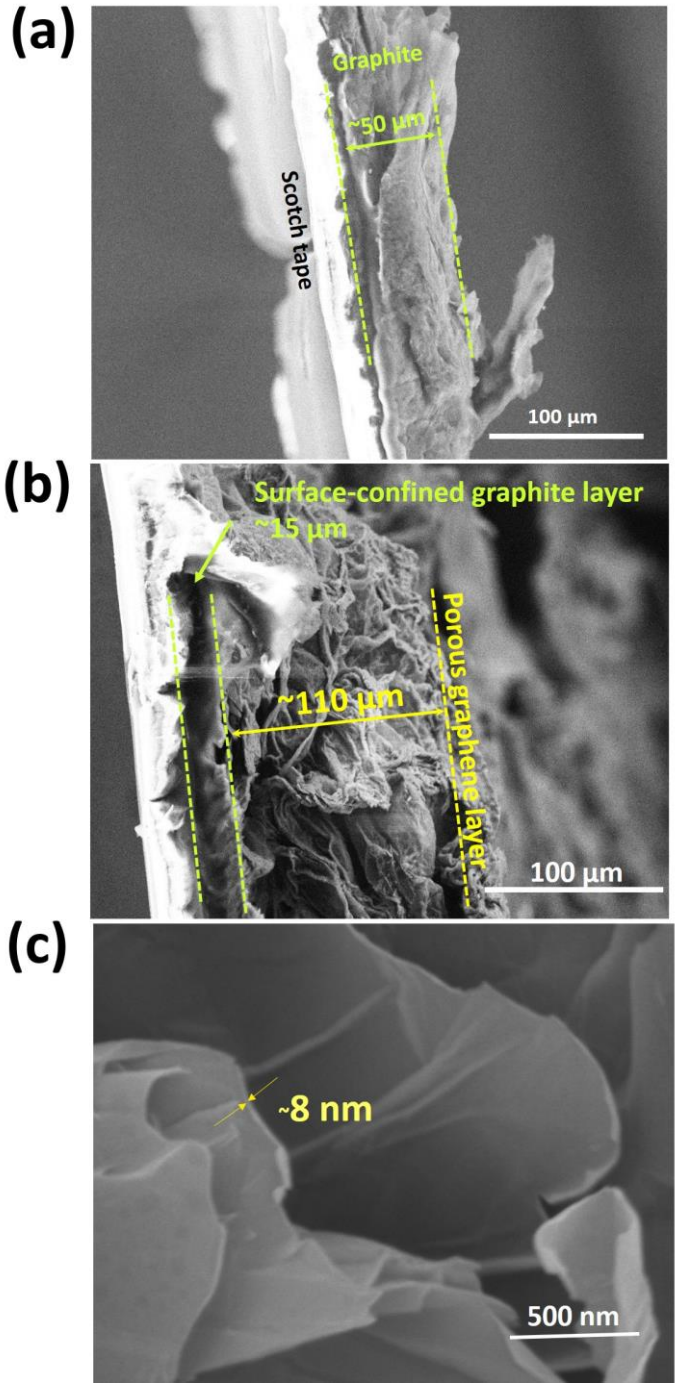

Figure 6. (a) SEM images of graphite/scotch electrode; (b-c) The PGM-240 electrode with different magnifications;

There are some interesting phenomena: 1) the graphite region neighboring the scotch (~15 µm thickness) remain compact even after exfoliation, indicating the lattice expansion of this zone is restrained due to the adhesive surface of the scotch tape. 2)

most of the formed graphene flakes still stay on the scotch tape to form the thicker graphene layer, instead of falling off to the aqueous phase. These behaviors are obviously different from the direct electro-exfoliation of the graphite foil, like what we did previously. As discussed in the last chapter, the exfoliation of the graphite foil would split the graphite monolith into several separated graphite grids, and insitu generate graphene layer on their surface. (**Figure 7** a&b) In contrast to ca. 110 μm of GPM electrodes, what needs to be noted is the thickness of this new-formed graphene layer is only just a few micrometers (**Figure 7**b). Besides, the current response during the exfoliation of graphite foil also appears different, and a relatively steady current can be obtained during the graphite foil exfoliation, despite the gradual decrease (probably due to the reduced active materials). And, the new formed graphene flakes prefer to fall into the aqueous phase, instead of remaining on the electrode. If prolonging the exfoliation time, the entire electrode will be fully decomposed, as shown in the digital photo of **Figure 7**d. The lack of binding sites, namely the adhesive surface of the scotch tape, might be the reason. The continuously exposed graphite layer beneath the exfoliated region could sustainedly take part into the reactions, and generate bubbles blowing off new-formed graphene flakes, which could explain its constant exfoliation current and the fast fall-off of graphene flakes during the electro-exfoliation. Therefore, the adhesive scotch tape might play a pivotal role that significantly changes the exfoliation behavior, and a thick exfoliated zone (~115 μm) can be formed on the top of the scotch tape surface.

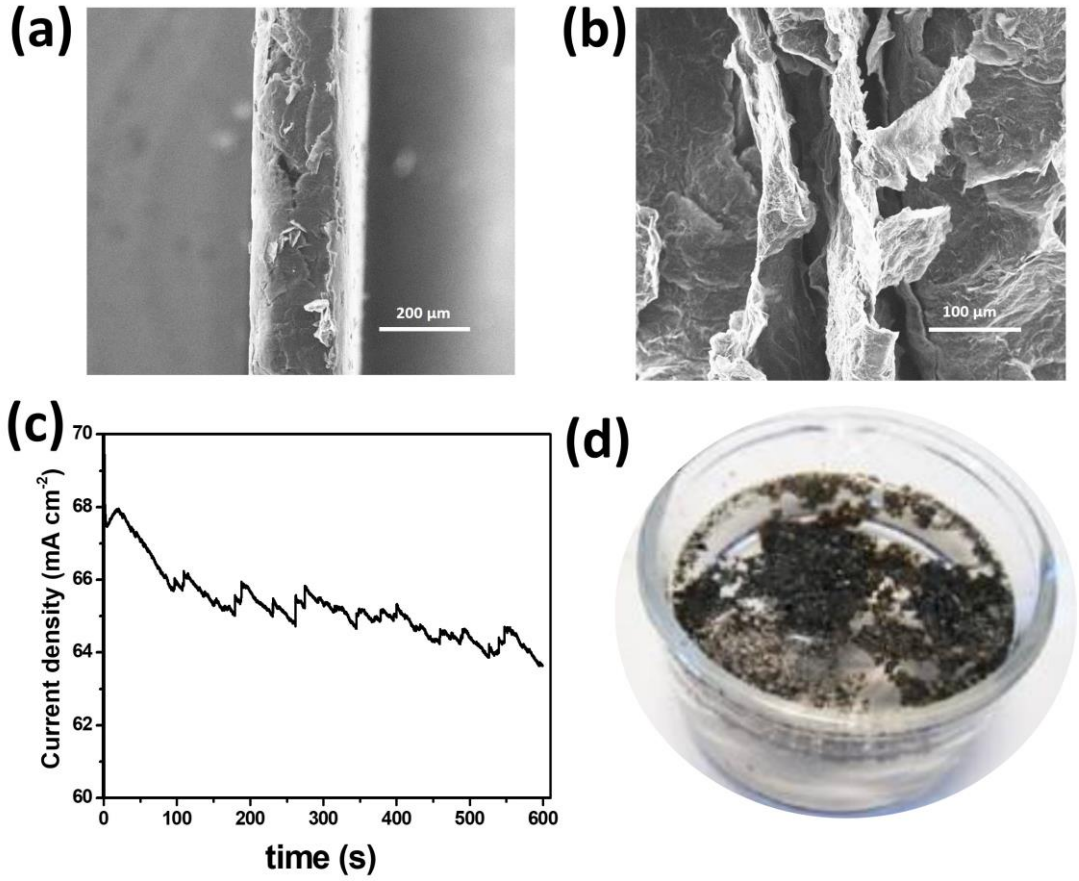

Figure 7. (a&b) Morphology of the pristine graphite foil, and electro-exfoliated graphite foil under 4 V in 0.1M Na_2SO_4 electrolyte for 600 s; The corresponding current response vs. time for the exfoliation process (c); (d) The digital photo for the aqueous bath after the electro-exfoliation process, containing numerous graphene flakes.

4.3.2 The energy storage performance of GPMs

Back to the plotline of this chapter, the energy storage performance of GPMs electrodes are evaluated to quest for the best electro-exfoliation time. The CV curves of GPMs and the graphite/scotch tape electrode are recorded in a three-electrode system at 50 mV s^{-1}, where GPMs (or graphite/scotch tape), platinum mesh, silver/silver chloride, and 1 M H_2SO_4 aqueous solution are the working electrode, counter electrode, reference electrode, and electrolyte, respectively. The results, given in **Figure 8**a, show that the current response of original graphite/scotch tape electrode delivers a rectangle-like shape with relative small intensity, indicative of the pure electrical double layer process

with a relatively small electroactive surface area. The current response significantly magnifies with prolonging the electro-exfoliation time until 240 s, which confirms the largely increased electroactive surface area from the new-generated graphene. However, the current response of GPM-240 and GPM-360 are highly overlapped, which implies the applied voltage will not change the structure of GPMs electrode after 240s. This phenomenon further confirms the electro-exfoliation of the graphite/scotch electrode is different from that of the graphite foil electrode, where a clear capacity decrease can be observed when the exfoliation time exceeds the threshold time. Besides, a pair of highly symmetrical weak redox peaks at ca.0.35 V can be found in the CV curves of GPMs, especially for those with long exfoliation time like GPM-120, GPM-240, and GPM-360. As discussed in the last chapter, the redox peaks perhaps come from the adsorption/desorption of protons in oxygen-containing functional groups generated from the oxidation of graphene surface under the high exfoliation voltage.

The relations between the electroactive surface area (current response during the cyclic voltammetry) and the exfoliation current are shown in **Figure 8**b. With prolonging the exfoliation time, the exfoliation current steadily decreases until 240s and reaches a stable state afterwards. The electroactive surface area sees the opposite trend. Compared with the electroactive surface area of graphite, it gradually increases 11 times until the exfoliation time reaches 240s, and then remains stable. Therefore, the exfoliation current could be an indicator of the structure evolution of GPMs, and a lower exfoliation current implies a higher degree of graphenization. The electro-exfoliation of 240s is the optimized time for preparing the GPMs to achieve the maximal graphene density while consuming minimal energy and time. As a result, GPM-240 is the optimal sample, and its energy storage properties are evaluated in the following work in detail.

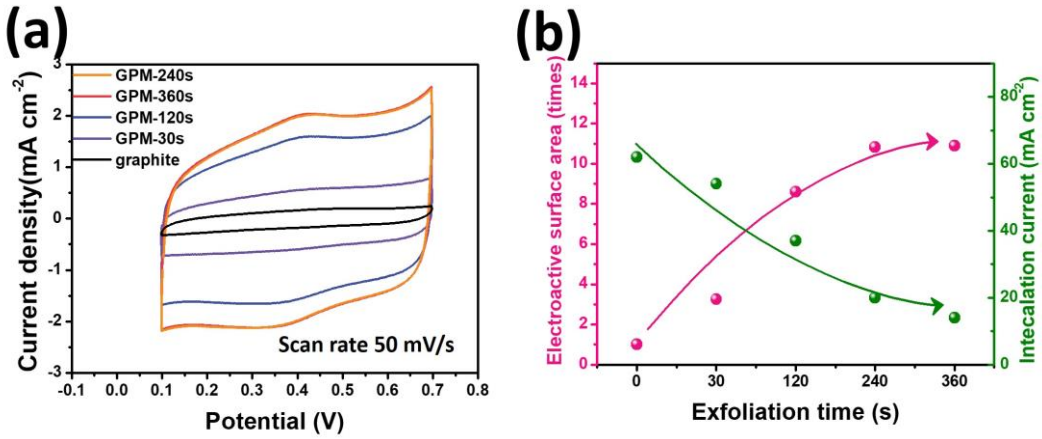

Figure 8. (a) Cyclic voltammetry curves of the pristine graphite foil and GPMs with different exfoliation time, recorded from a three electrode system in 1 M H_2SO_4 aqueous solution at a scan rate of 50 mV s^{-1}; (b) The relation between the electro-exfoliation time and the anodic exfoliation current/the electroactive surface area on the assumption that the initial graphite electroactive surface are is equal to 1.

The cyclic voltammetry curves of GPM-240 are recorded in a three-electrode system (GPM-240, platinum mesh, and Ag/AgCl as the working electrode, the counter electrode, and the reference electrode, respectively) at different scan rates from 5 mV s^{-1} to 200 mV s^{-1} in 1 M H_2SO_4 aqueous solution. The corresponding results in **Figure 9**a show the rectangular shape, despite a pair of very small redox peaks at ca. 0.35 V coming from oxygen-containing functional groups, no matter at a relative small scan rate of 5 mV s^{-1} or at a high scan rate of 200 mV s^{-1}. The well-maintained rectangular shape and the nearly 90^o turning at the switch potential (even 82^o at the scan rate of 200 mV s^{-1}) demonstrate a good electrical double-layer behavior, proving the negligible internal resistance and fast ions diffusion process during charge-discharge processes, indicating the superior rate performance. The energy storage ability of GPM-240 is assessed with the galvanostatic charge-discharge technique with current densities from 0.5 mA cm^{-2} to 8 mA cm^{-2}. In spite of a slightly distortion at ca. 0.35 V, the symmetrically triangular charge-discharge curves show the pure electrical double-layer energy storage process and high coulombic efficiency. The energy storage capacity of

GPM-240 can be calculated based on these curves, and it exhibits 24.5 mC cm^{-2} (40.8 mF cm^{-2}) at a current density of 0.5 mA cm^{-2} and still maintain 81% at a high current density of 8 mA cm^{-2}.

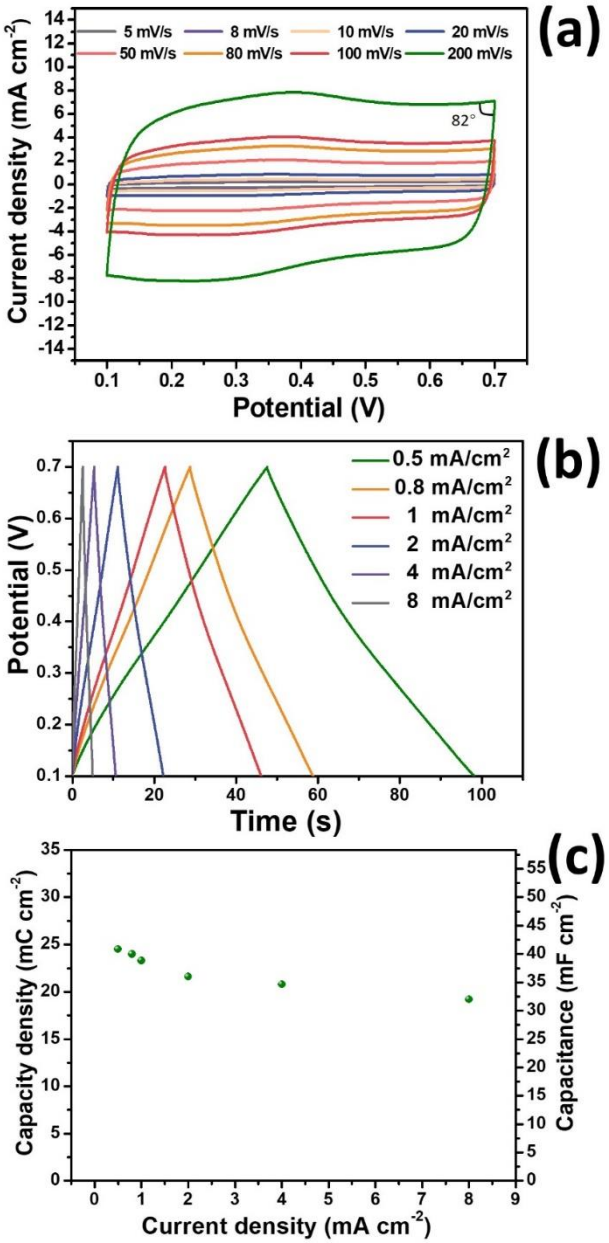

Figure 9. Energy storage performance of GPM-240 in a three electrode system (vs. Ag/AgCl) with 1 M H_2SO_4 solution as the electrolyte. the CV curves recorded at different scan rates ranging from 5 mV s^{-1} to 200 mV s^{-1} (a); The galvanostatic charge-discharge curves with current densities from 0.5 mA cm^{-2} to 8 mA cm^{-2} (b); The rate performance calculated from the galvanostatic charge-discharge curves (c).

The last chapter has proved the ferrocene functionalized silica film can be well generated on the surface of electro-exfoliated graphene, to enhance its energy storage capacity by introducing the faradic reactions while maintaining its original electrical double layer capacity. Therefore, it should be interesting to coat such ferrocene functionalized silica film onside GPM-240 to further improve its capacity and to achieve the construction of flexible electron-hopping devices with the help of the flexible scotch tape substrate. Following the similar protocol of the last chapter, the ferrocene functionalized mesoporous silica thin film is further grown on the surface of GPM-240, and the obtained sample is labelled as Fc-Ms-GPM-240. Its morphology is shown in **Figure 10** a&b. Similar to that of GPM-240, the structure of Fc-Ms-GPM-240 still maintains a highly porous structure composed of numerous nano-sheet, but the thickness of the sheets increases to ~70 nm from ~ 8 nm. The EDX-mapping is further used to acquire the chemical information of Fc-Ms-GPM-240. The corresponding results prove that C, O, Si, and Fe homogenously distribute on the surface, demonstrating the uniform coating of ferrocene functionalized silica film on the surface of the electro-exfoliated graphene with the thickness ~ 60 nm.

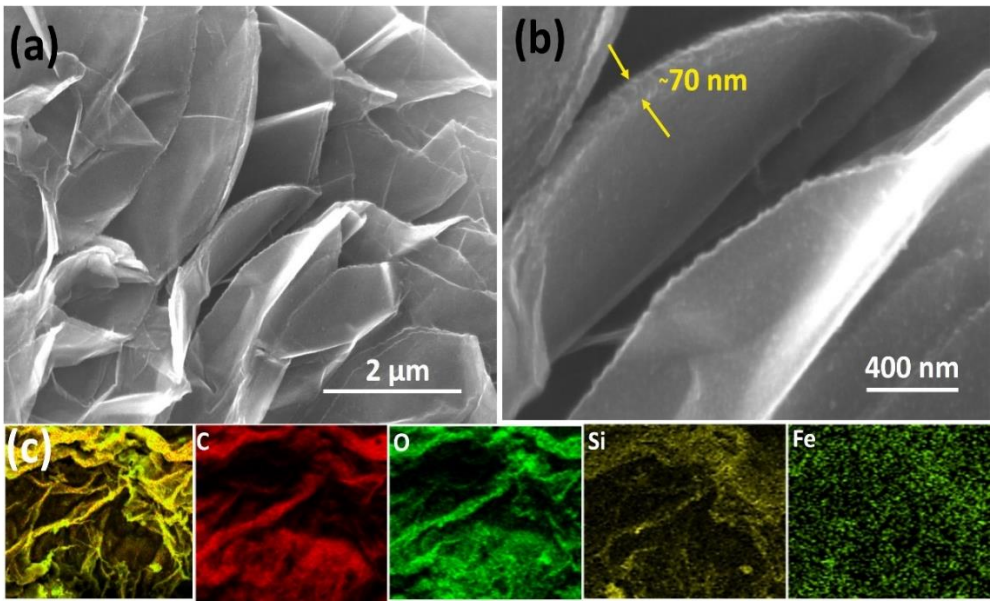

Figure 10. (a&b) Morphologies of Fc-MS-GPM-240 with different magnifications; (c) the EDX-mapping results showing the elements distribution of C, O, Si, Fe.

The energy storage performance of Fc-MS-GPM-240 is analyzed in a three-electrode system with the same configuration as mentioned before. **Figure 11**a gives the comparison of the CV curves between GPM-240 and Fc-MS-GPM-240 at the same scan rate of 20 mV s^{-1}. Similar to the results of the last chapter, a pair of redox peaks located at ca. 0.35V can be observed, coming from the redox reaction of the ferrocene molecules. In addition, the current responses of GPM-240 and Fc-MS-GPM-240 are almost overlapped at the non-faradic region (0.1 V~0.2 V), which proves the existence of the mesoporous silica film on the surface of graphene will not affect the capacity originating from electrical double layer process too much. The CV curves of the Fc-MS-GPM-240 with different scan rates from 5 mV s^{-1} to 200 mV s^{-1} are given in **Figure 11**b. With increasing the scan rate, the peak-to-peak separation also increases due to the stronger polarization effect, but the CV curves remain symmetry even at a high scan rate of 200 mV s^{-1}, indicating the reversible nature of the ferrocene redox reaction. The galvanostatic charge-discharge curves of Fc-MS-GPM-240 with current densities from 0.5 mA cm^{-2} to 8 mA cm^{-2} are given in **Figure 11**c. Unlike the triangular curves of GPM-240, obvious distortions from ca. 0.3 V to ca. 0.5 V can be observed in both charging and discharging branches, well consistent with the redox regions in the CV curves. The steady potential increase/decrease with a function of charging/discharging time in this distortion window is a sign of the surface-controlled nature of the ferrocene redox reaction, showing the fast electrons and counter ions transfer behaviors. Besides, a similar time for the charging/discharging branches illustrates high coulombic efficiency, and most electrons stored in the materials can be released during the energy storage processes. The capacity of Fc-MS-GPM-240, calculated from the charge-discharge curves, is 37 mC cm^{-2} at the current density of 0.5 mA cm^{-2}, and can remain 27.5 mC cm^{-2} (74% of the initial capacity), which are much higher than that of the pristine GPM-240.

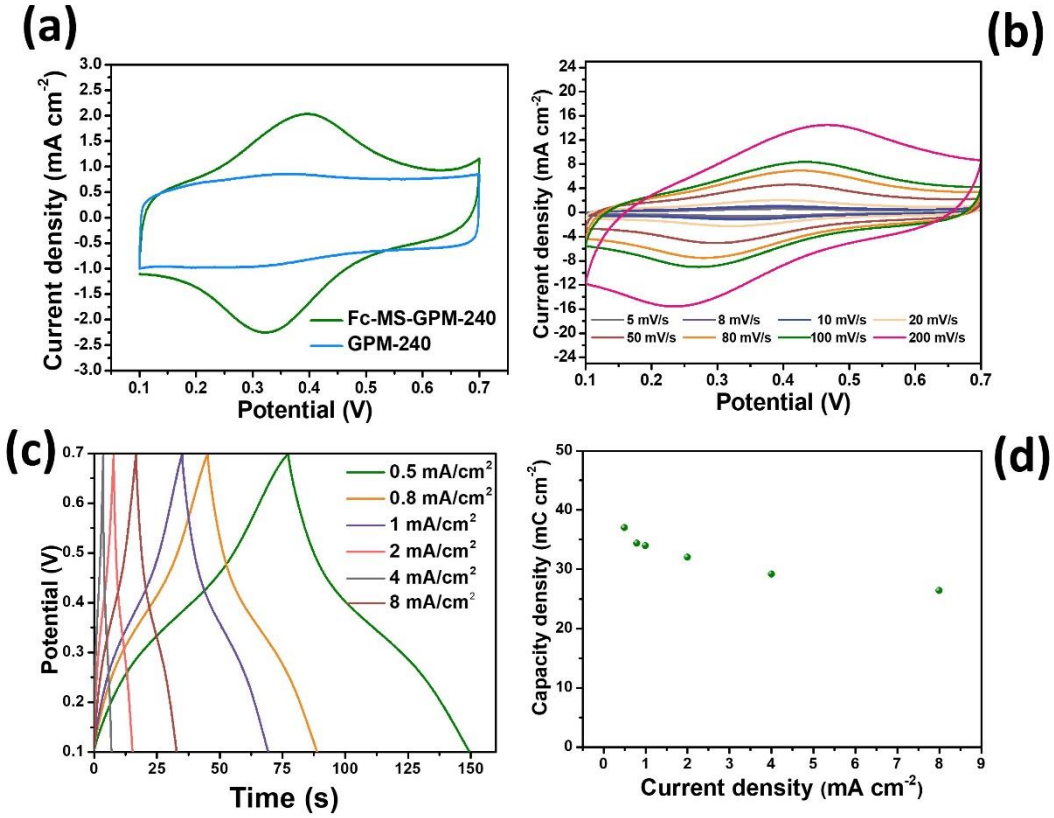

Figure 11. Energy storage performance of Fc-MS-GPM-240 in a three electrode system (vs. Ag/AgCl) with 1 M H_2SO_4 solution as the electrolyte. (a) the CV comparison between GPM-240 and Fc-Ms-GPM-240 at the scan rate of 20 mV s^{-1}; (b) the CV curves recorded at different scan rates ranging from 5 mV s^{-1} to 200 mV s^{-1}; (c) the galvanostatic charge-discharge curves with current densities from 0.5 mA cm^{-2} to 8 mA cm^{-2}; (d) the rate performance calculated from the galvanostatic charge-discharge curves.

The Fc-MS-GPM-240 also delivers a good cycling performance (**Figure 12**a), and its capacity only loss ca. 6% after 1,000 consecutive cycles at a scan rate of 200 mV s^{-1}. Except a little bit current decrease (the inset of **Figure 12**a), the shape of the CV curves does not change too much between the 1st and the 1000th cycles, indicative of its stable structure. Besides, the Fc-MS-GPM-240 is able to be multi-foldable and curvable, (**Figure 12**b) thanks to the flexibility of the scotch tape substrate.

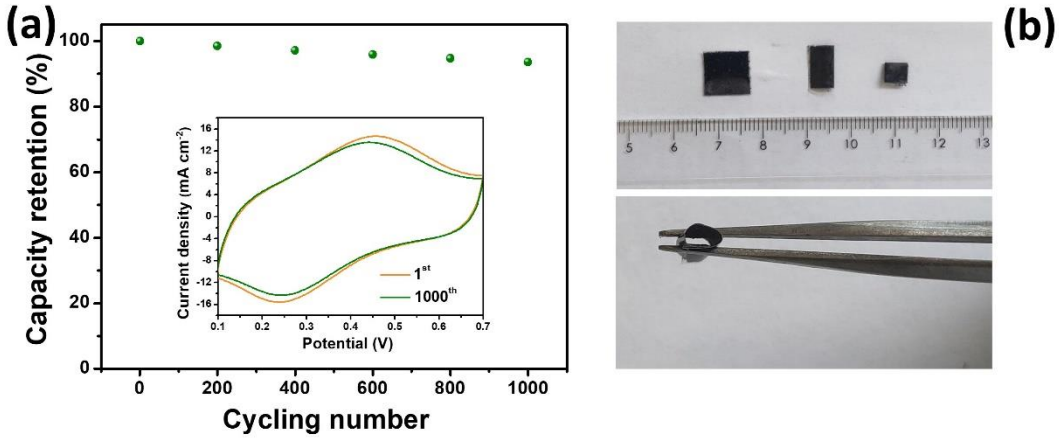

Figure 12. (a) Cycling performance of the Fc-MS-GPM-240 at a scan rate of 200 mV s^{-1}, and the inset is the CV curve for the 1st cycle and the 1000th cycle; (b) the digital photo to show the flexibility of the Fc-MS-GPM-240.

4.4 Conclusions

The strategy to prepare the planar micro-devices has been proposed by utilizing 3D-printed items to pattern the scotch tape, followed by a graphite transfer and electro-exfoliation process. (P.S. The 3D printing assisted pattern process has not been done yet due to the time limit, but the feasibility of this process is proved by a simple marker-pattern way.) Densely packed graphene layer (~110 μm) can be formed for the obtained GPMs electrodes, which exhibits a good energy storage performance in terms of the high capacity (24.5 mC cm^{-2} at the current density of 0.5 mA cm^{-2}) and good rate performance (81% capacity retention at the current density of 8 mA cm^{-2}). The flexible electron-hopping system has also been prepared by further generating the ferrocene functionalized silica film on the GPM-240, showing an obvious capacity enhancement (37 mC cm^{-2} at the current density of 0.5 mA cm^{-2}).

General Conclusions

A new type of silica-based energy storage materials operating with electron-hopping mechanism has been prepared by combining electrochemically-induced self-assembly method (EASA) and a copper-catalyzed azide-alkyne click (CuAAC) reaction. The redox active centers (ferrocene or cobaltocenium molecules) distributed on the surface of the silica film can directly commute electrons via the electron-hopping process. The results demonstrate this charge transfer mechanism is able to deliver a fast electron transfer rate even on the insulating silica substrate, resulting in a superior rate performance in comparison to the traditional faradic materials. The high density of redox molecules and the smooth counter ions diffusion pathway have been identified playing a pivotal role to ensure the fast electron-hopping process. Besides, the large-scale assembly of the electron-hopping system has been achieved by further generating the ferrocene functionalized silica film on a free-standing graphene foam electrode, exhibiting a 100-times higher capacity density, in comparison to that generating on ITO electrode, while maintaining the high rate performance. Finally, an attempt has been tried to assemble the graphene-supported ferrocene-functionalized silica into a flexible planar device, and the preliminary results has proved the feasibility of our proposed idea. Overall, in this thesis, the systematical study for the potential of the electron-hopping process in the energy storage field, which may pave a new way for the construction of energy storage materials.

Conclusions Générales

Un nouveau type de matériaux de stockage d'énergie à base de silice fonctionnant avec un mécanisme de saut d'électrons a été préparé en combinant une méthode d'auto-assemblage électrochimique (EASA) et une réaction de clic d'azide-alcyne catalysée par le cuivre (CuAAC). Les centres actifs redox (molécules de ferrocène ou de cobaltocénium) répartis à la surface du film de silice peuvent directement commuter les électrons par le biais du processus de saut d'électrons. Les résultats démontrent que ce mécanisme de transfert de charge est capable de fournir un taux de transfert d'électrons rapide même sur le substrat de silice isolant, ce qui se traduit par une performance de taux supérieure par rapport aux matériaux faradiques traditionnels. La haute densité des molécules redox et la voie de diffusion des contre-ions lisses ont été identifiées comme jouant un rôle essentiel pour assurer le processus de saut d'électrons rapide. En outre, l'assemblage à grande échelle du système de saut d'électrons a été réalisé en générant le film de silice fonctionnalisé au ferrocène sur une électrode autoportante en mousse de graphène, présentant une densité de capacité 100 fois plus élevée que celle générée sur une électrode ITO, tout en maintenant la performance de taux élevé. Enfin, une tentative a été faite pour assembler la silice fonctionnalisée au ferrocène sur un dispositif planaire flexible, et les résultats préliminaires ont prouvé la faisabilité de l'idée que nous proposons. Globalement, dans cette thèse, l'étude systématique du potentiel du processus de saut d'électrons dans le domaine du stockage de l'énergie, qui pourrait ouvrir une nouvelle voie pour la construction de matériaux de stockage de l'énergie.

High Lights

- This work first evaluates the potential of the electron-hopping as a promising charge transfer mechanism for the energy storage materials. The prepared silica-based materials operating with this mechanism show competitive energy storage performance.
- This work proves insulating nanostructured material can be also used for the energy storage applications, which breaks the stereotype, and widely broadens the choices of the electrode materials.
- This work particularly evaluates the energy storage value of the redox-molecules functionalized silica thin films prepared with the EASA method, achieving their feasibility demonstration, large-scale assembly, and the attempt to construct flexible planar devices, all of which solidly promote the development of such thin films.

Outlook

Beyond as the substrate to assemble the electron-hopping system for the energy storage device, such ordered, large-scale intact, and vertically aligned mesoporous silica thin film still holds great potential for the emerging applications that are currently facing insurmountable problems. Here, just give a few probably feasible cases to show the advantages of this silica thin film.

Case I

Acting As Artificial Interfaces for Homogeneous Metal Deposition

The metallic alkali metals are regarded as ideal anode materials in battery systems due to the step-change theoretical-specific capacity (Li: 3,860 mA h g^{-1}, Na: 1,166 mA h g^{-1}, Zn: 820 mAh g^{-1}) and low redox potential (Li:-3.040 V, Na:-2.714 V, Zn:-0.76 V *vs.* the standard hydrogen electrode). However, the alkali metal anode encounters great challenges in practical use due to its short lifespan and easily short-circuit problems.[212] One of main reasons causing these problems is the formation of hundreds microns of metal dendrites/protrusions due to the uneven metal electro-stripping/plating process. The surface-formed dendrites could possibly be peeled off from the anode into the electrolyte during the striping process, resulting in the loss of active materials, or continuously grow across the separator membrane to touch the cathode, inducing short-circuit.[213] We speculate the pre-coating of such vertically aligned mesoporous silica thin film on no matter metal plates or host materials could probably alleviate this dendrites problem. Taking the zinc metal anode for an example, the 2D diffusion of zinc ions could lead to inhomogeneous formation of the zinc seeds in the early nucleation stage.[214] Compared with the zinc plane, these as-formed seeds would preferentially grow in the following electrodeposition process due to their favorable surface energy, and finally result in the formation of dendrites. The illustration of this process is depicted in **Figure** 1.

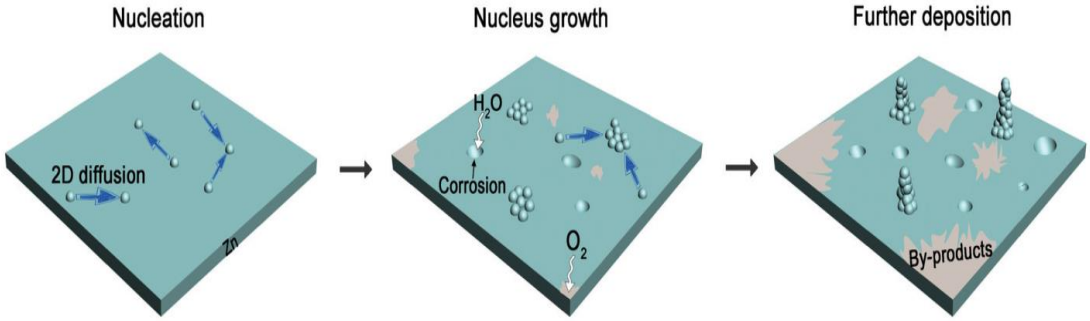

Figure 1 the illustration of the formation process of zinc dendrites. [214]

The interfacial modification of zinc plates or host materials with a thin layer of insulating materials, such as TiO_2[215], $CaCO_3$[212] etc., has been proved an efficient strategy to prevent the zinc dendrites formation, as the existence of such insulating layer may redirect the zinc ions diffusion and spatially confine the growth of dendrites during the stripping/plating process. However, coating an additional layer may also bring about the increase of zinc ions diffusion resistance to access to the underlying conductive layer, leading to a deteriorative rate performance.[215] As such, we propose the vertically aligned mesoporous silica thin film may properly function the metal ions plating/stripping processes. In the nucleation stage, the vertically aligned channels of the film could divide the whole zinc surface into numerous isolated nano-reactors, where the 2D planar zinc ions diffusion is blocked by the vertical silica walls. As a result, instead of the generating a small number of relative big zinc seeds, a mass of zinc seeds could be probably produced inside the mesochannels (2-3 nm). In the further zinc metal growth stage, the numerous zinc seeds could largely increase the active zinc deposition sites, achieving homogeneous zinc stripping/plating. Besides, the uniform vertical channels of such thin silica film (thickness ranging from 75 nm to 300 nm) also permit a fast ions diffusion process, proved by our previous results[92], and therefore could deliver a good rate performance.

Case II

Assisting Assembly of Azobenzene Derivatives for Photon Energy Storage

Solar energy harvesting and conversion into other forms of energy (i.e. electricity, chemical fuels, and heat) have been a focus of research efforts for efficient and renewable energy utilization.[216] Azobenzene and its derivatives are one of the most

important photon-energy storage materials due to their low cost, facile synthesis, and remarkable chemical stability.[217] They can isomerize to metastable forms (Cis-form) upon filtered solar irradiation, store photon energy in the strained chemical bonds, and release the stored energy as heat upon reverse isomerization (Trans-form), ΔH=41.4 kJ mol^{-1} for pristine azobenzene, as shown in **Figure 2**.

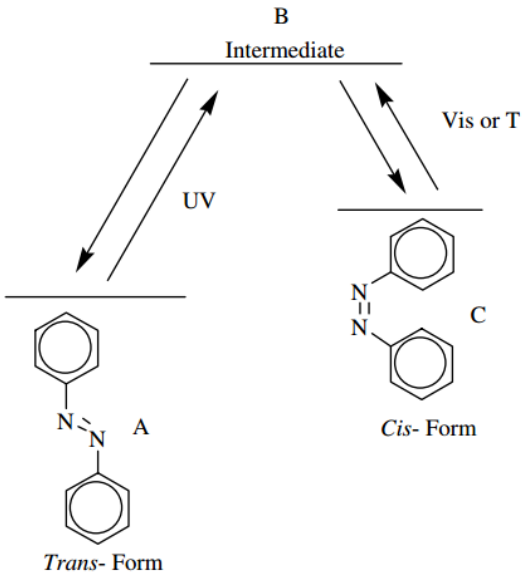

Figure 2. the illustration of form transition of azobenzene.

One of the bottleneck issues restricting their applications lies in how to further improve their energy densities.[217] Therefore, preparing hybrid photo-isomerization energy storage materials using nanoscale templates, such as carbon nanotube[218], and graphene[219], has been confirmed an effective mean to achieve this goal. Analogically, one can image the vertically-aligned mesochannels silica thin film could also have the similar functions as other nanoscale templates. First, the vertical mesochannels of the film could provide large surface and achieve ordered assembly of high density of azobenzene molecules. Besides, one definite advantage for this template, compared with chemical inert carbon-based materials, is its high chemical-activity, which can be easily introduced functional groups (azobenzene here) by either chemical modification of the silane used in the precursor solution or the utilization of the post-treatment techniques like click chemistry that we used for the grafting of ferrocene molecules in this thesis. Overall, the vertically aligned mesoporous silica film may hold potential in the field of photo-isomerization energy storage systems.

Case III

Acting as Transparent Template for Electrochromic Energy Storage Systems

Electrochromic devices that can reversibly change their optical properties via controlling voltage has attracted much attention because of its low-power consumption and broad fascinating applications, such as energy-efficient information displays, electronic labels, smart windows, switchable mirrors, and other cutting-edge applications.[220] Numerous electrochromic materials were developed in recent years including inorganic materials: WO_3, $W_{18}O_{49}$, and organic materials: Metallo-molecules, Polyaniline.[221–223] However, the exerting drags for these devices lie in how to achieve large-scale homogeneity, high coloration efficiency, fast switching speed, as well as robust electrochemical stability. The vertically-aligned mesoporous silica film could be an ideal template to assist assembly these electrochromic materials onto the electrode surface. First, the silica film can be easily and homogeneously generated on the surface of conductive electrodes including transparent ITO and FTO. The existence of this additional layer may help to achieve the even assembly of electrochromic materials in large-scale. Second, the large surface area of its vertically-aligned mesochannels would accommodate more electrochromic materials on the electrode surface, and the higher density of active materials would lead to a higher coloration efficiency. Third, it remains challenging to assemble the electrochromic materials in molecular level. Our previous results in this thesis have proved the electron-hopping based redox-molecular systems own a very fast redox reaction rate. Therefore, one can imagine it should be very interesting if we can modify the silica wall with some electrochromic metallo-molecules, like what we did with ferrocene molecules. These surface modified molecules could be fast reduced or oxidized, along with the color shifting, by the electron-hopping process and permit a fast speed of the color switch. Last but not the least, the silica film is highly transparent, and its Uv-Vis transmission spectrum is given in **Figure 3**. As we can see, the silica film gives the transparency over 72% across a wide wavelength from 320 nm to 700 nm. This means the existence of this silica film on the surface of electrode will not deteriorate the transparency of the pristine electrode too much, which is very important for the template of the electrochromic devices. Overall, this silica film with highly transparent nature and unique physiochemical properties probably hold a great potential in the electrochromic field.

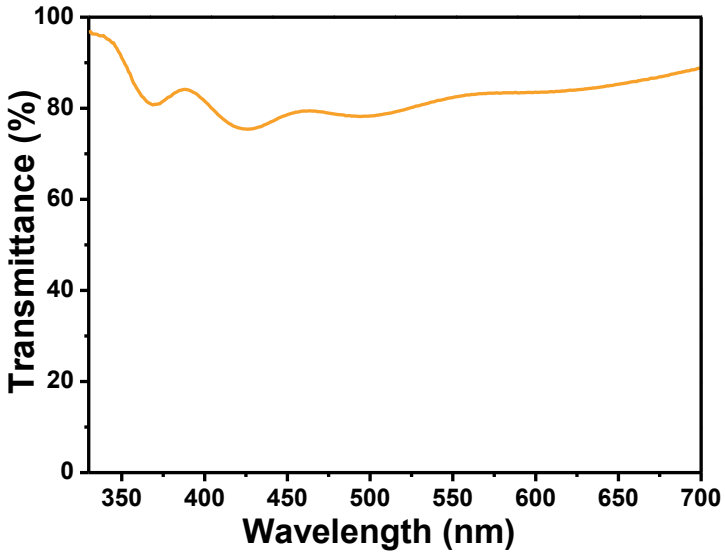

Figure 3. Uv-Vis transmission spectrum of the vertically aligned mesoporous silica film with wavenumbers ranging from 320 nm to 700 nm.

References

[1] N. Vilà, A. Walcarius, Electrochemical response of vertically-aligned, ferrocene-functionalized mesoporous silica films: Effect of the supporting electrolyte, Electrochim. Acta. 179 (2015) 304–314. doi:10.1016/j.electacta.2015.02.169.

[2] N. Vilà, E. André, R. Ciganda, J. Ruiz, D. Astruc, A. Walcarius, Molecular sieving with vertically aligned mesoporous silica films and electronic wiring through isolating nanochannels, Chem. Mater. 28 (2016) 2511–2514. doi:10.1021/acs.chemmater.6b00716.

[3] P. Simon, Y. Gogotsi, D. Bruce, Where do batteries end and supercapacitors begin ?, Science. 343 (2014) 1210–1211. doi:10.1126/science.1249625.

[4] Z. Lin, E. Goikolea, A. Balducci, K. Naoi, P.L. Taberna, M. Salanne, G. Yushin, P. Simon, Materials for supercapacitors: When Li-ion battery power is not enough, Mater. Today. 21 (2018) 419–436. doi:10.1016/j.mattod.2018.01.035.

[5] S. Chu, A. Majumdar, Opportunities and challenges for a sustainable energy future, Nature. 488 (2012) 294–303. doi:10.1038/nature11475.

[6] Z. Yang, J. Zhang, M.C.W. Kintner-Meyer, X. Lu, D. Choi, J.P. Lemmon, J. Liu, Electrochemical energy storage for green grid, Chem. Rev. 111 (2011) 3577–3613. doi:10.1021/cr100290v.

[7] Armand, Michel, J. Tarascon, Building better batteries, Nature. 451 (2008) 652–657.

[8] L. Negre, B. Daffos, V. Turq, P.L. Taberna, P. Simon, Ionogel-based solid-state supercapacitor operating over a wide range of temperature, Electrochim. Acta. 206 (2016) 490–495. doi:10.1016/j.electacta.2016.02.013.

[9] J. Yan, Q. Wang, T. Wei, Z. Fan, Recent advances in design and fabrication of electrochemical supercapacitors with high energy densities, Adv. Energy Mater. 4 (2014). doi:10.1002/aenm.201300816.

[10] B.E. Conway, Electrochemical Supercapacitors:Scientific Fundamentals and Technological Applications, Springer US, 1999.

[11] H. Helmholtz, Ueber einige Gesetze dcr Vertheilung elektrischer Strome in korperlichen Leitern, mit Anwendung auf die thierisch -elektrischen Versuche, Ann. Der Phys. Und Chemie. 165 (1853) 353–377. doi:10.1002/andp.18531650702.

[12] M. GOUY., De La Charge Électrique a La Surface D'Un Électrolyte, J.de Physs. (1910) 457–468.

[13] David Leonard Chapman, A contribution to the theory of electrocapillarity, Theor. Comput. Sci. 37 (1985) 151–181. doi:10.1016/0304-3975(85)90090-8.

[14] O. Stern, ZUR THEORIE DER ELEKTROLYTISCHEN DOPPELSCHICHT, Zeitschrift Fur Elektrochemie. 30 (1924) 508–516. doi:10.1002/bbpc.192400182.

[15] D.C. Grahame, The electrical double layer and the theory of electrocapillarity, Chem. Rev. 41 (1947) 441–501. doi:10.1021/cr60130a002.

[16] M.L. Heilig, F. Vischers, Low voltage electrolytic capaciotr, 1957. doi:10.1145/178951.178972.

[17] R.A. Rightmire, ELECTRICAL ENERGY STORAGE DEWICE AND METHOD OF STORING ELECTRICAL ENERGY, 1969. doi:10.1017/CBO9781107415324.004.

[18] Y. Shao, M.F. El-Kady, J. Sun, Y. Li, Q. Zhang, M. Zhu, H. Wang, B. Dunn, R.B. Kaner, Design and mechanisms of asymmetric supercapacitors, Chem. Rev. 118 (2018) 9233–9280. doi:10.1021/acs.chemrev.8b00252.

[19] B.E. Conway, Transition from "supercapacitor" to "battery" behavior in electrochemical energy storage, Proc. Int. Power Sources Symp. 138 (1991) 319–327. doi:10.1149/1.2085829.

[20] S. Trasatti, G. Buzzanca, Ruthenium dioxide: A new interesting electrode

material. Solid state structure and electrochemical behaviour, J. Electroanal. Chem. 29 (1971) 4–8. doi:10.1016/S0022-0728(71)80111-0.

[21] H.T. Fang, M. Liu, D.W. Wang, X.H. Ren, X. Sun, Fabrication and supercapacitive properties of a thick electrode of carbon nanotube-RuO_2 core-shell hybrid material with a high RuO_2 loading, Nano Energy. 2 (2013) 1232–1241. doi:10.1016/j.nanoen.2013.05.012.

[22] Y. Aiping, C. Victor, Z. Jiujun, Electrochemical Supercapacitors for Energy Storage and Delivery: Fundamentals and Applications, CRC Press, 2017.

[23] Y. Wang, Y. Song, Y. Xia, Electrochemical capacitors: Mechanism, materials, systems, characterization and applications, Chem. Soc. Rev. 45 (2016) 5925–5950. doi:10.1039/c5cs00580a.

[24] J.R. Miller, P. Simon, Materials science: Electrochemical capacitors for energy management, Science. 321 (2008) 651–652. doi:10.1126/science.1158736.

[25] Y. Gogotsi, What nano can do for energy storage, ACS Nano. 8 (2014) 5369–5371. doi:10.1021/nn503164x.

[26] M. Forghani, S.W. Donne, Method comparison for deconvoluting capacitive and pseudo-capacitive contributions to electrochemical capacitor electrode behavior, J. Electrochem. Soc. 165 (2018) A664–A673. doi:10.1149/2.0931803jes.

[27] E.L. Gyenge, J.-F. Drillet, The electrochemical behavior and catalytic activity for oxygen reduction of MnO_2/C– toray gas diffusion electrodes , J. Electrochem. Soc. 159 (2011) F23–F34. doi:10.1149/2.061202jes.

[28] D. Qu, H. Shi, Studies of activated carbons used in double-layer capacitors, J. Power Sources. 74 (1998) 99–107.

[29] J. Gamby, P.L. Taberna, P. Simon, J.F. Fauvarque, M. Chesneau, Studies and characterisations of various activated carbons used for carbon/carbon supercapacitors, J. Power Sources. 101 (2001) 109–116. doi:10.1016/S0378-

7753(01)00707-8.

[30] Z.S. Wu, A. Winter, L. Chen, Y. Sun, A. Turchanin, X. Feng, K. Müllen, Three-dimensional nitrogen and boron co-doped graphene for high-performance all-solid-state supercapacitors, Adv. Mater. 24 (2012) 5130–5135. doi:10.1002/adma.201201948.

[31] M. Kaempgen, C.K. Chan, J. Ma, Y. Cui, G. Gruner, Printable thin film supercapacitors using single-walled carbon nanotubes, Nano Lett. 9 (2009) 1872–1876. doi:10.1021/nl8038579.

[32] C. Yu, C. Masarapu, J. Rong, B.Q.M. Wei, H. Jiang, Stretchable supercapacitors based on buckled single-walled carbon nanotube macrofilms, Adv. Mater. 21 (2009) 4793–4797. doi:10.1002/adma.200901775.

[33] R. Raccichini, A. Varzi, S. Passerini, B. Scrosati, The role of graphene for electrochemical energy storage, Nat. Mater. 14 (2015) 271–279. doi:10.1038/nmat4170.

[34] Y. Wang, Z. Shi, Y. Huang, Y. Ma, C. Wang, M. Chen, Y. Chen, Supercapacitor devices based on graphene materials, J. Phys. Chem. C Phys. Chem. C. 113 (2009) 13103–13107.

[35] A.G. Pandolfo, A.F. Hollenkamp, Carbon properties and their role in supercapacitors, J. Power Sources. 157 (2006) 11–27. doi:10.1016/j.jpowsour.2006.02.065.

[36] J. Xia, F. Chen, J. Li, N. Tao, Measurement of the quantum capacitance of graphene, Nat. Nanotechnol. 4 (2009) 505–509. doi:10.1038/nnano.2009.177.

[37] M.D. Stoller, C.W. Magnuson, Y. Zhu, S. Murali, J.W. Suk, R. Piner, R.S. Ruoff, Interfacial capacitance of single layer graphene, Energy Environ. Sci. 4 (2011) 4685–4689. doi:10.1039/c1ee02322e.

[38] M.F. El-Kady, V. Strong, S. Dubin, R.B. Kaner, Laser scribing of high-

performance and flexible graphene-based electrochemical capacitors, Science. 335 (2012) 1326–1330. doi:10.1126/science.1216744.

[39] L.L. Zhang, X.S. Zhao, Carbon-based materials as supercapacitor electrodes, Chem. Soc. Rev. 38 (2009) 2520–2531. doi:10.1039/b813846j.

[40] R. Kotz, M. Carlen, Principles and applications of electrochemical capacitors, Electrochim. Acta. 45 (2000) 2483–2498. doi:10.1057/9780230503014.

[41] Y. Gogotsi, R.M. Penner, Energy storage in nanomaterials - capacitive, pseudocapacitive, or battery-like?, ACS Nano. 12 (2018) 2081–2083. doi:10.1021/acsnano.8b01914.

[42] V. Augustyn, P. Simon, B. Dunn, Pseudocapacitive oxide materials for high-rate electrochemical energy storage, Energy Environ. Sci. 7 (2014) 1597–1614. doi:10.1039/c3ee44164d.

[43] S. Huang, J. Sun, J. Yan, J. Liu, W. Wang, Q. Qin, W. Mao, W. Xu, Y. Wu, J. Wang, Enhanced high-temperature cyclic stability of Al-doped manganese dioxide and morphology evolution study through in situ NMR under high magnetic field, ACS Appl. Mater. Interfaces. 10 (2018) 9398–9406. doi:10.1021/acsami.7b18762.

[44] M. Toupin, T. Brousse, D. Bélanger, Charge storage mechanism of MnO_2 electrode used in aqueous electrochemical capacitor, Chem. Mater. 16 (2004) 3184–3190. doi:10.1021/cm049649j.

[45] W. Sugimoto, H. Iwata, K. Yokoshima, Y. Murakami, Y. Takasu, Proton and electron conductivity in hydrous ruthenium oxides evaluated by electrochemical impedance spectroscopy: The origin of large capacitance, J. Phys. Chem. B. 109 (2005) 7330–7338. doi:10.1021/jp044252o.

[46] M. Mastragostino, C. Arbizzani, F. Soavi, Polymer-based supercapacitors, 98 (2001) 812–815.

[47] D. Chen, J.H. Wang, T.F. Chou, B. Zhao, M.A. El-Sayed, M. Liu, Unraveling the nature of anomalously fast energy storage in T-Nb_2O_5, J. Am. Chem. Soc. 139 (2017) 7071–7081. doi:10.1021/jacs.7b03141.

[48] J.W. Kim, V. Augustyn, B. Dunn, The effect of crystallinity on the rapid pseudocapacitive response of Nb_2O_5, Adv. Energy Mater. 2 (2012) 141–148. doi:10.1002/aenm.201100494.

[49] T. Brousse, D. Bélanger, J.W. Long, To be or not to be pseudocapacitive?, J. Electrochem. Soc. 162 (2015) A5185–A5189. doi:10.1149/2.0201505jes.

[50] Lindstrom Henrik, S. So, A. Solbrand, J. Hjelm, A. Hagfeldt, S. Lindquist, Li ion insertion in TiO_2(Anatase), voltammetry on nanoporous films, J. Phys. Chem. B. 2 (1997) 7717–7722.

[51] J. Wang, J. Polleux, J. Lim, B. Dunn, Pseudocapacitive contributions to electrochemical energy storage in TiO_2 (anatase) nanoparticles, J. Phys. Chem. C. 111 (2007) 14925–14931. doi:10.1021/jp074464w.

[52] S. Zhou, S. Wang, S. Zhou, H. Xu, J. Zhao, J. Wang, Y. Li, An electrochromic supercapacitor based on MOF derived hierarchical-porous NiO feilm, Nanoscale. (2020). doi:10.1039/d0nr01152e.

[53] P. Cai, T. Liu, L. Zhang, B. Cheng, J. Yu, ZIF-67 derived nickel cobalt sulfide hollow cages for high-performance supercapacitors, Appl. Surf. Sci. 504 (2020) 144501. doi:10.1016/j.apsusc.2019.144501.

[54] S.A. Ansari, N.A. Khan, Z. Hasan, A.A. Shaikh, F.K. Ferdousi, H.R. Barai, N.S. Lopa, M.M. Rahman, Electrochemical synthesis of titanium nitride nanoparticles onto titanium foil for electrochemical supercapacitors with ultrafast charge/discharge, Sustain. Energy Fuels. (2020). doi:10.1039/d0se00049c.

[55] J. Kang, A. Hirata, L. Kang, X. Zhang, Y. Hou, L. Chen, C. Li, T. Fujita, K. Akagi, M. Chen, Enhanced supercapacitor performance of MnO_2 by atomic doping, Angew. Chemie - Int. Ed. 52 (2013) 1664–1667.

doi:10.1002/anie.201208993.

[56] A.M. Elshahawy, C. Guan, X. Li, H. Zhang, Y. Hu, H. Wu, S.J. Pennycook, J. Wang, Sulfur-doped cobalt phosphide nanotube arrays for highly stable hybrid supercapacitor, Nano Energy. 39 (2017) 162–171. doi:10.1016/j.nanoen.2017.06.042.

[57] T. Xing, Y. Ouyang, Y. Chen, L. Zheng, C. Wu, X. Wang, P-doped ternary transition metal oxide as electrode material of asymmetric supercapacitor, J. Energy Storage. 28 (2020) 101248. doi:10.1016/j.est.2020.101248.

[58] H.K. Jung, S.J. Lee, D. Han, A.R. Hong, H.S. Jang, S.H. Lee, J.H. Mun, H.J. Lee, S.H. Han, D. Yang, D.H. Kim, Au-incorporated NiO nanocomposite thin films as electrochromic electrodes for supercapacitors, Electrochim. Acta. 330 (2020) 135203. doi:10.1016/j.electacta.2019.135203.

[59] Y. Wang, Y.Z. Zhang, Y.Q. Gao, G. Sheng, J.E. ten Elshof, Defect engineering of MnO_2 nanosheets by substitutional doping for printable solid-state micro-supercapacitors, Nano Energy. 68 (2020) 104306. doi:10.1016/j.nanoen.2019.104306.

[60] G. Xiong, P. He, D. Wang, Q. Zhang, T. Chen, T.S. Fisher, Hierarchical Ni – Co hydroxide petals on mechanically robust graphene petal foam for high-energy asymmetric supercapacitors, (2016) 5460–5470. doi:10.1002/adfm.201600879.

[61] M.R. Lukatskaya, S. Kota, Z. Lin, M.Q. Zhao, N. Shpigel, M.D. Levi, J. Halim, P.L. Taberna, M.W. Barsoum, P. Simon, Y. Gogotsi, Ultra-high-rate pseudocapacitive energy storage in two-dimensional transition metal carbides, Nat. Energy. 6 (2017) 1–6. doi:10.1038/nenergy.2017.105.

[62] D.M. MacArthur, The proton diffusion coefficient for the nickel hydroxide electrode, J. Electrochem. Soc. 117 (1970) 729. doi:10.1149/1.2407618.

[63] A.M. Friedman, J.W. Kennedy, The self-diffusion coefficients of potassium, cesium, iodide and chloride ions in aqueous solutions, J. Am. Chem. Soc. 77

(1955) 4499–4501. doi:10.1021/ja01622a016.

[64] S. Cong, Y. Tian, Q. Li, Z. Zhao, F. Geng, Single-crystalline tungsten oxide quantum dots for fast pseudocapacitor and electrochromic applications, Adv. Mater. 26 (2014) 4260–4267. doi:10.1002/adma.201400447.

[65] D.J. Gibbons, W.E. Spear, Electron hopping transport and trapping phenomena in orthorhombic sulphur crystals, J. Phys. Chem. Solids. 27 (1966) 1917–1925. doi:10.1016/0022-3697(66)90122-3.

[66] A.L. Eckermann, D.J. Feld, J.A. Shaw, T.J. Meade, Electrochemistry of redox-active self-assembled monolayers, Coord. Chem. Rev. 254 (2010) 1769–1802. doi:10.1016/j.ccr.2009.12.023.

[67] C. Orneias, J. Ruiz, C. Belin, D. Astruc, Giant dendritic molecular electrochrome batteries with ferrocenyl and pentamethylferrocenyl termini, J. Am. Chem. Soc. 131 (2009) 590–601. doi:10.1021/ja8062343.

[68] D. Astruc, Electron-transfer processes in dendrimers and their implication in biology, catalysis, sensing and nanotechnology, Nat. Chem. 4 (2012) 255–267. doi:10.1038/nchem.1304.

[69] C. Amatore, E. Maisonhaute, B. Schöllhorn, J. Wadhawan, Ultrafast voltammetry for probing interfacial electron transfer in molecular wires, ChemPhysChem. 8 (2007) 1321–1329. doi:10.1002/cphc.200600774.

[70] C. T. Kresge, M. E. Leonowicz, W. J. Roth, J. C. Vartuli, J. S. Beck, Ordered mesoporous molecular sieves synthesized by a liquid-crystal template mechanism, Nature. 359 (1992) 710–712.

[71] Y. Wan, Y. Shi, D. Zhao, Designed synthesis of mesoporous solids via nonionic-surfactant-templating approach, Chem. Commun. (2007) 897–926. doi:10.1039/b610570j.

[72] D. Zhao, J. Feng, Q. Huo, N. Melosh, G.H. Fredrickson, B.F. Chmelka, G.D.

Stucky, Triblock copolymer syntheses of mesoporous silica with periodic 50 to 300 angstrom pores, Science. 279 (1998) 548–552.

[73] D. Zhao, Q. Huo, J. Feng, B.F. Chmelka, G.D. Stucky, Nonionic triblock and star diblock copolymer and oligomeric sufactant syntheses of highly ordered, hydrothermally stable, mesoporous silica structures, J. Am. Chem. Soc. 120 (1998) 6024–6036. doi:10.1021/ja974025i.

[74] C. Yu, Y. Yu, D. Zhao, Highly ordered large caged cubic mesoporous silica structures templated by triblock PEO-PBO-PEO copolymer, Chem. Commun. (2000) 575–576. doi:10.1039/b000603n.

[75] S. Shen, Y. Li, Z. Zhang, J. Fan, B. Tu, W. Zhou, D. Zhao, A novel ordered cubic mesoporous silica templated with tri-head group quaternary ammonium surfactant, Chem. Commun. 2 (2002) 2212–2213. doi:10.1039/b206993h.

[76] S.S. Kim, T.R. Pauly, T.J. Pinnavaia, Non-ionic surfactant assembly of wormhole silica molecular sieves from water soluble silicates, Chem. Commun. (2000) 835–836. doi:10.1039/b001012j.

[77] P.T. Tanev, Y. Liang, T.J. Pinnavaia, Assembly of mesoporous lamelar silicas with hierarchical particle architectures, J. Am. Chem. Soc. 119 (1997) 8616–8624. doi:10.1021/ja970228v.

[78] R. Ryoo, J.M. Kim, C.H. Ko, C.H. Shin, Disordered molecular sieve with branched mesoporous channel network, J. Phys. Chem. 100 (1996) 17718–17721. doi:10.1021/jp9620835.

[79] C. Pak, G.L. Haller, Preparation of vanadium- and chromium-substituted KIT-1 disordered mesoporous materials by direct incorporation, Microporous Mesoporous Mater. 44–45 (2001) 321–326. doi:10.1016/S1387-1811(01)00198-6.

[80] E. Da'na, Adsorption of heavy metals on functionalized-mesoporous silica: A review, Microporous Mesoporous Mater. 247 (2017) 145–157.

doi:10.1016/j.micromeso.2017.03.050.

[81] B. Yao, S. Mandrà, J.O. Curry, S. Shaikhutdinov, H.J. Freund, J. Schrier, Gas Separation through Bilayer Silica, the Thinnest Possible Silica Membrane, ACS Appl. Mater. Interfaces. 9 (2017) 43061–43071. doi:10.1021/acsami.7b13302.

[82] J. Liang, Z. Liang, R. Zou, Y. Zhao, Heterogeneous Catalysis in Zeolites, Mesoporous Silica, and Metal–Organic Frameworks, Adv. Mater. 29 (2017) 1–21. doi:10.1002/adma.201701139.

[83] C.T. Wang, C.L. Wu, I.C. Chen, Y.H. Huang, Humidity sensors based on silica nanoparticle aerogel thin films, Sensors Actuators, B Chem. 107 (2005) 402–410. doi:10.1016/j.snb.2004.10.034.

[84] A. Rahikkala, S.A.P. Pereira, P. Figueiredo, M.L.C. Passos, A.R.T.S. Araújo, M.L.M.F.S. Saraiva, H.A. Santos, Mesoporous Silica Nanoparticles for Targeted and Stimuli-Responsive Delivery of Chemotherapeutics: A Review, Adv. Biosyst. 2 (2018) 1–33. doi:10.1002/adbi.201800020.

[85] A. Fihri, D. Abdullatif, H. Bin Saad, R. Mahfouz, H. Al-Baidary, M. Bouhrara, Decorated fibrous silica epoxy coating exhibiting anti-corrosion properties, Prog. Org. Coatings. 127 (2019) 110–116. doi:10.1016/j.porgcoat.2018.09.025.

[86] F. Nador, E. Guisasola, A. Baeza, M.A.M. Villaecija, M. Vallet-Regí, D. Ruiz-Molina, Synthesis of polydopamine-like nanocapsules via removal of a sacrificial mesoporous silica template with water, Chem. - A Eur. J. 23 (2017) 2753–2758. doi:10.1002/chem.201604631.

[87] H. Yang, N. Coombs, I. Sokolov, G.A. Ozin, Free-standing and oriented mesoporous silica films grown at the air-water interface, Nature. 381 (1996) 589–592. doi:10.1038/381589a0.

[88] H. Yang, A. Kuperman, N. Coombs, S. Mamiche-Afara, G.A. Ozin, Synthesis of oriented films of mesoporous silica on mica, Nature. 379 (1996) 703–705. doi:10.1038/379703a0.

[89] F. Schacht, S; Huo, Q; Voigt-Martin, I G; Stucky, G D; Schuth, Oil-water interface templating of mesoporous macroscale structures, Science. 273 (1996) 768.

[90] L. Nicole, C. Boissière, D. Grosso, A. Quach, C. Sanchez, Mesostructured hybrid organic-inorganic thin films, J. Mater. Chem. 15 (2005) 3598–3627. doi:10.1039/b506072a.

[91] C.J. Brinker, Y. Lu, Alan Sellinger, and H. Fan, Evaporation-induced self-assembly: Functional nanostructures made easy, Adv. Mater. 11 (1999) 579–585. doi:10.1557/mrs2004.183.

[92] A. Goux, M. Etienne, E. Aubert, C. Lecomte, J. Ghanbaja, A. Walcarius, Oriented mesoporous silica films obtained by electro-assisted self-assembly (EASA), Chem. Mater. 21 (2009) 731–741. doi:10.1021/cm8029664.

[93] A. Walcarius, E. Sibottier, M. Etienne, J. Ghanbaja, Electrochemically assisted self-assembly of mesoporous silica thin films, Nat. Mater. 6 (2007) 602–608. doi:10.1038/nmat1951.

[94] N. Vilà, J. Ghanbaja, E. Aubert, A. Walcarius, Electrochemically assisted generation of highly ordered azide-functionalized mesoporous silica for oriented hybrid films, Angew. Chemie - Int. Ed. 53 (2014) 2945–2950. doi:10.1002/anie.201309447.

[95] M. Abboud, R. Bel-Hadj-Tahar, N. Fakhri, A. Sayari, Synthesis of ferrocenylazobenzene-functionalized MCM-41 via direct co-condensation method, Microporous Mesoporous Mater. 265 (2018) 179–184. doi:10.1016/j.micromeso.2018.02.013.

[96] H. Nandivada, X. Jiang, J. Lahann, Click chemistry: Versatility and control in the hands of materials scientists, Adv. Mater. 19 (2007) 2197–2208. doi:10.1002/adma.200602739.

[97] A. Schlossbauer, D. Schaffert, J. Kecht, E. Wagner, T. Bein, Click chemistry for

high-density biofunctionalization of mesoporous silica, J. Am. Chem. Soc. 130 (2008) 12558–12559. doi:10.1021/ja803018w.

[98] C. Karman, N. Vilà, A. Walcarius, Amplified charge transfer for anionic redox probes through oriented mesoporous silica thin films, ChemElectroChem. 3 (2016) 2130–2137. doi:10.1002/celc.201600303.

[99] T. Nasir, G. Herzog, M. Hébrant, C. Despas, L. Liu, A. Walcarius, Mesoporous Silica Thin Films for Improved Electrochemical Detection of Paraquat, ACS Sensors. 3 (2018) 484–493. doi:10.1021/acssensors.7b00920.

[100] P. Simon, Y. Gogotsi, Materials for electrochemical capacitors, Nat. Mater. 7 (2008) 845–854. doi:10.1142/9789814317665_0021.

[101] Z. Yu, L. Tetard, L. Zhai, J. Thomas, Supercapacitor electrode materials: Nanostructures from 0 to 3 dimensions, Energy Environ. Sci. 8 (2015) 702–730. doi:10.1039/c4ee03229b.

[102] Y. Liu, X. Peng, Recent advances of supercapacitors based on two-dimensional materials, Appl. Mater. Today. 8 (2017) 104–115. doi:10.1016/j.apmt.2017.05.002.

[103] X. Shi, S. Zheng, Z.S. Wu, X. Bao, Recent advances of graphene-based materials for high-performance and new-concept supercapacitors, J. Energy Chem. 27 (2018) 25–42. doi:10.1016/j.jechem.2017.09.034.

[104] D.S. Achilleos, T.A. Hatton, Surface design and engineering of hierarchical hybrid nanostructures for asymmetric supercapacitors with improved electrochemical performance, J. Colloid Interface Sci. 447 (2015) 282–301. doi:10.1016/j.jcis.2014.12.080.

[105] J. Wang, S. Dong, B. Ding, Y. Wang, X. Hao, H. Dou, Y. Xia, X. Zhang, Pseudocapacitive materials for electrochemical capacitors: From rational synthesis to capacitance optimization, Natl. Sci. Rev. 4 (2017) 71–90. doi:10.1093/nsr/nww072.

[106] M.M. Sk, C.Y. Yue, K. Ghosh, R.K. Jena, Review on advances in porous nanostructured nickel oxides and their composite electrodes for high-performance supercapacitors, J. Power Sources. 308 (2016) 121–140. doi:10.1016/j.jpowsour.2016.01.056.

[107] Y. Liu, Z. Wang, Y. Zhong, M. Tade, W. Zhou, Z. Shao, Molecular design of mesoporous $NiCo_2O_4$ and $NiCo_2S_4$ with sub-micrometer-polyhedron architectures for efficient pseudocapacitive energy storage, Adv. Funct. Mater. 27 (2017) 1701229–1701239. doi:10.1002/adfm.201701229.

[108] Q. Meng, K. Cai, Y. Chen, L. Chen, Research progress on conducting polymer based supercapacitor electrode materials, Nano Energy. 36 (2017) 268–285. doi:10.1016/j.nanoen.2017.04.040.

[109] W. Zuo, R. Li, C. Zhou, Y. Li, J. Xia, J. Liu, Battery-supercapacitor hybrid devices: recent progress and future prospects, Adv. Sci. 4 (2017) 1600539–1600560. doi:10.1002/advs.201600539.

[110] A. Muzaffar, M.B. Ahamed, K. Deshmukh, J. Thirumalai, A review on recent advances in hybrid supercapacitors: Design, fabrication and applications, Renew. Sustain. Energy Rev. 101 (2019) 123–145. doi:10.1016/j.rser.2018.10.026.

[111] D.G. Wang, Z. Liang, S. Gao, C. Qu, R. Zou, Metal-organic framework-based materials for hybrid supercapacitor application, Coord. Chem. Rev. 404 (2020) 213093. doi:10.1016/j.ccr.2019.213093.

[112] D.N. Blauch, J.M. Savéant, Effects of long-range electron transfer on charge transport in static assemblies of redox centers, J. Phys. Chem. 97 (1993) 6444–6448. doi:10.1021/j100126a019.

[113] H.O. Finklea, D.D. Hanshew, Electron-Transfer Kinetics in Organized Thiol Monolayers with Attached Pentaammine(pyridine)ruthenium Redox Centers, J. Am. Chem. Soc. 114 (1992) 3173–3181. doi:10.1021/ja00035a001.

[114] K. Sato, R. Ichinoi, R. Mizukami, T. Serikawa, Y. Sasaki, J. Lutkenhaus, H.

Nishide, K. Oyaizu, Diffusion-cooperative model for charge transport by redox-active nonconjugated polymers, J. Am. Chem. Soc. 140 (2018) 1049–1056. doi:10.1021/jacs.7b11272.

[115] N. Vilà, J. Ghanbaja, E. Aubert, A. Walcarius, Electrochemically assisted generation of highly ordered azide-functionalized mesoporous silica for oriented hybrid films, Angew. Chemie - Int. Ed. 53 (2014) 2945–2950. doi:10.1002/anie.201309447.

[116] N. Vilà, J. Ghanbaja, A. Walcarius, Clickable bifunctional and vertically aligned mesoporous silica films, Adv. Mater. Interfaces. 3 (2016) 1500440–1500451. doi:10.1002/admi.201500440.

[117] P. Yadav, S. Chacko, G. Kumar, R. Ramapanicker, V. Verma, Click chemistry route to covalently link cellulose and clay, Cellulose. 22 (2015) 1615–1624. doi:10.1007/s10570-015-0594-2.

[118] M. Wildschek, C. Rieker, P. Jaitner, H. Schottenberger, K. Eberhard Schwarzhans, Ethynylcobaltocenium compounds as precursors for bridged, heteronuclear oligometallocenes: Preparation and reactions of ethynyl-, trimethylsilylethynyl- and ferrocenylethynylcobaltocenium salts, J. Organomet. Chem. 396 (1990) 355–361. doi:10.1016/0022-328X(90)85476-F.

[119] W.S. Hummers, R.E. Offeman, Preparation of Graphitic Oxide, J. Am. Chem. Soc. 80 (1958) 1339. doi:10.1021/ja01539a017.

[120] W. Xu, Z. Jiang, Q. Yang, W. Huo, M.S. Javed, Y. Li, L. Huang, X. Gu, C. Hu, Approaching the lithium-manganese oxides' energy storage limit with Li_2MnO_3 nanorods for high-performance supercapacitor, Nano Energy. 43 (2018) 168–176. doi:10.1016/j.nanoen.2017.10.046.

[121] Y. Guillemin, M. Etienne, E. Aubert, A. Walcarius, Electrogeneration of highly methylated mesoporous silica thin films with vertically-aligned mesochannels and electrochemical monitoring of mass transport issues, J. Mater. Chem. 20

(2010) 6799–6807. doi:10.1039/c0jm00305k.

[122] A. Gamero-Quijano, C. Karman, N. Vilà, G. Herzog, A. Walcarius, Vertically aligned and ordered one-dimensional mesoscale polyaniline, Langmuir. 33 (2017) 4224–4234. doi:10.1021/acs.langmuir.7b00892.

[123] I. Kovačević, B. Pivac, P. Dubček, N. Radić, S. Bernstorff, A. Slaoui, A GISAXS study of SiO/SiO_2 superlattice, Thin Solid Films. 511–512 (2006) 463–467. doi:10.1016/j.tsf.2005.12.028.

[124] M.H. Lim, A. Stein, Comparative studies of grafting and direct syntheses of inorganic-organic hybrid mesoporous materials, Chem. Mater. 11 (1999) 3285–3295. doi:10.1021/cm990369r.

[125] C. Richard G, B. Craig E, Understanding Voltammetry, Imperial College Press, London, 2013.

[126] Y. Jiang, J. Liu, Definitions of pseudocapacitive materials: a brief review, Energy Environ. Mater. 2 (2019) 30–37. doi:10.1002/eem2.12028.

[127] T.M. Higgins, J.N. Coleman, Avoiding resistance limitations in high-performance transparent supercapacitor electrodes based on large-area, high-conductivity PEDOT:PSS films, ACS Appl. Mater. Interfaces. 7 (2015) 16495–16506. doi:10.1021/acsami.5b03882.

[128] C. (John) Zhang, T.M. Higgins, S.H. Park, S.E. O'Brien, D. Long, J.N. Coleman, V. Nicolosi, Highly flexible and transparent solid-state supercapacitors based on RuO_2/PEDOT:PSS conductive ultrathin films, Nano Energy. 28 (2016) 495–505. doi:10.1016/j.nanoen.2016.08.052.

[129] P.J. King, T.M. Higgins, S. De, N. Nicoloso, J.N. Coleman, Percolation effects in supercapacitors with thin, transparent carbon nanotube electrodes, ACS Nano. 6 (2012) 1732–1741. doi:10.1021/nn204734t.

[130] T. Chen, Y. Xue, A.K. Roy, L. Dai, Transparent and stretchable high-

performance supercapacitors based on wrinkled graphene electrodes, ACS Nano. 8 (2014) 1039–1046. doi:10.1021/nn405939w.

[131] L. Song, X. Cao, L. Li, Q. Wang, H. Ye, L. Gu, C. Mao, J. Song, S. Zhang, H. Niu, General method for large-area films of carbon nanomaterials and application of a self-assembled carbon nanotube film as a high-performance electrode material for an all-solid-state supercapacitor, Adv. Funct. Mater. 27 (2017) 1700474–1700487. doi:10.1002/adfm.201700474.

[132] H.R. Byon, S.W. Lee, S. Chen, P.T. Hammond, Y. Shao-Horn, Thin films of carbon nanotubes and chemically reduced graphenes for electrochemical micro-capacitors, Carbon N. Y. 49 (2011) 457–467. doi:10.1016/j.carbon.2010.09.042.

[133] J.H. Anderson, G.A. Parks, The electrical conductivity of silica gel in the presence of adsorbed water, J. Phys. Chem. 72 (1968) 3662–3668. doi:10.1021/j100856a051.

[134] W. Tian, H. Hu, Y. Wang, P. Li, J. Liu, J. Liu, X. Wang, X. Xu, Z. Li, Q. Zhao, H. Ning, W. Wu, M. Wu, Metal-organic frameworks mediated synthesis of one-dimensional molybdenum-based/carbon composites for enhanced lithium storage, ACS Nano. 12 (2018) 1990–2000. doi:10.1021/acsnano.7b09175.

[135] C.J. Zhang, B. Anasori, A. Seral-Ascaso, S.H. Park, N. McEvoy, A. Shmeliov, G.S. Duesberg, J.N. Coleman, Y. Gogotsi, V. Nicolosi, Transparent, Flexible, and conductive 2D titanium carbide (mxene) films with high volumetric capacitance, Adv. Mater. 29 (2017) 1–9. doi:10.1002/adma.201702678.

[136] K. Lee, H. Lee, Y. Shin, Y. Yoon, D. Kim, H. Lee, Highly transparent and flexible supercapacitors using graphene-graphene quantum dots chelate, Nano Energy. 26 (2016) 746–754. doi:10.1016/j.nanoen.2016.06.030.

[137] J.J. Yoo, K. Balakrishnan, J. Huang, V. Meunier, B.G. Sumpter, A. Srivastava, M. Conway, A.L. Mohana Reddy, J. Yu, R. Vajtai, P.M. Ajayan, Ultrathin planar graphene supercapacitors, Nano Lett. 11 (2011) 1423–1427.

doi:10.1021/nl200225j.

[138] G. Giordano, N. Vil??, E. Aubert, J. Ghanbaja, A. Walcarius, Multi-layered, vertically-aligned and functionalized mesoporous silica films generated by sequential electrochemically assisted self-assembly, Electrochim. Acta. 237 (2017) 227–236. doi:10.1016/j.electacta.2017.03.220.

[139] C.J. Brinker, A.J. Hurd, P.R. Schunk, G.C. Frye, C.S. Ashley, Review of sol-gel thin film formation, J. Non. Cryst. Solids. 147–148 (1992) 424–436. doi:10.1016/S0022-3093(05)80653-2.

[140] F. Qu, R. Nasraoui, M. Etienne, Y.B. Saint Côme, A. Kuhn, J. Lenz, J. Gajdzik, R. Hempelmann, A. Walcarius, Electrogeneration of ultra-thin silica films for the functionalization of macroporous electrodes, Electrochem. Commun. 13 (2011) 138–142. doi:10.1016/j.elecom.2010.11.034.

[141] I. Mazurenko, M. Etienne, R. Ostermann, B.M. Smarsly, O. Tananaiko, V. Zaitsev, A. Walcarius, Controlled electrochemically-assisted deposition of sol-gel biocomposite on electrospun platinum nanofibers, Langmuir. 27 (2011) 7140–7147. doi:10.1021/la200069z.

[142] L. Fang, Q.Q. He, M.J. Zhou, J.P. Zhao, J.M. Hu, Electrochemically assisted deposition of sol–gel films on graphene nanosheets, Electrochem. Commun. 109 (2019) 106609. doi:10.1016/j.elecom.2019.106609.

[143] R. Shi, C. Han, H. Duan, L. Xu, D. Zhou, H. Li, J. Li, F. Kang, B. Li, G. Wang, Redox-active organic sodium anthraquinone-2-sulfonate (AQS) anchored on reduced graphene oxide for high-performance supercapacitors, Adv. Energy Mater. 8 (2018) 1802088. doi:10.1002/aenm.201802088.

[144] Y. Liu, B. Zhang, Q. Xu, Y. Hou, S. Seyedin, S. Qin, G.G. Wallace, S. Beirne, J.M. Razal, J. Chen, Development of graphene oxide/polyaniline inks for high performance flexible microsupercapacitors via extrusion printing, Adv. Funct. Mater. 28 (2018) 1706592. doi:10.1002/adfm.201706592.

[145] W.H. Low, P.S. Khiew, S.S. Lim, C.W. Siong, E.R. Ezeigwe, Recent development of mixed transition metal oxide and graphene/mixed transition metal oxide based hybrid nanostructures for advanced supercapacitors, J. Alloys Compd. 775 (2019) 1324–1356. doi:10.1016/j.jallcom.2018.10.102.

[146] A. Bakandritsos, P. Jakubec, M. Pykal, M. Otyepka, Covalently functionalized graphene as a supercapacitor electrode material, FlatChem. 13 (2019) 25–33. doi:10.1016/j.flatc.2018.12.004.

[147] K. Parvez, R. Li, S.R. Puniredd, Y. Hernandez, F. Hinkel, S. Wang, X. Feng, K. Müllen, Electrochemically exfoliated graphene as solution-processable, highly conductive electrodes for organic electronics, ACS Nano. 7 (2013) 3598–3606. doi:10.1021/nn400576v.

[148] L. Hu, X. Peng, Y. Li, L. Wang, K. Huo, L.Y.S. Lee, K.Y. Wong, P.K. Chu, Direct anodic exfoliation of graphite onto high-density aligned graphene for large capacity supercapacitors, Nano Energy. 34 (2017) 515–523. doi:10.1016/j.nanoen.2017.03.007.

[149] J. Wang, N. Vila, A. Walcarius, Redox-active vertically aligned mesoporous silica thin films as transparent surfaces for energy storage applications, ACS Appl. Mater. Interfaces. 12 (2020) 24262-24270. doi:10.1021/acsami.0c03650.

[150] K. Parvez, Z. Wu, R. Li, X. Liu, R. Graf, Exfoliation of graphite into graphene in aqueous solutions, J. Am. Chem. Soc. 136 (2014) 6083–6091. doi:10.1021/ja5017156.

[151] A.C. Ferrari, J. Robertson, Resonant Raman spectroscopy of disordered, amorphous, and diamondlike carbon, Phys. Rev. B. 64 (2001) 075414. doi:10.1103/PhysRevB.64.075414.

[152] K.N. Kudin, B. Ozbas, H.C. Schniepp, R.K. Prud'homme, I.A. Aksay, R. Car, Raman spectra of graphite oxide and functionalized graphene sheets, Nano Lett. 8 (2008) 36–41. doi:10.1021/nl071822y.

[153] A.L. Dendramis, E.W. Schwinn, R.P. Sperline, A surface-enhanced Raman scattering study of CTAB adsorption on copper, Surf. Sci. 134 (1983) 675–688. doi:10.1016/0039-6028(83)90065-1.

[154] L. Poltorak, G. Herzog, A. Walcarius, Electrochemically assisted generation of silica deposits using a surfactant template at liquid/liquid microinterfaces, Langmuir. 30 (2014) 11453–11463. doi:10.1021/la501938g.

[155] L. Liu, A. Walcarius, Kinetics of the electrochemically-assisted deposition of sol-gel films, Phys. Chem. Chem. Phys. 19 (2017) 14972–14983. doi:10.1039/c7cp01775h.

[156] O. De Los Cobos, B. Fousseret, M. Lejeune, F. Rossignol, M. Dutreilh-Colas, C. Carrion, C. Boissiére, F. Ribot, C. Sanchez, X. Cattoën, M. Wong Chi Man, J.O. Durand, Tunable multifunctional mesoporous silica microdots arrays by combination of inkjet printing, eisa, and click chemistry, Chem. Mater. 24 (2012) 4337–4342. doi:10.1021/cm3022769.

[157] N.H. Ly, T.D. Nguyen, S.W. Joo, Raman spectroscopy of pH-induced release of zidovudine from lactobionic acid-conjugated PEGylated gold colloids, Colloids Surfaces B Biointerfaces. 171 (2018) 49–57. doi:10.1016/j.colsurfb.2018.05.042.

[158] J. Jiang, X. Li, P. Zhu, D. Li, X. Han, Q. Cui, H. Zhu, Effect of pressure on 4-toluenesulfonyl azide studied by raman scattering and synchrotron x-ray diffraction, J. Phys. Chem. C. 121 (2017) 1032–1039. doi:10.1021/acs.jpcc.6b11016.

[159] N. Moitra, P. Trens, L. Raehm, J.O. Durand, X. Cattoën, M.W. Chi Man, Facile route to functionalized mesoporous silica nanoparticles by click chemistry, J. Mater. Chem. 21 (2011) 13476–13482. doi:10.1039/c1jm12066b.

[160] F. Xi, L. Xuan, L. Lu, J. Huang, F. Yan, J. Liu, X. Dong, P. Chen, Improved adhesion and performance of vertically-aligned mesoporous silica-nanochannel film on reduced graphene oxide for direct electrochemical analysis of human

serum, Sensors Actuators, B Chem. 288 (2019) 133–140. doi:10.1016/j.snb.2019.02.115.

[161] R.A. Decréau, J.P. Collman, A. Hosseini, Electrochemical applications. How click chemistry brought biomimetic models to the next level: Electrocatalysis under controlled rate of electron transfer, Chem. Soc. Rev. 39 (2010) 1291–1301. doi:10.1039/b901972n.

[162] L. Zhang, N. Vilà, G.-W. Kohring, A. Walcarius, M. Etienne, Covalent immobilization of (2,2'-Bipyridyl) (pentamethylcyclopentadienyl)-rhodium complex on a porous carbon electrode for efficient electrocatalytic NADH regeneration, ACS Catal. 7 (2017) 4386–4394. doi:10.1021/acscatal.7b00128.

[163] E. Piccinini, J.S. Tuninetti, J. Irigoyen Otamendi, S.E. Moya, M. Ceolín, F. Battaglini, O. Azzaroni, Surfactants as mesogenic agents in layer-by-layer assembled polyelectrolyte/surfactant multilayers: Nanoarchitectured "soft" thin films displaying a tailored mesostructure, Phys. Chem. Chem. Phys. 20 (2018) 9298–9308. doi:10.1039/c7cp08203g.

[164] J.F. Moulder, W.F. Stickle, P.E. Sobol, K.D. Bomben, Handbook of X-ray Photoelectron Spectroscopy, Perkin-Elmer Corp, USA, 1992.

[165] E.W. Wollman, D. Kang, C.D. Frisbie, I.M. Lorkovic, M.S. Wrighton, Photosensitive self-assembled monolayers on gold: photochemistry of surface-confined aryl azide and cyclopentadienylmanganese tricarbonyl, J. Am. Chem. Soc. 116 (1994) 4395–4404. doi:10.1021/ja00089a030.

[166] J.P. Collman, N.K. Devaraj, T.P.A. Eberspacher, C.E.D. Chidsey, Mixed azide-terminated monolayers: A platform for modifying electrode surfaces, Langmuir. 22 (2006) 2457–2464. doi:10.1021/la052947q.

[167] S. Sandwich, Z. Wang, W. Wang, N. Coombs, N. Soheilnia, G.A. Ozin, Graphene oxide-periodic mesoporous vertically silica sandwich nanocomposites with oriented channels, 4 (2010) 7437–7450.

[168] D.M. Oliveira, A.S. Andrada, Synthesis of ordered mesoporous silica MCM-41 with controlled morphology for potential application in controlled drug delivery systems, Ceramica. 65 (2019) 170–179.

[169] E.F. Dalton, N.A. Surridge, J.C. Jernigan, K.O. Wilbourn, J.S. Facci, R.W. Murray, Charge transport in electroactive polymers consisting of fixed molecular redox sites, Chem. Phys. 141 (1990) 143–157. doi:10.1016/0301-0104(90)80026-T.

[170] D.N. Blauch, J.M. Savéant, Dynamics of electron hopping in assemblies of redox centers. percolation and diffusion, J. Am. Chem. Soc. 114 (1992) 3323–3332. doi:10.1021/ja00035a025.

[171] R. Pietschnig, Polymers with pendant ferrocenes, Chem. Soc. Rev. 45 (2016) 5216–5231. doi:10.1039/c6cs00196c.

[172] R.L.N. Hailes, A.M. Oliver, J. Gwyther, G.R. Whittell, I. Manners, Polyferrocenylsilanes: Synthesis, properties, and applications, Chem. Soc. Rev. 45 (2016) 5358–5407. doi:10.1039/c6cs00155f.

[173] L. Hu, T. Zhai, H. Li, Y. Wang, Redox-mediator-enhanced electrochemical capacitors: recent advances and future perspectives, ChemSusChem. 12 (2019) 1118–1132. doi:10.1002/cssc.201802450.

[174] T. Nguyen, M. Fátima Montemor, γ-FeOOH and amorphous Ni-Mn hydroxide on carbon nanofoam paper electrodes for hybrid supercapacitors, J. Mater. Chem. A. 6 (2018) 2612–2624. doi:10.1039/c7ta05582j.

[175] Z.B. Zhai, K.J. Huang, X. Wu, Superior mixed Co-Cd selenide nanorods for high performance alkaline battery-supercapacitor hybrid energy storage, Nano Energy. 47 (2018) 89–95. doi:10.1016/j.nanoen.2018.02.059.

[176] S. Li, C. Yu, J. Yang, C. Zhao, M. Zhang, H. Huang, Z. Liu, W. Guo, J. Qiu, A superhydrophilic “nanoglue” for stabilizing metal hydroxides onto carbon materials for high-energy and ultralong-life asymmetric supercapacitors, Energy

Environ. Sci. 10 (2017) 1958–1965. doi:10.1039/c7ee01040k.

[177] L. Wang, H. Yang, X. Liu, R. Zeng, M. Li, Y. Huang, X. Hu, Constructing hierarchical tectorum-like α-Fe_2O_3/PPy nanoarrays on carbon cloth for solid-state asymmetric supercapacitors, Angew. Chemie - Int. Ed. 56 (2017) 1105–1110. doi:10.1002/anie.201609527.

[178] X. Chen, Y. Zhu, M. Zhang, J. Sui, W. Peng, Y. Li, G.L. Zhang, F. Zhang, X. Fan, N-Butyllithium-treated $Ti_3C_2T_x$ MXene with excellent pseudocapacitor performance, ACS Nano. 13 (2019) 9449–9456. doi:10.1021/acsnano.9b04301.

[179] H.C. Chen, Y. Qin, H. Cao, X. Song, C. Huang, H. Feng, X.S. Zhao, Synthesis of amorphous nickel–cobalt–manganese hydroxides for supercapacitor-battery hybrid energy storage system, Energy Storage Mater. 17 (2019) 194–203. doi:10.1016/j.ensm.2018.07.018.

[180] L. Zhang, D. DeArmond, N.T. Alvarez, R. Malik, N. Oslin, C. McConnell, P.K. Adusei, Y.Y. Hsieh, V. Shanov, Flexible micro-supercapacitor based on graphene with 3d structure, Small. 13 (2017) 1–10. doi:10.1002/smll.201603114.

[181] A. Afif, S.M. Rahman, A. Tasfiah Azad, J. Zaini, M.A. Islan, A.K. Azad, Advanced materials and technologies for hybrid supercapacitors for energy storage – A review, J. Energy Storage. 25 (2019) 100852. doi:10.1016/j.est.2019.100852.

[182] J. Yang, X. Duan, Q. Qin, W. Zheng, Solvothermal synthesis of hierarchical flower-like β-NiS with excellent electrochemical performance for supercapacitors, J. Mater. Chem. A. 1 (2013) 7880–7884. doi:10.1039/c3ta11167a.

[183] P. Si, S. Ding, X.W. Lou, D.H. Kim, An electrochemically formed three-dimensional structure of polypyrrole/graphene nanoplatelets for high-performance supercapacitors, RSC Adv. 1 (2011) 1271–1278. doi:10.1039/c1ra00519g.

[184] M. Zhi, A. Manivannan, F. Meng, N. Wu, Highly conductive electrospun carbon nanofiber/MnO_2 coaxial nano-cables for high energy and power density supercapacitors, J. Power Sources. 208 (2012) 345–353. doi:10.1016/j.jpowsour.2012.02.048.

[185] J. Yang, S. Gunasekaran, Electrochemically reduced graphene oxide sheets for use in high performance supercapacitors, Carbon 51 (2013) 36–44. doi:10.1016/j.carbon.2012.08.003.

[186] Y. Yoon, K. Lee, S. Kwon, S. Seo, H. Yoo, S. Kim, Y. Shin, Y. Park, D. Kim, J.Y. Choi, H. Lee, Vertical alignments of graphene sheets spatially and densely piled for fast ion diffusion in compact supercapacitors, ACS Nano. 8 (2014) 4580–4590. doi:10.1021/nn500150j.

[187] L. Liu, H. Zhao, Y. Wang, Y. Fang, J. Xie, Y. Lei, Evaluating the role of nanostructured current collectors in energy storage capability of supercapacitor electrodes with thick electroactive materials layers, Adv. Funct. Mater. 28 (2018) 1705107–1705116. doi:10.1002/adfm.201705107.

[188] W.W. Liu, Y.Q. Feng, X. Bin Yan, J.T. Chen, Q.J. Xue, Superior micro-supercapacitors based on graphene quantum dots, Adv. Funct. Mater. 23 (2013) 4111–4122. doi:10.1002/adfm.201203771.

[189] J. Du, Z. Wang, J. Yu, S. Ullah, B. Yang, C. Li, N. Zhao, B. Fei, C. Zhu, J. Xu, Ultrahigh-strength ultrahigh molecular weight polyethylene (UHMWPE)-based fiber electrode for high performance flexible supercapacitors, Adv. Funct. Mater. 28 (2018) 1707351–1707360. doi:10.1002/adfm.201707351.

[190] H.J. Sim, C. Choi, D.Y. Lee, H. Kim, J.H. Yun, J.M. Kim, T.M. Kang, R. Ovalle, R.H. Baughman, C.W. Kee, S.J. Kim, Biomolecule based fiber supercapacitor for implantable device, Nano Energy. 47 (2018) 385–392. doi:10.1016/j.nanoen.2018.03.011.

[191] M.F. El-Kady, M. Ihns, M. Li, J.Y. Hwang, M.F. Mousavi, L. Chaney, A.T. Lech,

R.B. Kaner, Engineering three-dimensional hybrid supercapacitors and microsupercapacitors for high-performance integrated energy storage, Proc. Natl. Acad. Sci. U. S. A. 112 (2015) 4233–4238. doi:10.1073/pnas.1420398112.

[192] F. Su, X. Lv, M. Miao, High-performance two-ply yarn supercapacitors based on carbon nanotube yarns dotted with $Co_3O_4$and NiO nanoparticles, Small. 11 (2015) 854–861. doi:10.1002/smll.201401862.

[193] J. Lin, C. Zhang, Z. Yan, Y. Zhu, Z. Peng, R.H. Hauge, D. Natelson, J.M. Tour, 3-Dimensional Graphene Carbon Nanotube Carpet-Based Microsupercapacitors With High Electrochemical Performance, Nano Lett. 13 (2013) 72–78. doi:10.1021/nl3034976.

[194] D. Pech, M. Brunet, H. Durou, P. Huang, V. Mochalin, Y. Gogotsi, P.L. Taberna, P. Simon, Ultrahigh-power micrometre-sized supercapacitors based on onion-like carbon, Nat. Nanotechnol. 5 (2010) 651–654. doi:10.1038/nnano.2010.162.

[195] N.A. Kyerematen, T. Brousse, D. Pech, Microsupercapacitors as miniaturized energy-storage components for on-chip electronics, Nat. Nanotechnol. 12 (2017) 7–15. doi:10.1038/nnano.2016.196.

[196] H. He, Y. Fu, T. Zhao, X. Gao, L. Xing, Y. Zhang, X. Xue, All-solid-state flexible self-charging power cell basing on piezo-electrolyte for harvesting/storing body-motion energy and powering wearable electronics, Nano Energy. 39 (2017) 590–600. doi:10.1016/j.nanoen.2017.07.033.

[197] D.P. Dubal, N.R. Chodankar, D.H. Kim, P. Gomez-Romero, Towards flexible solid-state supercapacitors for smart and wearable electronics, Chem. Soc. Rev. 47 (2018) 2065–2129. doi:10.1039/c7cs00505a.

[198] C. Zhao, Y. Liu, S. Beirne, J. Razal, J. Chen, Recent development of fabricating flexible micro-supercapacitors for wearable devices, Adv. Mater. Technol. 3 (2018) 1–16. doi:10.1002/admt.201800028.

[199] Y. Shao, J. Li, Y. Li, H. Wang, Q. Zhang, R.B. Kaner, Flexible quasi-solid-state

planar micro-supercapacitor based on cellular graphene films, Mater. Horizons. 4 (2017) 1145–1150. doi:10.1039/c7mh00441a.

[200] C. (John) Zhang, V. Nicolosi, Graphene and MXene-based transparent conductive electrodes and supercapacitors, Energy Storage Mater. 222 (2018) 11–20. doi:10.1016/j.ensm.2018.05.003.

[201] S.H. Kang, I.G. Kim, B.N. Kim, J.H. Sul, Y.S. Kim, I.K. You, Facile fabrication of flexible in-plane graphene micro-supercapacitor via flash reduction, ETRI J. 40 (2018) 275–282. doi:10.4218/etrij.2017-0242.

[202] A. Lamberti, F. Clerici, M. Fontana, L. Scaltrito, A highly stretchable supercapacitor using laser-induced graphene electrodes onto elastomeric substrate, Adv. Energy Mater. 6 (2016). doi:10.1002/aenm.201600050.

[203] X. Pu, M. Liu, L. Li, S. Han, X. Li, C. Jiang, C. Du, J. Luo, W. Hu, Z.L. Wang, Wearable textile-based in-plane microsupercapacitors, Adv. Energy Mater. 6 (2016). doi:10.1002/aenm.201601254.

[204] J. Liang, A.K. Mondal, D.W. Wang, F. Iacopi, Graphene-based planar microsupercapacitors: recent advances and future challenges, Adv. Mater. Technol. 4 (2019) 1–38. doi:10.1002/admt.201800200.

[205] V.B. Mohan, K. Jayaraman, M. Stamm, D. Bhattacharyya, Physical and chemical mechanisms affecting electrical conductivity in reduced graphene oxide films, Thin Solid Films. 616 (2016) 172–182. doi:10.1016/j.tsf.2016.08.007.

[206] Y. Chen, B. Xu, J. Xu, J. Wen, T. Hua, C.W. Kan, Graphene-based in-planar supercapacitors by a novel laser-scribing, in-situ reduction and transfer-printed method on flexible substrates, J. Power Sources. 420 (2019) 82–87. doi:10.1016/j.jpowsour.2019.02.096.

[207] W. Gao, N. Singh, L. Song, Z. Liu, A.L.M. Reddy, L. Ci, R. Vajtai, Q. Zhang, B. Wei, P.M. Ajayan, Direct laser writing of micro-supercapacitors on hydrated

graphite oxide films, Nat. Nanotechnol. 6 (2011) 496–500. doi:10.1038/nnano.2011.110.

[208] Z.S. Wu, K. Parvez, X. Feng, K. Müllen, Graphene-based in-plane micro-supercapacitors with high power and energy densities, Nat. Commun. 4 (2013). doi:10.1038/ncomms3487.

[209] L. Li, E.B. Secor, K.S. Chen, J. Zhu, X. Liu, T.Z. Gao, J.W.T. Seo, Y. Zhao, M.C. Hersam, High-performance solid-state supercapacitors and microsupercapacitors derived from printable graphene inks, Adv. Energy Mater. 6 (2016). doi:10.1002/aenm.201600909.

[210] T.D. Ngo, A. Kashani, G. Imbalzano, K.T.Q. Nguyen, D. Hui, Additive manufacturing (3D printing): A review of materials, methods, applications and challenges, Compos. Part B Eng. 143 (2018) 172–196. doi:10.1016/j.compositesb.2018.02.012.

[211] A. Ambrosi, M. Pumera, 3D-printing technologies for electrochemical applications, Chem. Soc. Rev. 45 (2016) 2740–2755. doi:10.1039/c5cs00714c.

[212] L. Kang, M. Cui, F. Jiang, Y. Gao, H. Luo, J. Liu, W. Liang, C. Zhi, Nanoporous $CaCO_3$ coatings enabled uniform zn stripping/plating for long-life zinc rechargeable aqueous batteries, Adv. Energy Mater. 8 (2018) 1–8. doi:10.1002/aenm.201801090.

[213] S. Li, Q. Liu, J. Zhou, T. Pan, L. Gao, W. Zhang, L. Fan, Y. Lu, Hierarchical Co_3O_4 nanofiber–carbon sheet skeleton with superior Na/Li-philic property enabling highly stable alkali metal batteries, Adv. Funct. Mater. 29 (2019) 1–10. doi:10.1002/adfm.201808847.

[214] Z. Zhao, J. Zhao, Z. Hu, J. Li, J. Li, Y. Zhang, C. Wang, G. Cui, Long-life and deeply rechargeable aqueous Zn anodes enabled by a multifunctional brightener-inspired interphase, Energy Environ. Sci. 12 (2019) 1938–1949. doi:10.1039/c9ee00596j.

[215] K. Zhao, C. Wang, Y. Yu, M. Yan, Q. Wei, P. He, Y. Dong, Z. Zhang, X. Wang, L. Mai, Ultrathin surface coating enables stabilized zinc metal anode, Adv. Mater. Interfaces. 5 (2018) 1–7. doi:10.1002/admi.201800848.

[216] G.D. Han, S.S. Park, Y. Liu, D. Zhitomirsky, E. Cho, M. DincĂ, J.C. Grossman, Photon energy storage materials with high energy densities based on diacetylene-azobenzene derivatives, J. Mater. Chem. A. 4 (2016) 16157–16165. doi:10.1039/c6ta07086h.

[217] S. Li, H. Wang, J. Fang, Q. Liu, J. Wang, S. Guo, Photo-isomerization energy storage using azobenzene and nanoscale templates: A topical review, J. Therm. Sci. 29 (2020) 280–297. doi:10.1007/s11630-020-1245-y.

[218] T.J. Kucharski, N. Ferralis, A.M. Kolpak, J.O. Zheng, D.G. Nocera, J.C. Grossman, Templated assembly of photoswitches significantly increases the energy-storage capacity of solar thermal fuels, Nat. Chem. 6 (2014) 441–447. doi:10.1038/nchem.1918.

[219] W. Luo, Y. Feng, C. Qin, M. Li, S. Li, C. Cao, P. Long, E. Liu, W. Hu, K. Yoshino, W. Feng, High-energy, stable and recycled molecular solar thermal storage materials using AZO/graphene hybrids by optimizing hydrogen bonds, Nanoscale. 7 (2015) 16214–16221. doi:10.1039/c5nr03558a.

[220] G. Cai, J. Wang, P.S. Lee, Next-generation multifunctional electrochromic devices, Acc. Chem. Res. 49 (2016) 1469–1476. doi:10.1021/acs.accounts.6b00183.

[221] S.H. Fu, M. Higuchi, D.G. Kurth, Metallosupramolecular polyelectrolytes self-assembled from various pyridine ring-substituted bisterpyridines and metal ions: Photophysical, electrochemical, and electrochromic properties, J. Am. Chem. Soc. 130 (2008) 2073–2081. doi:10.1021/ja710380a.

[222] W. Cheng, J. He, K.E. Dettelbach, N.J.J. Johnson, R.S. Sherbo, C.P. Berlinguette, Photodeposited amorphous oxide films for electrochromic windows, Chem. 4

(2018) 821–832. doi:10.1016/j.chempr.2017.12.030.

[223] J.L. Wang, Y.R. Lu, H.H. Li, J.W. Liu, S.H. Yu, Large area co-assembly of nanowires for flexible transparent smart windows, J. Am. Chem. Soc. 139 (2017) 9921–9926. doi:10.1021/jacs.7b03227.

Appendix

Chemicals

The detailed chemical information used in this thesis is listed in the following **Table 1**.

Table 1 the chemicals used in this thesis

Name	Abbreviation/ Formula	Source	Molecular weight (g/mol)	Purity
Silica film precursors and template salt				
Tetraethoxysilane	TEOS	Alfa Aesar	208	98%
(3-chloropropyl) triethoxysilane	Cl-PTES	Alfa Aesar	241	97%
Cetyltrimethylammonium bromide	CTAB	Acros Organics	364	99%
(3-azidopropyl) triethoxysilane	Az-PTES	homemade	-	-
Solvent and electrolyte				
Acetonitrile	ACN	Merck	41	99%
Dimethylformamide	DMF	Merck	73	99%
Cyclohexane	C_6H_{12}	Merck	84	99%
Water	H_2O	Millipore Milli-Q	18	-
Ethanol	EtOH	Merck	46	95%
Sodium sulfate	Na_2SO_4	Sigma-Aldrich	142	99%
Lithium chloride	LiCl	Fluka	42	99%
Lithium perchlorate	$LiClO_4$	Sigma-Aldrich		
Sodium nitrate	$NaNO_3$	Prolabo	85	99%
Sulfuric acid	H_2SO_4	Sigma-Aldrich	98	99%
Reactants and catalysts				
Ethynylferrocene	EtynylFc	Sigma-Aldrich	210	97%

Ethynylcobaltocenium	EtynylCo	Homemade	-	-
Copper sulfate	$CuSO_4$	Sigma-Aldrich	160	99%
L^+ascorbic acid	AA	Merck	176	99%
Sodium azide	NaN_3	Acros Organics	65	99%
Tetrabutylammonium bromide	TBAB	Fluka	322	99%
Graphite foil	-	Shanghai Carbon	-	95%
Others				
Sodium diethyldithiocarbamate trihydrate	NaDDTC	Sigma-Aldrich	225	-
Hydrochloric acid (1 M)	HCl	Sigma-Aldrich	36	37
poly(vinyl alcohol)	PVA	Fluka	72000	-
Indium tin oxide	ITO	Delta Technologies	-	-

Characterization apparatus

Apparatus for electrochemical characterization

Electrochemical experiments (electrodeposition of the silica film, exfoliation of the graphite foil, cyclic voltammetry measurements, and charge-discharge curves) were performed using Autolab PGSTAT-100, Autolab PGSTAT-300, μAutolab, and Biologic VSP-300 potentiostats.

Apparatus for morphology observation

Transmission electron microscopy (TEM) investigation was performed with a JEOL ARM 200F – Cold FEG TEM/STEM equipped with a GIF Quantum ER. Scanning electron microscopy (SEM) investigation was performed with a JEOL JSM-840

apparatus equipped with an energy-dispersive X-ray (EDX) microanalyzer and the high-resolution SEM micrographs have been obtained with the model JSM-IT500HR apparatus (JEOL). Atomic force microscopy (AFM) analysis was done with Asylum MFP3D-Bio apparatus (Oxford Instrument).

Apparatus for spectral analysis

Fourier transform infrared spectroscopy (FTIR) measurement was carried out using a Nicolet 8700 apparatus equipped with a diffuse reflectance accessory (Smart Collector). Raman spectroscopy measurements were carried out with a Jobin Yvon T64000 spectrometer with green light laser (514 nm).

Apparatus for structure analysis

Grazing-Incidence Small-Angle X-ray Scattering (GISAXS) pattern was obtained using the Nanoviewer from Rigaku (CuK α radiation). The angle of incidence of the X-ray beam with respect to the film surface was set at 0.22°. The N_2 adsorption–desorption isotherms were recorded at −196°C on Belsorp system (BEL JAPAN, INC).